The HUNGARIAN JOURNAL OF INDUSTRY AND CHEMISTRY (HJIC)
formerly (until 2012) the Hungarian Journal of Industrial Chemistry

The HJIC is an international periodical that focuses on results of fundamental and applied research in the fields of

- Biotechnology
- Chemical Engineering Science
- Chemical Processes
- Energetics
- Environmental Chemistry
- Environmental Engineering & Technology
- Industrial Management
- Material Science
- Mechanical Engineering
- Mechatronics
- Process & System Engineering
- Recycling

in the form of original papers, reviews, short communications, and conference proceedings written in English.

EDITORIAL BOARD

Editor-in-chief: RÓBERT K. SZILÁGYI
Department of Chemistry and Biochemistry,
Montana State University, Bozeman, MT, U.S.A.

Honorary Senior Editor: GÉZA HORVÁTH
Department of Chemical Engineering Science,
University of Pannonia, Veszprém, Hungary

Associate Editors:

JÁNOS ABONYI
Department of Process Engineering,
University of Pannonia, Veszprém, Hungary

DEZSŐ BODA
Department of Physical Chemistry,
University of Pannonia, Veszprém, Hungary

NORBERT MISKOLCZI
MOL Department of Hydrocarbon and Coal Processing,
University of Pannonia, Veszprém, Hungary

DÓRA RIPPEL PETHŐ
Department of Chemical Engineering Science,
University of Pannonia, Veszprém, Hungary

Editors:

LÁSZLÓ BARTHA
MOL Department of Hydrocarbon and Coal Processing,
University of Pannonia, Veszprém, Hungary

KATALIN BÉLAFI-BAKÓ
Research Institute of Bioengineering,
Membrane Technology and Energetics,
University of Pannonia, Veszprém, Hungary

PETER CZERMAK
Institute of Bioprocess Engineering and
Pharmaceutical Technology, Mittelhessen University of
Applied Sciences, Giessen, Germany

DÉNES FODOR
Institute of Mechanical Engineering,
University of Pannonia, Veszprém, Hungary

MARIA GAVRILESCU
Department of Environmental Engineering
and Management,
Gheorghe Asachi Technical University of Iasi, Romania

LÁSZLÓ GUBICZA
Research Institute of Bioengineering, Membrane
Technology and Energetics,
University of Pannonia, Veszprém, Hungary

JENŐ HANCSÓK
MOL Department of Hydrocarbon and Coal Processing,
University of Pannonia, Veszprém, Hungary

JIŘÍ KLEMEŠ
Centre for Process Integration and Intensification,
University of Pannonia, Veszprém, Hungary

ZOLTÁN KOVÁCS
Department of Management,
University of Pannonia, Veszprém, Hungary

JÁNOS KRISTÓF
Department of Analytical Chemistry,
University of Pannonia, Veszprém, Hungary

ISTVÁN SZALAI
Institute of Physics and Mechatronics,
University of Pannonia, Veszprém, Hungary

FERENC SZEIFERT
Department of Process Engineering,
University of Pannonia, Veszprém, Hungary

JÁNOS SZÉPVÖLGYI
Research Centre for Natural Sciences,
University of Pannonia, Veszprém, Hungary

IMRE TÍMÁR
Institute of Mechanical Engineering,
University of Pannonia, Veszprém, Hungary

GYULA VATAI
Department of Food Engineering,
Corvinus University of Budapest, Hungary

GÁBOR VERESS
Federation of Technical and Scientific Societies –
MTESZ Budapest, Hungary

IBOLYA ZSOLDOS
Department of Material Science and Technology,
Széchenyi István University, Győr, Hungary

EDITORIAL OFFICE: UNIVERSITY OF PANNONIA, P.O. BOX 158, VESZPRÉM, 8201 (HUNGARY)
Tel.: +36 (88) 624-746, e-mail: hjic@almos.uni-pannon.hu; web: hjic.mk.uni-pannon.hu
Felelős szerkesztő: Szilágyi Róbert Károly Nyelvi lektor: Matthew Chen
Kiadja: Pannon Egyetem, 8200 Veszprém, Egyetem u. 10.
Levélcím: H-8201 Veszprém, Postafiók 158, Tel.: (88) 624-000
Felelős kiadó: a Pannon Egyetem, Mérnöki Kar dékánja

Hung. J. Ind. & Chem. *2013*, Vol. 41(2), pp. 83–136

Table of Contents

HUNGARIAN JOURNAL
OF INDUSTRY AND CHEMISTRY
VESZPRÉM
Vol. 41(2) pp. 83–108 (2013)

CORROSION PROTECTION WITH ULTRATHIN GRAPHENE COATINGS: A REVIEW

ANDRÁS GERGELY ✉ AND TAMÁS KRISTÓF

Department of Physical Chemistry, Institute of Chemistry, University of Pannonia, Egyetem u. 10., Veszprém 8200, HUNGARY
✉Email: gergelyandras@almos.uni-pannon.hu

Developments in surface treatment or finishing, and modification of structural metals have probably never been so dynamic than in recent years due to the need for new approaches to efficient corrosion protection. The application of coatings is a strategy to be followed to physically separate corrosive environments from metal surfaces. The overall protection efficiency depends on the coating's barrier properties. Traditional alternatives to coating suffer from inefficient physical protection in cases of low film thicknesses and at elevated temperatures. One of the most advanced options is to apply ultrathin atomic films to ensure complete separation of the metallic surface from the fluid media. Among the numerous materials and methods, exceptional chemical resistance and high domain size make graphene a promising candidate for constituting ultrathin coatings with interfacial atomic layers adherent and homogeneous coverage to feature firm barrier behaviour. This review focuses on the major efforts with notable results and points out some short comings that must be resolved to serve as a basis for further progress in this field.

Keywords: ultrathin coatings, graphene, metals, corrosion protection

Introduction

Nowadays graphene (Gr) is undoubtedly of great interest in many fields of science and engineering. The attention is due to its unique structure, electrical properties [1, 2], efficient heat spreading [3], wetting transparency [4], surface wetting tenability [5], and high reflectivity (mirrors for the beams of He and H_2) [6]. The Gr's practical impermeability to gases [7-9] is a result of the combination of its strong structure (carbon bond energy and intrinsic strength are 4.9 eV and 43 N m^{-1}, respectively) and its morphology that makes Gr to be the thinnest and most impermeable membrane [10]. In addition, because of its chemical inertness [11], especially against oxidation [12, 13], it is highly resistant to corrosion [14] under conditions where other substances would undergo chemical reactions [15, 16]. As a lightweight mono-atomic coating, Gr can function as one of the most advanced electron- and ion-transfer barriers at the metal-electrolyte interface, without notably altering optical properties and thermal conductivity of the substrates. Gr on metal surfaces is expected to afford oxidation resistance [11] based on its airtight balloon behaviour associated with its excellent barrier nature against oxygen diffusion [7]. Nevertheless, coherence, and uniformity of Gr coatings are apparently vital to achieve good corrosion protection. In accordance with general expectations, electrochemical properties of Gr [17, 18] and its coated derivatives were extensively investigated. The main results achieved recently are described in the following sections that are organised from the viewpoint of synthesis techniques and application purposes.

Pure Graphene Coatings

Direct Chemical Vapour Deposition (CVD) on Metal Surfaces

Early studies were inspired to synthesise full surface covering Gr films of the highest domain (single sheet) size and integrity to exert impermeability over macroscopically large surfaces. Later findings proved the viability of this concept as interfacial construction of thin layers is a promising way to provide durable corrosion protection for metallic substrates [19]. Generally, coatings play a vital role in improving surface quality and protection of substrates, since much effort has been made to produce films featuring excellent properties. Graphene is certainly one of the most prominent representatives of this kind and subsequently has been studied in almost all scientific and engineering fields. This new generation material has been a novel subject to incorporate into the latest corrosion protecting coatings. Achievements in utilising Gr as a pure and composite coating were first reviewed by TONG *et al.* [20]. The synthesis and functionalisation of Gr were briefly discussed and future perspectives suggested.

The simplest way is to grow Gr directly on metal surfaces, even though this strategy does not provide the most protective coatings due to low adherence of the inorganic layers as consequence of weak interaction. By direct CVD, metals like nickel [21], cobalt [22], iridium [23], ruthenium [24] and copper [21, 25-27] were coated with Gr (on large areas in certain cases) [25] using methane or acetylene as a carbon source [28, 29]. Deposition kinetics of carbon and the formation of Gr layers on copper were thoroughly explored; surface mediation theory was proved when poly-crystalline films were characterised with the domain size of 10 μm^2 [30]. Except for assessing the influence of grain orientation, the effect of other growth parameters was estimated. The most relevant findings are as follows:

1. The density of Gr nuclei decreased, conversely flake domain size increased as temperature increased and partial pressure of the carbon source decreased.
2. When the pressure dropped below a critical threshold then no Gr nucleation was observed and film formations terminated before reaching full surface coverage.
3. To achieve complete surface coverage, the partial pressure of methane must have been increased above 500 mTorr then full coverage was reached within 2 to 3 min. Only a supersaturated surface relaying on a critical threshold of partial pressure ~285 mTorr was suggested to drive the formation of fully coated copper substrates with a continuous layer of Gr flakes. Thus, carbon nuclei formed in the first step under a lower pressure followed by a second step of nuclei growth at a higher pressure, promoting full surface coverage.

The effects of these parameters coupled with the investigation of the orientation of metal crystals on Gr domain size were quantitatively evaluated at low temperatures [31]. The activation energy for Gr nucleation under atmospheric pressure was noticeably higher (9 eV) than under low-pressure CVD procedures (4 eV). Such a difference was attributed to copper sublimation at low pressure, because copper evaporation probably has a decisive impact on the desorption rate of carbon from the surface. Copper evaporation is restricted under atmospheric pressure, so the activation energy is assigned to the desorption of carbon clusters. Close to the melting point of copper, large single-crystal Gr synthesis was proposed at the highest possible temperature (probably to maintain the highest rate of interfacial mass-transfer, diffusion coefficient of the decomposed and fragmented precursor agents). By following these principles, single Gr crystals with a domain size of ~1 mm could be synthesised. The nucleation density was higher on (111) than on (100) and (101) surfaces without any identifiable preference at higher temperatures [32]. Under carefully optimised conditions, continuous films of some layers were obtained on polycrystalline nickel without void areas at the flake boundaries [21]. In that case, ambient pressure CVD was to grow Gr films of 1-12 layers, with flake sizes of up to 20 μm for single- and bilayers (BLs). An ultra high vacuum (UHV) chamber was not needed [33, 34] to finely balance nucleation and growth processes, instead, thermal annealing was employed leading to the emergence of single-crystalline nickel with grain sizes of 1-20 μm. Grain surfaces became atomically flat with some terraces and steps similar to single-crystals usually used for epitaxial UHV experiments and Gr growth took place probably *via* the precipitation of carbon in the metal. Because metallic grains may independently affect film thickness as a result of the high density of atomic steps at grain boundaries, multi-layer (ML) nucleation occurred mainly at those areas.

By using atmospheric pressure CVD, high quality Gr was grown on copper, eliminating all the major difficulties associated with the low-pressure method. Parameter optimisation involved evaluating the influence of the thickness, purity, morphology and crystallographic orientation of the metal foils on growth rates and the number of Gr layers. Scanning electron microscopy (SEM) images illustrating Gr flakes on polished foils besides XRD patterns of annealed foils are presented in *Fig.1* showing large copper domains on NR foils. The effects of copper impurities on the density of bilayers are signified; complete surface coverage on AA2 (the purest foil (99.999%) without double layers), AA1 and NR. In *Fig.2*, Gr quality is presented at various distances along the tube reactor. The methane concentration was higher at the inlet leading to a greater abundance of MLs (darker islands in the images). Gradual increase of concentration resulted in the formation of single-layer (SL) Gr growth over the entire length. A constant methane concentration yielded a high percentage of MLs at the inlet, incomplete coverage in the middle and separated single domains (seen as darker islands) at the outlet.

As a method of surface pre-treatment, electro-polishing [36, 37] in phosphoric acid seemed to be a good choice to achieve an appropriate degree of surface cleaning and minimised roughness. Acetic acid was highly efficient at cleaning the copper surface, but only capable of removing oxidised species without any further etching. Etching with ferric chloride solution generally gave similar results to electropolishing despite the greater roughness of the $FeCl_3$ treated copper foils. This was probably due to the considerable scale of copper recrystallisation during annealing at temperatures close to the melting point of copper before the CVD process, leading to the evolution of a smoother surface with a low density of defects serving as nucleation sites. Additionally, the growth rate was estimated depending on the purity and crystallographic orientation of copper but by far not as much as the partial pressure of hydrogen, because the amount of dissolved hydrogen depends less on the thickness of the copper substrate. Crystallographic orientation was found to be an important factor, since the growth rate on the surface of substrates characterised by Miller indexes (100) was faster than on (111) surface under ambient pressure. In contrast, at low pressure and temperature the (111) surface facilitates the fastest growth rate [38]. Furthermore, optimal conditions to achieve full surface covering films with the minimum proportion of MLs might greatly vary with purity of the metal specimens. High purity substrates contribute to the formation of SL

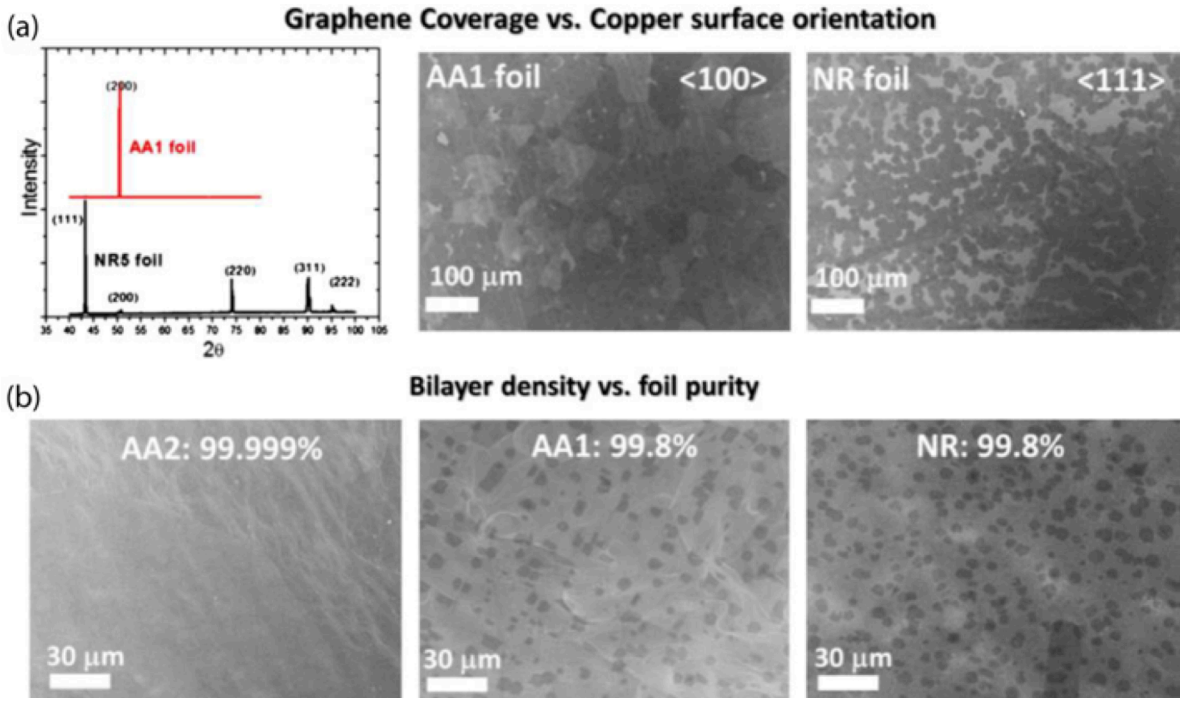

Figure 1: SEM images illustrate (a) Gr growth rate on polished AA1 and polished NR foils. XRD of annealed AA1 shows (100) orientation, the NR foil with the majority of (111) with smaller contributions from (110) and (311); (b) The effect of copper impurities on the density of bilayers [35] (republished by courtesy of the publisher, Elsevier)

films, and low purity metals support the evolution of multi-layer (ML) Gr coatings. Due to the multiple aspects of the reaction mechanism, optimal conditions for long foils are related to low and varied concentrations of carbon sources along the tube reactors, similarly to the application of temperature gradients (furnace dimensions and its relation to foil size) as well.

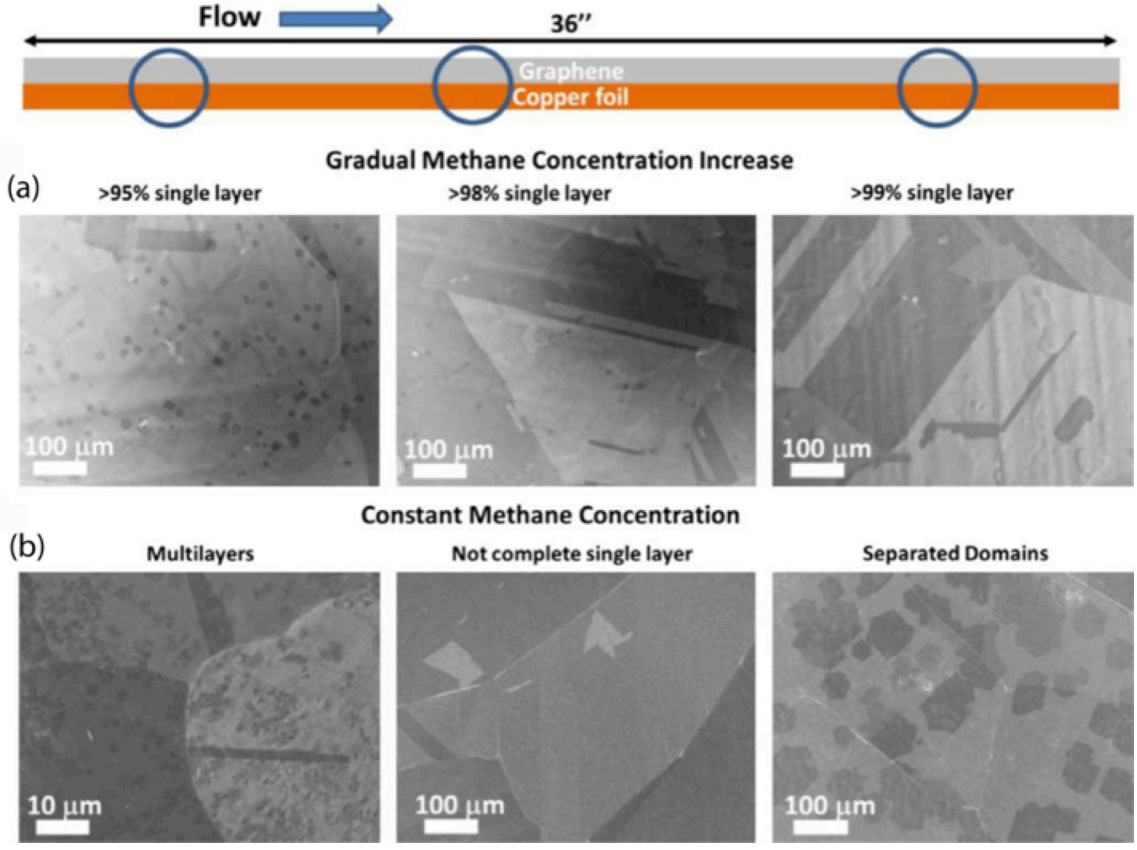

Figure 2: Gr films at various distances along the CVD reactor used at atmospheric pressure. (a) Gradual methane concentration, single-layer Gr growth over the tube reactor; (b) Multilayers at the inlet, incomplete surface coverage in the middle and separated single domains at the outlet [35] (republished by courtesy of the publisher, Elsevier)

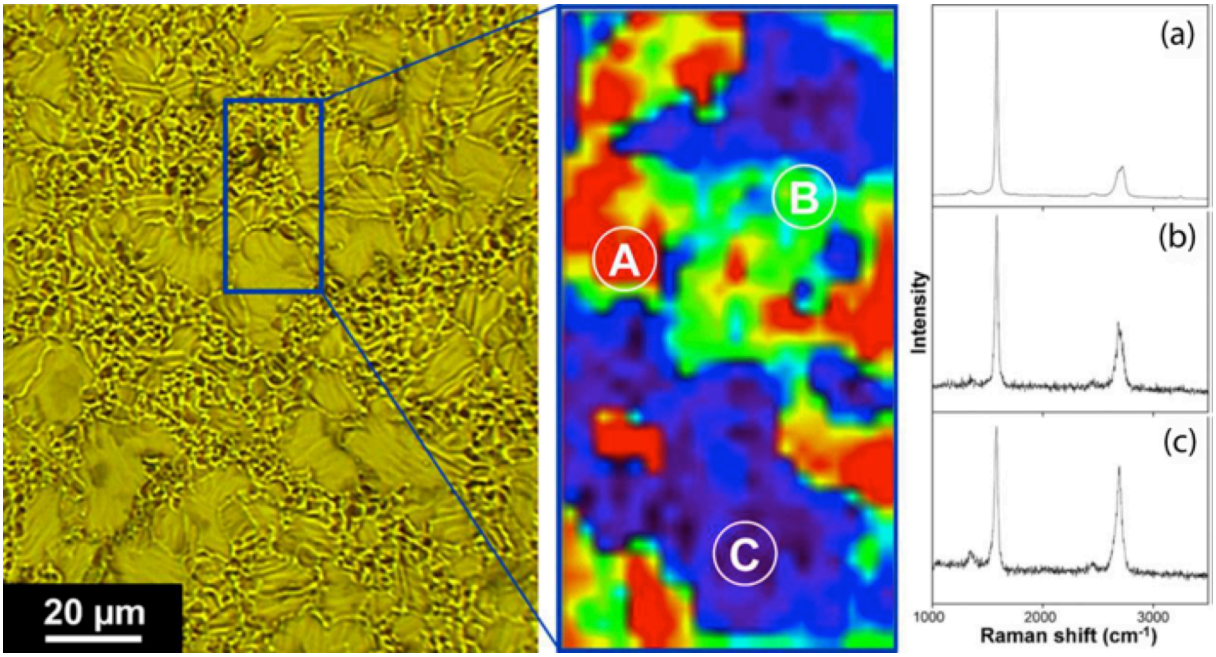

Figure 3: Optical micrograph, Raman map of ~2700 cm^{-1} peaks and respective Raman spectra of the areas on the Ni–Gr surface [41] (republished by courtesy of the publisher, Elsevier)

The gradual increase of methane concentration from 30 to 100 ppm in the mobile phase helps resolve the changing rate of activated carbon production [39]. Because methane concentration near the outlet increases slowly as a result of thermal decomposition and deposition, the main purpose of the gradually increasing methane concentration was to minimise bilayer growth at the inlet over the synthesis duration and to ensure full surface coverage near the outlet with the highest concentration of the carbon source. In fact, optimisation in the case of the atmospheric pressure CVD is more complicated than vacuum ones, which process in long tube chambers with small foils. A steady methane concentration at the inlet surely results in an increasing proportion of MLs at the inlet and incomplete coverage at the outlet, with visibly separated flake boundaries. The initial methane concentration of less than 30 ppm exclusively led to SL Gr at the inlet. High quality Gr grows with >99% monolayer coverage and in some cases films consisted of flake sizes of around 100 µm. High temperature etching with oxygen led to the visualisation of inter-domain boundaries as etching started at these boundaries and expanded into domains in a dendritic pattern, leaving diagonal stripes etch-free. Efficient corrosion resistive film properties were reported when experiments were made with samples exposed to air at 300 ºC, showing no sign of oxidation (oxygen enrichment in the metallic phase) over Gr coated areas in comparison to bare substrates.

According to a similar preference, growing Gr layers on copper is favourable, because copper does not dissolve carbon as much as nickel at high temperatures. However, it is also possible to grow MLs with highly ordered crystalline structures suing atmospheric CVD with controlled film thickness [40]. Both pure nickel and copper were covered with CVD grown Gr films detected as covering the majority of the metals in a SL form besides some areas of double and fragmented MLs (less than 5% of the coating) [41]. An optical micrograph and Raman map with the respective Raman spectra obtained from the Ni–Gr and Cu–Gr surfaces are presented in *Figs.3* and *4*, respectively. Electrochemical tests indicated that such coatings substantially reduced the corrosion rate of the substrates. By Raman spectroscopy investigation, SL Gr showed sharp G (1580 cm^{-1}) and 2D (2650–2700 cm^{-1}) bands with a small G/2D ratio, whereas ML Gr with a high G/2D ratio and an altered, less sharp 2D band were detected. Hence, 80 and 60% of the copper/nickel surface was covered with Gr as a single- or few-layers coating without uniformity on nickel. Scanning electron micrographs of the samples showed different thicknesses of the films with various scales of folding, full of wrinkles and edges. Thus, the overall conclusion was reached that coherent SL Gr is hard to obtain by direct deposition processes. Immersion type corrosion tests indicated open circuit potentials (OCPs) or free corrosion potentials of copper and nickel shifted towards the positive potential region. The electrochemical test conditions are summarised in *Table 1*. A potential ennoblement of about 0.3 V was measured for the corroding system of nickel/Gr and a cathodic shift of ~0.2 V observed with coated copper samples. The cathodic reduction processes were affected, inhibited by the Gr layer on copper and the rate of anodic half-reactions was apparently reduced near the steady free corrosion potential. However, during extended linear potential scanning Gr/nickel showed higher anodic currents than uncoated substrates opposed to the modified copper that exhibited no changes in the anodic branch after Gr deposition.

As an oxidation barrier for liquid and liquid–vapour phase-change cooling systems almost the same heat transfer efficiency was reported using bare and Gr/copper surfaces in liquid-phase and two-phase thermal performance tests [42]. After thermal treatment,

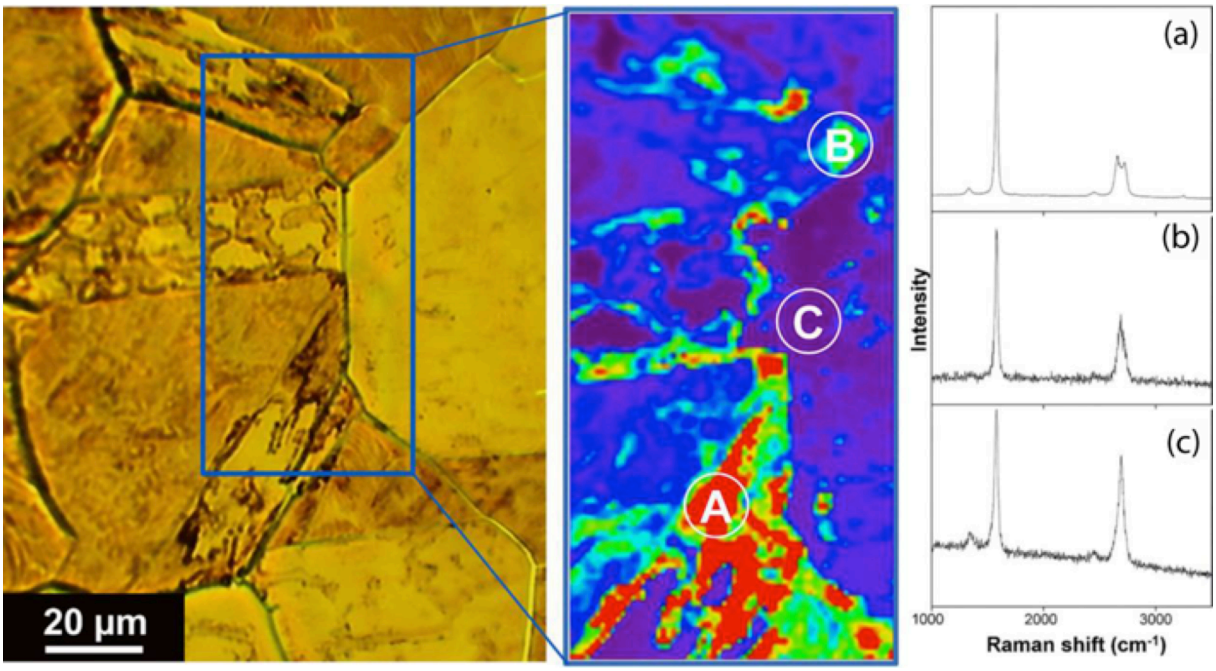

Figure 4: An optical micrograph, Raman map of ~2700 cm^{-1} peaks and respective Raman spectra of the areas on the Cu–Gr surface [41] (republished by courtesy of the publisher, Elsevier)

analysis revealed oxide formation on the entire surface of bare copper and limited oxidation at grain boundaries on the coated substrate. In conclusion, few Gr layers acted as a protective layer even under vigorous flow conditions near the boiling point of the fluid phase. Graphene prepared by microwave (MW) assisted CVD protected substrates from chemical oxidation when samples were heated under atmospheric conditions in a sequential multi-step procedure with dwelling times from 15, or 30 min to 1 h [43]. A very low degree of chemical oxidation of Gr over copper was indicated by XPS and the presence of cuprous oxide was found on the entire surface of bare specimens.

There are special applications such as steering and focusing elements for neutral atomic and molecular beams in de Broglie microscopes [44]. These mirrors utilise the quantum reflection of an atomic beam on metal surfaces since interaction volume is strictly limited to an extremely thin atomic layer of the metals. Oxidation and any other form of corrosion or adsorption of atmospheric gases might well lead to far lower reflectivity of the metallic surfaces, and the coatings of more than a few atomic layers are unacceptable. Thus, there are exceptional requirements of protective coatings and Gr films were expected to provide the solution in this matter too. Complete and uniform monolayers could be grown on polycrystalline ruthenium of a columnar structure on fused silica, exposing flat surface facets [45]. Single-layer Gr protects underlying metals with special structures like concave focusing mirrors and non-planar micro-electrode arrays from oxidation under ambient gases. Ruthenium was recovered by heating the samples under ambient conditions at 250 ºC for half an hour in an ultra-high vacuum, which was indicated by missing peaks in the oxygen (1s) region of the XPS spectra.

Gr on copper provided mediocre protection against electrochemical degradation in chloride environments [46]. Impedance measurements showed increased resistance at the metal/solution interface as anodic and cathodic current densities decreased with about hundred times higher charge-transfer resistance besides about thousand times lower double-layer capacitance in comparison to uncoated copper. Ennoblement of the free corrosion potential was also observed and related to the good barrier nature of the film.

The protection of copper against corrosion by the growing number of Gr layers was in part demonstrated [47]. To enable reliable and complete mechanical blockage by the coating exploiting its impermeability and chemical inertness, preparation parameters were balanced to obtain an appropriate film structure. In *Fig.5*, cyclic voltammograms (CVs) of the bare and passivated copper (the latter with 1-3 Gr layers) are shown along with the intensity of oxidative currents besides the atomic force microscope image of the Cu/Gr after etching.

Fig.6 depicts CVs of Gr-coated copper and Gr-copper post-treated with aluminium oxide (AlO_x) of different thicknesses, along with the comparison of their peak currents. Nonetheless, nanometre size structural defects at flake boundaries were the main source of deficiency, decisive in the often-observed limited protection efficacy. To circumvent this problem, a general strategy is to grow ML island-free Gr films. Selective coverage of defect areas was achieved by atomic layer deposition, resulting in enhanced protection of ~99%. Bare copper in an aerated sulphate solution indicated a pitting corrosion rate of ~9 nm s^{-1} with a density of ~1 µm^{-2}.

The estimated diffusion rate of the reactants was above 1 m s^{-1} limiting the rate of corrosion processes.

Table 1: Metallic substrate, type and growth parameters to obtain Gr films by direct CVD deposition

Substrate	Preparation type & parameters	Corrosion test parameters	Surface of the working electrode (cm^2)	Types of electrochemical test	Ref.
Cu & Ni	CVD grown on metal surfaces	flat-cell, 0.1 M NaCl	0.07	potentiodyn. pol., scan rate: 1 mV s^{-1}, after min at OCP	[41]
Cu	CVD grown	flow-cell, mass velocity: 38 kg m^{-2} s^{-1} for 9 h, T = 59.5±0.5°C	3.06	none	[42]
Cu	MW assisted CVD	heating at 150°C, in air at 1 atm for 1 h	Unknown	none	[43]
Ru	CVD	ambient exposure	Unknown	none	[45]
Cu	CVD	0.1 M NaCl	0.785	potentiodyn. pol., scan rate: 0.5 mV s^{-1} from OCP, EIS after 1 h	[46]
Cu	CVD	aerated 0.1 M Na_2SO_4	0.24	cyclic voltammetry, scan rate: 10 mV s^{-1}	[47]
Ni	CVD	treated at 600 ºC in air, then 31 wt.% H_2O_2 for up to 2 h	Unknown	none	[49]
Cu & Ni	CVD & mech. transferred by spin-coating with PMMA at 4000 rpm for 45 s	0.1 M $NaSO_4$	0.4	potentiodyn. pol. & CV, scan rate: 0.005 mV s^{-1}, EIS	[50]
Cu & Si	CVD then transfer of layers with PMMA cured at 165 ºC	ox. at 225 ºC for 60 min and red. of Cu at 450 ºC for 90 min under O_2 and H_2 flow	Unknown	none	[60]
Cu	CVD, thiol func.: SLG-Cu treated with HCl & H_2O then 7.5 mM thiol-ethanol treatment for 2 h	lymphocyte transformation test & *in vivo* experiment	1.4	tests: Cu conc. by ICP-OES, cell viability & stimulation index for lymphocyte	[80]
Ni	template directed CVD	anode in glucose based electrolyte, Ni in ferricyanide catholyte	8	CV and EIS	[116]

Interestingly, in the case of the ML Gr films, mass transport remained fast across the sheets and parallel along their planes, which was anticipated by the outcome of a water permeation experiment [8]. This may explain the unchanged chemical inertness of the Gr coating, owing to the fast mass transport along and across the layers as etchant species permeate through unburied areas in outer layers and diffuse laterally while finding open areas in layers underneath. Inertness to electrochemical reactions could only be attained by thin layer deposition of aluminium oxide (within ~5 nm) by the means of an atomic layer deposition technique on Gr/copper. Only by this way could unburied regions on the copper surface be made void-free. After 160 atomic layer deposition cycles with a ~16 nm thick passivating film inhibition efficiency was ~99%. This was partly confirmed by Tafel analysis giving instantaneous general corrosion rates of ~99% to the copper-single layer Gr with 16 nm aluminium oxide and 87% to SL Gr/Cu, in comparison with bare copper.

The approach of the direct loading of a precursor, i.e., acetone on copper then annealing it to convert its vapours into Gr was investigated [47]. Monolayers formed with nearly 100% coverage after rapid thermal annealing. Under optimal conditions, acetone derived films with good crystallinity compared to common CVD grown counterparts. The passivity of the metal coated/masked with SL Gr was attributed to remarkably inhibited cathodic reduction reactions and barrier action against the diffusion of anions accessing the underlying substrate. So, SL Gr/copper exhibited ca. forty times lower corrosion rates compared to the mechanically polished copper, which means an inhibition efficacy of up to 97%. Nevertheless, optimal protection performance was proposed to be achieved by the application of four Gr layers with their short-term inhibitions of up to 99%. The corrosion current of the Gr/copper reduced by ca. sixty times compared to mechanically polished substrates and the OCP shifted towards the negative potential region. Electrochemical impedance spectroscopy (EIS) indicated ten thousand times lower electrolyte-metal interfacial capacitance (C_{dl}) of the Gr/copper samples than those of the mechanically polished specimens. Such a notable drop suggests a significant shrinkage of the exposed surface to the electrolyte. C_{dl} of the Gr/copper was ca. three times higher in NaCl solution (0.6 M) than in its diluted media (0.1 M), but 6.4 times lower than that obtained in 0.1 M Na_2SO_4. C_{dl} and constant phase element (CPE) of the Gr/copper samples suggest an electrochemically smaller active surface to interfacial charging (discharging) and adsorption (like a non-Faradaic Helmholtz capacitor) as the density of conductive pathways decreases besides the lower effective surface roughness than that of the mechanically polished substrate. The CPE was 2.7 times higher than that

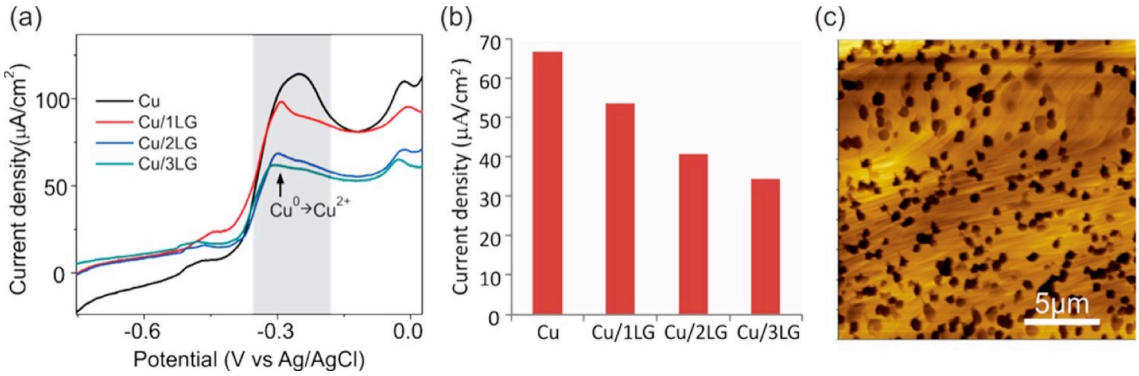

Figure 5: CVs of (a) bare Cu and Cu passivated by 1-3 layers of Gr, (b) intensity of oxidation currents under various passivation conditions, (c) atomic force microscope image of Cu/Gr after etching (adapted with permission from Ref. [47] Copyright (2014) American Chemical Society)

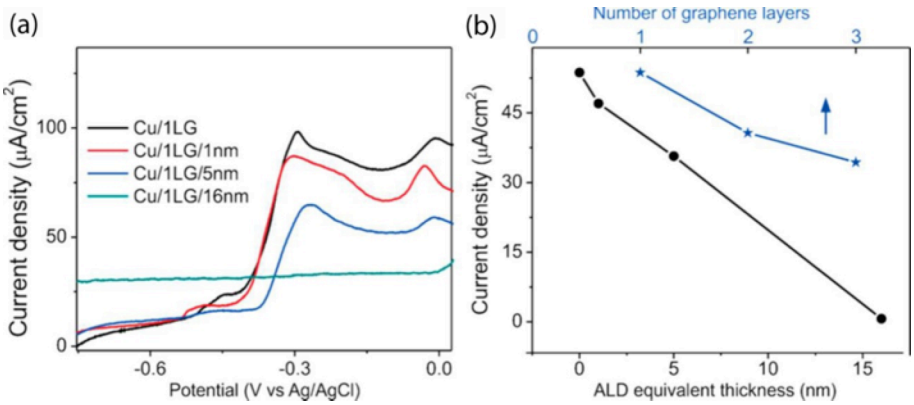

Figure 6: CVs of (a) Cu/Gr/Al samples, (b) Peak currents of Cu(0) for Cu/Gr/Al with different aluminium thicknesses and in comparison to Cu/Gr with 1-3 Gr layers (adapted with permission from Ref. [47] Copyright (2014) American Chemical Society)

measured in NaCl solution (0.1 M) and over ten times lower than in Na_2SO_4 solution (0.1 M). The resistance of coated copper to corrosion (R_{corr}) was ca. thirty five times higher than those of mechanically polished ones 6×10^4 and 1.6×10^3 Ω cm^2, respectively. R_{corr} was appreciably lower than that of NaCl and higher than with Na_2SO_4 solutions. Thus, inhibition efficacy was found as follows; >97% in 0.6 M and >71% in 0.1 M NaCl. Thus, performance was sensitive to the integrity of the Gr film as mechanically polished samples indicated rapid protection efficiency losses with increasing chloride concentrations in the test solutions.

Rigorous corrosion testing of nickel/CVD grown Gr films revealed low intensity oxidation of the substrate by heat treatment. Oxidation resistance was effective up to 500 ºC for 3 h, and with durable exposure (2 h) to essential hydrogen peroxide (31 wt.%) solution [49].

Both nickel and copper were coated with ML Gr films [14] by mechanical transfer. CV measurements indicated a remarkable restriction of the evolution of anodic and cathodic current transients, resulting in the effectively decreased electrochemical activity of the metal substrates. *Fig.7* depicts CVs of bare and Gr-coated copper samples, and XPS spectra of copper under ambient conditions, at 100 mV and sputter cleaning. Region (i) and (ii) contains a shoulder and a peak due to CuO and Cu_2O/Cu, respectively. The third part of the figure shows SEM images of Cu and Gr/Cu before and after voltammetry scans. Based on Tafel analysis, corrosion rate assessment (quantification prediction) for bare substrates gave the following results: ca. 6×10^{-13} and ca. 3×10^{-14} m s^{-1} for copper and nickel respectively. Graphene/copper indicated lower corrosion rate of ca. 8×10^{-14} m s^{-1} up to ca. seven times less than the bare substrate. The Gr/nickel showed a reduced rate of ca. twenty times to 2×10^{-15} m s^{-1}. With two or four folds of Gr layers, the corrosion rate of nickel decreased to 2×10^{-14} and 8×10^{-15} m s^{-1} respectively, which is considered as a notable performance improvement.

EIS measurements suggested an undamaged state of Gr, but the metal surface might corrode at high rates around void areas in the film. The most probable electrical network included resistive elements of the solution; $R_s \approx 40$ (6.5 Ω cm^2) and charge-transfer at the interface; initial $R_{ct} \approx 3\pm0.5$ kΩ cm^2 due to Faradaic processes. The mass transport process was modelled with a Warburg element ($W \approx 1.0\pm10^{-3}$ Ω^{-1} s$^{0.5}$ cm^{-2}) as a semi-infinite diffusion component. The inhomogeneity of the surface was handled by incorporating a CPE as a non-ideal capacitance in the circuit due to the impedance dispersity of the electrical double layer component at the metal-liquid interface. Double layer capacitance was best achieved with 2.2 μF cm^{-2} and the CPE was $Y_o \approx 7.6\pm10^{-5}$ Ω^{-1} s cm^{-2}. Increased resistance coupled in series was caused by the electrical surface resistance of Gr (≈1 kΩ) with a double layer capacitance of ~3.8 cm^{-2}. Average fitting parameters were changed

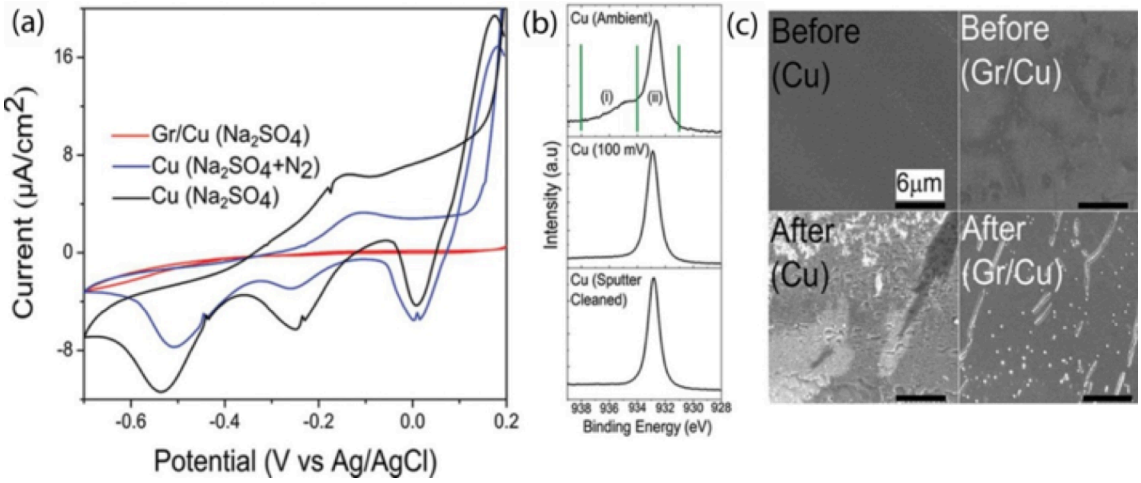

Figure 7: CVs of (a) bare Cu and Gr/Cu samples with the blue line corresponds to the measurement with N_2 bubbled through the solution; (b) XPS spectra of copper under ambient conditions at 100 mV and sputter cleaning with regions (i) and (ii) are due to CuO and Cu_2O/Cu(0), respectively; (c) SEM images of Cu and Gr/Cu before and after CV scan (adapted with permission from Ref. [14] Copyright (2014) American Chemical Society)

accordingly as follows: $C_{dl} \approx 9\pm5.0$ μF cm^{-2}, CPE: $Y_o \approx 2\pm10^{-5}$ Ω^{-1} s cm^{-2}, W ≈ 3±0.5 Ω^{-1} s$^{0.5}$ cm^{-2}, and $R_{ct} \approx 10\pm1.2$ kΩ cm^{-2}. The C_{dl} was ca. ten times lower than measured with bare copper, which seemed to be unrealistic. Such a difference is thought to originate from the quantum capacitance of the Gr film as a contribution in series with the C_{dl}. This is partly due to the small density of states in the Gr, which is in good agreement with the reported quantum capacitance of 7–10 μF cm^{-2} [50]. The increased R_{ct} of the copper samples in comparison with the one measured at the beginning of corrosion test suggested that the minor proportion of the metal substrate was uncoated with Gr, participated in corrosion processes. The proportion of this unburied area was estimated to be unexpectedly high ($A \approx 0.3$), exceeding the scale impressed by microscopy images ($A < 0.05$). Such a difference was attributed to the access to larger substrate areas by the diffusing depolarisator species and a subsequent greater proportion of Helmholtz capacitance then pseudo-capacitance based on electrochemical activation of metallic substrates for anodic reactions.

Nevertheless, the ability of Gr to catalyse, and depolarise cathodic reactions such as oxygen reduction [51] by well-coupling micro-galvanic cells in contact with the poly-aromatic sheets [52] either in planar or concentric forms (according to the function of the surface quinone group on carbon electrodes, i.e. GARTEN and WEISS's mechanism) is almost always a concern. Thus, protection efficiency depends largely on the deposition technique, quality, and epitaxial pile structure of the Gr sheets, affecting ionic and electrical transport through the films. Due to low adherence as a result of the lack of direct grafting or anchoring type chemisorption, direct CVD-grown films are classified as fragile coatings liable for potential polarisation and charging of the surface due to their structural alterations [53]. To increase the small domain size of the flakes, high temperature annealing at ~1035 ºC on the metal surface offers a resolution promoting further development of coherency of the films composed of large domains [54]. However, there are many problems with direct CVD deposition on metals like nickel because of the film formation mechanism of polyaromatic carbon materials.

The mechanisms of surface catalysis and adsorption during Gr growth on copper were determined [13, 55] to be different from film growth on nickel, which is governed by the combination of catalysis and adsorption as well as solubility and rejection. As the CVD technique enables the synthesis of Gr on larger metal surfaces [22, 56], carbon sources are thermally decomposed and fragmented into smaller segments, then atoms arrange into 2D honeycomb lattices. The preparation of CVD grown Gr films takes place readily on surfaces with face-centred cubic and hexagonal close-packed crystal structures. Methane and ethylene, which decompose at a temperature of ~1000 ºC are used as main precursors [24, 25] even though such a high temperature might significantly affect the metallographic state of the substrate, nucleation and deposition kinetics. Metals with close to zero solubility of carbon at the reaction temperature, e.g., copper, deposit *via* a catalytic mechanism and they are more likely to assist the formation of SL Gr instead of ML ones owing to the lack of catalytic effect after the first layer is deposited. Thus, the metal surface acts as a catalyst facilitating Gr growth in the form of a finishing coating, as deposition is restricted to SL [57]. Film growth on metals with mediocre carbon solubility at reaction temperatures undergoes *via* a complicated mechanism in which carbon diffuses into the bulk metal, e.g., nickel, and is rejected during the cooling process because of the decreasing solubility at lower temperatures. The rate of carbon rejection is critical to the development of ML Gr coatings. Hence, these films form preferentially instead of SLs on copper. Further complications may arise by the use of thicker metal specimens because thicker substrates dissolve larger amounts of carbon during the cooling phase since they release more carbon to produce larger amounts of carbon soot. Although any process that needs to be scaled-up must be optimised for engineering alloys, there are many results of theoretical interests as well.

A thesis [58] thoroughly investigated the protection efficacy of direct CVD grown Gr on copper, depending on flake size and uniformity, duration and temperature of the heat treatment. Key factors leading to firm protection performance both in terms of instantaneous and long-term functions are identified as to eliminate defects in the Gr sheets, flakes must build up a flawlessly continuous, coherent, and uniform film. Low nucleation and high growth rates must be maintained under low pressure to gain a low density of carbon spots (as probability of deposition decreases) and coherent films with the absence of unburied areas at flake boundaries. The films with large flake sizes were tested in a number of experiments to optimise growth parameters in order to reduce the amount of disorders, defects and void areas. A series of chemical oxidation experiments were performed by heating bare and coated copper foils at various temperatures and for various time frames. Ellipsometry helped characterise the thickness of oxide layers on the highly reflective copper. Heat treatment was carried out at 120 ºC under air for up to 76.5 hours. The growth rate of copper oxide layers, as an inherent indicator of the oxidation rate, almost linearly increased with time and the difference was only ca. a factor of six between the bare and coated copper foils. Corrosion deterioration was located at two spots where air leaked through defects in the Gr film and around its flake boundaries. Following growth time in low pressure CVD experiments, films were grown in a way that their flakes were not connected. Therefore, flake growth stopped before expanding sufficiently to connect with one another. Then oxidation was performed at 190 ºC for up to 37 h and 26 min. Optical microscopy images revealed a remarkable difference between the bare and coated copper samples. Then oxidation was repeated with closely spaced Gr flakes investigated by optical and SEM. The samples with closely spaced flakes gave very good results after a 30 min treatment at 190 ºC. A 13.5 h treatment led to minor deterioration in the substrate exhibiting black oxide patches on the surface but a 23 h and 35 min annealing resulted in corrosion of nearly the entire surface.

In a series of experiments, copper substrates coated with continuous Gr flakes were treated at 190 ºC for various periods of time. After a 30 min heating, samples exhibited a fine condition with some proportion of the surface composed of dark copper oxide. After a 10 h and 45 min treatment, migration of the corrosion front on the copper surface (CuO formation) proved to be far advancing and the heavily corroded areas showed a homogeneous distribution in the form of tree roots. Optical microscope images after 35 hours of heating indicated heavy corrosion, but the surface was not fully covered with oxides. Raman spectroscopy quantitatively characterised copper oxidation, which could proceed at flake boundaries as they feature the least hindrance to mass transport of depolarisators and the large sheets did not damage or etch oxidatively inside.

Apart from growth related issues, electrochemical aspects of the shortfalls may also be relevant. Gr films, acting as physical separators, might take part in electron transport, helping interfacial charge-transfer perpendicular to the surface based on good coupling and ballistic electron transport parallel to the basal plane of the sheets. Oxygen adsorption and reduction reactions with low activation energies may further complicate the application of this material, which has been recently underlined in a short- and long-term performance test of Gr/Cu and Si substrates [59]. Results clarified that the samples heated at 250 ºC for 6 min showed heavy oxidised spots on bare copper, but little oxidation on the Gr coated one. Therefore, Gr served as a sufficient oxidation barrier helping to preserve the metallic state from chemical oxidation over a short time period at high temperatures. Nonetheless, long-term annealing of coated copper led to severe oxidation probably because oxygen diffusion proceeded through discontinuities and defects around Gr sheets. After 17 h at 250 ºC, coated copper became heavily oxidised in a way indistinguishable from the bare specimens subjected to the same conditions. Similarly, a 15 min treatment at 185 ºC resulted in partial oxidisation of bare copper but coated samples remained almost entirely in a pristine state. Nevertheless, after 17 h annealing in air at 185 ºC, both bare and monolayer coated substrates became severely corroded and the products were identified as cupric oxide (CuO) in a stoichiometric ratio. The timescale of protection against thermal oxidation by Gr on copper was estimated to be ~1 h at 185 ^{o}C and ca. ten times faster at 250 ºC. To explore the long-term protection ability under less severe conditions, bare and coated copper specimens were stored under ambient conditions (at 25 ºC) at low but variable humidity levels for up to two years. Bare copper showed relatively slow oxidation at room temperature. Gr/Cu tested after up to eighteen months exhibited oxide-free condition over the first two weeks but within a month the surface started to tarnish non-uniformly (in several hundreds of micrometres in size). Within a few months, most of the regions became heavily oxidised with an estimated oxide layer thickness of tens or hundreds of nanometres. Alignment between the substrate grains and Gr flakes was concluded to have an influence on oxygen and water diffusion along the surface. After eighteen months, the entire surface had become oxidised as EDAX analysis revealed a predominant percentage of cuprous oxide (Cu_2O) in the oxide phase. Gr/silicon gave similar results as bare and coated samples were compared to each other after one week under atmospheric conditions, indicating an increased oxygen content of silicon as time of exposure increased. According to the outcome of the series of experiments, short-term oxidation testing reflected some degree of protection but long-term propagation unveiled extensive wet corrosion, similar to that seen in the case of bare copper specimens. The high rate of the wet corrosion of copper is due to promoted galvanic cell formation on a micrometre scale at ambient temperature, especially over long-term exposure.

As a special field, the majority of medical applications require metals even today, in bone and joint replacements [60, 61], stents [62, 63] dental materials [64, 65], pacemakers and generators [66, 67]. Stainless

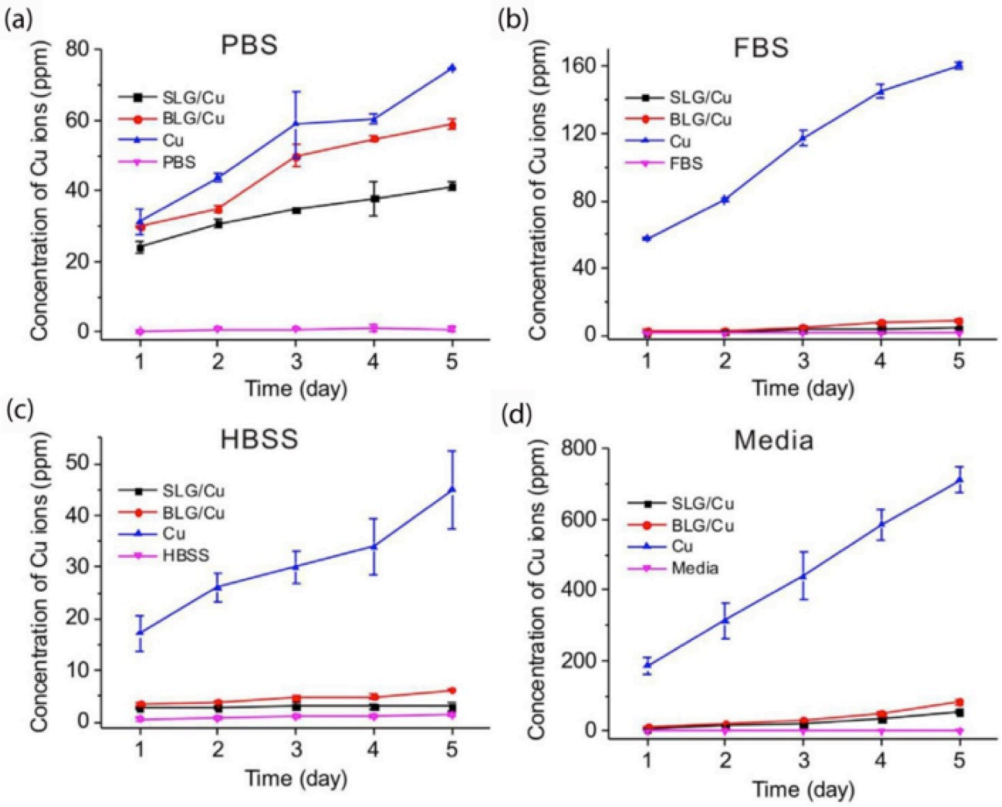

Figure 8: Concentration of Cu(II) ions from different biological solutions: in (a) PBS, (b) FBS, (c) HBSS solutions, and (d) cell culture media in the presence of SL (black) and BL Gr/Cu (red), Cu (blue) and blank solutions as controls (pink) measured by inductively coupled plasma-mass spectrometry (ICP-MS). All results are presented in a mass ratio (ppm) [79] (republished by courtesy of the publisher, Nature Publishing Group)

steel, titanium and cobalt alloys are the most common orthopaedic materials for joint prostheses articulated with a plastic bearing surface for many body parts [68, 69]. There are areas that require the use of alloys of mercury, silver, tin, copper along with limited amounts of zinc, palladium, indium, selenium and titanium in dental surgery [70, 71]. Despite the numerous successes, the main disadvantage of most of the alloys in medicine is their corrosion and the resulting physical deterioration (disintegration), quantity loss and contingent toxic side effects. The increased concentration of the aforementioned elements as soluble metals surely leads to chemical reactions of altered enzyme functions. It has been proven that soluble metals released because of corrosion processes can induce an innate monocytes-macrophage response and trigger immune responses, causing toxic, inflammatory, allergic or mutagenic reactions to patients [72]. In addition, corrosion leads to the adverse formation of metallic debris; solid particles and inorganic or organometallic compounds, in the periprosthetic soft tissues causing metallosis [73]. Furthermore, the corrosion degraded structural integrity leads to the premature failure and loosening of the metal devices [74]. Therefore, corrosion protection of metals used in physiological environments is of paramount importance and needs to be properly addressed for the sake of durable successful biomedical applications. Currently ceramic coatings are the most widely used to isolate metals from body fluids, e.g., zirconia transited from a zirconium alloy minimises corrosion in knee implants but the implants roughen with time. Nano-size diamond coatings and apatite-nano-diamond composites are promising candidates for the protection of metallic implants [75, 76], but they are highly permeable and greater surface roughness notably decreases their performance. Nowadays, atomic thin Gr films enhance the bio- and hemo-compatibility of implants to some extent [77, 78]. Interestingly, the outcome of almost all cell viability tests showed the biocompatibility of Gr on the nickel-titanium surface with some protection. After considering these facts, studies focused on clarifying the possibility of application of Gr as a corrosion protective film on structural metals used for biomedical devices. The most important future application would be the efficient corrosion protection of metallic prosthetics to avoid serious health problems to patients. In an effort to offer an alternative to protect metallic implants, Gr was proposed as a biocompatible and protective film as well [79]. Copper was the substrate for cell viability tests to reveal any change in immune response (lymphocyte transformation test) and the metal sensitivity test because of its high toxicity [80] making the experiment sensitive to reflect any significant protection. In vivo experiments served to study the protection of copper in live animals to evaluate Gr as a biocompatible film in physiological conditions. Corrosion inhibition of copper with Gr films was studied by the way of release and accumulation of copper ions in biological aqueous environments of phosphate buffered saline, fatal bovine serum and Hank's balanced salt solution. Cell culture

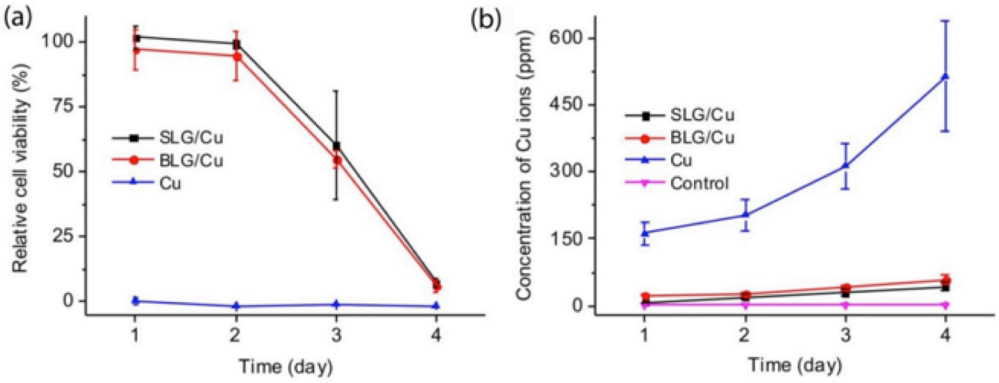

Figure 9: Relative cell viability and concentration of Cu(II) ions as a function of time. (a) Relative cell viability vs. time for SLG/Cu, BLG/Cu and Cu; (b) Concentration of Cu(II) ions in the cell culture medium after incubation with SLG/Cu. BLG/Cu and Cu (calculated from ICP-MS). A medium taken from a regular cell culture without Cu foils was used as the control [79] (republished by courtesy of the publisher, Nature Publishing Group)

media were monitored with inductively coupled plasma optical emission spectroscopy (ICP-OES) for five days. Single-layer Gr/copper indicated slightly varied but very good conditions on average.

The copper ion release rate was found to be at least an order of magnitude lower compared to bare copper that correlates almost linearly with time. The copper concentration in the solutions was higher when bilayer Gr/specimens propagated as compared to those of the tests with SL Gr obtained in all solutions. This was attributed to the stronger adhesion of SL films to metallic surfaces than bilayer ones, probably because of the better adaption to surface topography with high flexibility [81]. *Fig.8* shows the concentration of copper ions detected in different biological solutions such as phosphate buffered saline (PBS), fetal bovine serum (FBS), Hank's balanced salt solution (HBSS) and cell culture media with SL and BL Gr films and blank solutions as controls. Cell viability tests indicated almost the same results with single- and bilayer Gr/copper samples showing ±2.2 and 2.6% differences respectively compared to the control samples after the first day. Nonetheless, the results produced by low concentrations of dissolved copper in test solutions do not mean good results overall because the ion concentration could be much higher in a micro-milieu between the cells and coated substrate. The point of such a difference can explain why the cell viability dropped remarkably by more than 90% over the second, third, and fourth days of the test compared to the Gr contained samples although the copper concentration in the solutions remained very low (less than 70 ppm). Probably interfacial accumulation of metal ions must play a pivotal role in exceeding the toxicity limit, inevitably triggering lower cell viability. To resolve this problem, a further modification of the metal surface was necessary [82, 83]. By self-assembly monolayer treatment with decanethiol, bare and Gr/copper was modified with decanethiol, which was obviously assembled on the bare surface around the boundaries of Gr flakes. This is because the seemingly proper protection of copper was accompanied by much improved cell viability over three days *(Fig.9)*. The thiol modified SL Gr/Cu indicated that cell viability was ca. 55.8% after an incubation period of three days compared to SL Gr/Cu *(Fig.10)*. Thiol modified copper showed an improvement of up to 2% in comparison to the less than 1% viability observed for bare copper. These results suggest that Gr on copper is the major factor for protection, which can be appropriately enhanced by thiol modification. The film was also found to reduce immune response to copper in a clinical setting by a lymphocyte transformation test.

Animal experiments indicated a positive outcome to coated copper samples tested under *in vivo* conditions. The copper concentration was less than 3 and ~4.5 ppm in blood samples extracted from living rats implanted with SL coated and bare foils, reflecting the potential of thin Gr films in biomedical applications.

CVD-Grown Graphene Loading on Metal Surfaces by Mechanical and Electrical Techniques

Spin-Coating

There are a number of techniques to obtain high quality thin films. Static and dynamic dispense techniques such as dip [84-86], angle-dependent dip [87, 88], and hot dip spin, spin [89-92], spray [93], flow [94, 95], capillary [96, 97], roll [98], and reverse roll coating [99, 100] have developed thin layers on solid surfaces. By careful design, it is also possible to complement one another, offering a way to be tailored to application demands. Optimisation of these techniques is mostly dependent on actual parameters of the fluid phases and molecular or colloid solutions such as concentration, temperature, pressure, partial pressure or volatility of substances and solvents, dynamic or kinetic viscosity, and surface tension of fluid phases. The texture (roughness) of the substrate surface has much less influence (except for the surface energy) on the quality and quantity of casting. Drying and curing might later take place. From them, the ones featuring well controllable Gr growth are detailed in the following. Both spin-coating (SC) and kinetic spray (KS) are relatively novel techniques enabling us to form coatings of good quality on any sort of surface texture regardless of the substrates. SC is

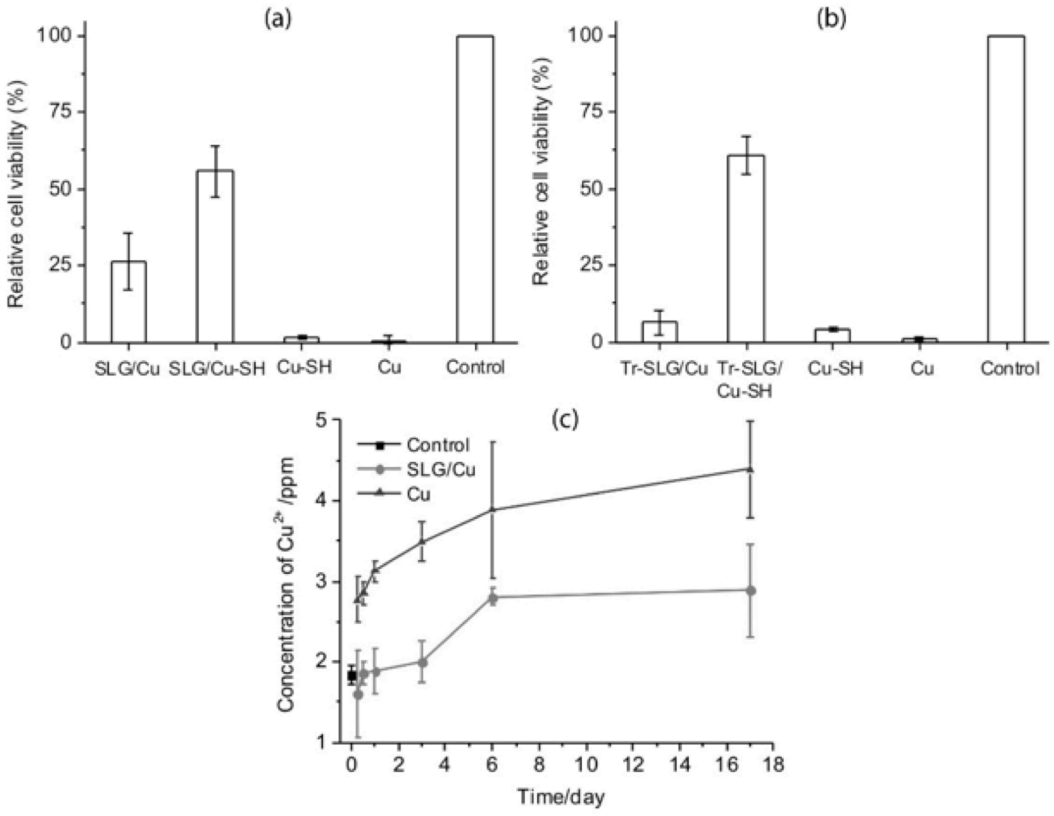

Figure 10: Relative cell viability of (a) bone cells incubated with SL Gr and SL Gr/Cu-SH, Cu-SH and bare Cu foil for 3 days. Control is a regular cell culture without Cu foils; (b) Relative cell viability of bone cells incubated with Tr-SL Gr/Cu, bare Cu, Tr-SL Gr/Cu-SH, and Cu-SH for 1 day; (c) Concentrations of Cu(II) ions in blood samples extracted from live rats with concentrations of Cu(II) from normal rats before implantation as control (black square), rats with implanted SLG/Cu foils (blue triangles) and rats with implanted Cu foils (red dots) as a function of time [79] (republished by courtesy of the publisher, Nature Publishing Group)

suitable to work out and implement practical deposition methods for atom-thick films on various metals, although a different approach must be applied for Newtonian [101] and non-Newtonian fluids [102]. Uniform coatings can be obtained over large areas with reproducible thicknesses in a good controllable manner, but only on planar substrates, which is a major limitation of this technique. SC starts by applying a small puddle onto the centre of the substrate, then spinning commences at initially a lower then, within a matter of seconds, at a higher rotational speed (two stages of centrifugation up to ~3000 rpm). The centrifugal force and centripetal acceleration result in excessive spreading of the fluids on the surface (wetting and covering depend on multiple physical-chemical parameters) and an inevitable loss (can be recycled) around the edges of the substrate until the spin-off time is completed. Then, a thin film forms releasing solvents and curing takes place, because of chemical reactions.

Kinetic Spray

Kinetic spray (KS) utilises a Laval nozzle to spray Gr colloid solutions at a very high speed and the supersonic acceleration leads to the production of very small droplets that evenly disperse then evaporate reducing the tendency of flake aggregation. Besides the uniform and smooth layers, defects in the Gr flakes were not observed. Hence, high quality film production by KS depends on the energy of the impact stretches Gr sheets then carbon atoms arrange into flawless hexagons based on plasticity probing of the Gr flakes [103]. Transmittance of graphene oxide (GrO) film spray deposited on soda-lime glass (from a 10 wt.% colloid solution of GrO in ethanol) was 73% and sheet resistance was 19 $k\Omega\ sq^{-1}$ using incident light at the wavelength of 550 nm. The electrical conductivity of the coatings increased by up to a thousand times after hydrazine reduction and annealing at 400 ºC. Additional thermal annealing at 1100 ºC further enhanced conductivity by ca. 10 times. Soda-lime glass with a transparency of 80% and electrical conductivity of 209 $S\ cm^{-1}$ (or sheet resistance; R_s = 2 $KX\ sq^{-1}$) as applied to a 14 nm thick Gr film [104]. KS is a reliable technique of wide commercial availability and offers a flexible solution to large-scale using according to recently reported corrosion tests [105-107].

Electrospinning

Electrospinning (ES) creates polymer fibres with a diameter range of between 40 and 2000 nm. The fibres can be made from solutions or from fused materials, controlling diameter size through the adjustment of

surface tension, solution concentration, conductivity and so forth [108-110]. ES occurs when the electric force of the surface overcomes the surface tension of the fluid phase triggering an electric spark, results in the solution being expelled from a syringe forming jet flow impacts and deposits. When the expelled material dries out or solidifies, it forms an electrically charged fibre that can be directed or speeded up by electric forces. So, a polymer solution stored in a syringe is charged to a high electrical potential. As the jet stretches and dries, radial electrical forces cause it to splash repeatedly. Dried, solidified fibres are collected on an electrically conductive (metal) screen. By ES, the composition of nylon 6-6 and Gr was prepared and deposited on porous silica then tested under various conditions [111]. Oxidation and reduction potentials in acidic, alkaline, and peroxide solutions were assessed by dynamic polarisation. SEM observations determined that treatment with acidic and basic solutions led to the formation of solid aggregates and slightly folded GrO flakes. Thermal treatment at 700 ºC gave samples with a porous structure. After annealing, a subsequent chemical derivatisation with acidic, basic and peroxide solutions assisted with ultrasonication facilitated the separation of GrO sheets, leading to a solid composed of lower dimensional flakes, especially in the case of oxidation. Oxidation was carried out in KOH and the reduction in H_2SO_4 solution. EIS data obtained in the immersion test with a Na_2SO_4 solution indicated decreasing interfacial capacitance of the ES produced samples with the Ny-GrO coatings. The EIS data calculated at 0.8 Hz changed between $1.4–4.5\times10^{-5}$ and $7.5–8.9\times10^{-7}$ F cm^{-2} (depending on the concentration of the electrolyte) with the GrO content increasing from 0.4 wt.% to 2 wt.%.

Electrophoresis

Electrophoretic deposition (EPD) is a promising technique to fabricate functionally graded [112-114] and hybrid composites [115, 116], laminated nano-ceramics [117, 118], and functional, nanostructured films and coatings [119-121]. In the last couple of years, numerous EPD applications have emerged as industries count on commercial advantages over other fabrication routes. It is a versatile and cost effective technique with acceptable levels of control over microstructure, stoichiometry, and macroscopic-microscopic dimensions and properties [122, 123]. EPD is a two-step colloid process in which electrostatically charged particles, suspended in a liquid medium, migrate according to the electric field towards the oppositely charged electrode. Then particles deposit, and flocculate on the electrode surface forming a relatively dense, homogeneously packed, bonded layer. Increasing the volume fraction of the nanoparticles and their deposition on the surface of any electrically conductive material is relatively easy. Usually, a post-treatment is required to increase the density of deposits and eliminate porosity [122]. Sometimes special modifications are required to render surfaces with notable properties such as increasing hydrophobicity by silylation. EPD is performed in stable colloid solutions in which there are plenty of electrostatically charged particles migrating in response to an impressed DC electric field and deposit either as a loose homogeneous or compact film onto the oppositely charged electrodes. To make deposits denser and eliminate porosity, additional EPD or heat treatment is required. Oxide particles, conductive polymers [124] and highly dispersed activated carbon [125] of nearly any size in colloidal suspensions [122] were deposited by this method, reflecting its high versatility. Furthermore, by electrophoresis uniform thin layers can be made on highly ragged, complex surfaces. Moderate electrical conductivity of the resulting substrates is the only requirement. The sample surface is treated as a whole in a uniform manner, whereas dimensions, deposition rate, uniformity and scale up features are also favourable. EPD is a preferable alternative to many other methods like slurry dipping, thermal and plasma spraying, sputtering, and physical/chemical vapour deposition.

In the course of thick Gr layer deposition on copper by EPD [126], deoxygenation of carbon was hinted at by bathochromic shifts in the UV spectra because of the electrochemical configuration and reaction mechanism. Potentiodynamic scanning showed positively shifted corrosion potentials and lower corrosion currents (I_{corr}), which suggested only mediocre protection by the thick Gr films in the initial phase of immersion propagation.

The composite coating of reduced GrO was prepared by cathodic EPD in an aqueous solution in a symmetrical cell-electrode arrangement [127]. Optimum conditions for cathodic deposition were found to produce a thickness of ~40 nm by applying 10 V for 30 s. SEM observations revealed the size of the GrO sheets being 1–2 μm, covering the surface uniformly. The composite coating was shown to protect copper firmly from electrochemical corrosion. Potentiodynamic measurements indicated an ennobled free corrosion potential with slightly reduced anodic and cathodic current branches, suggesting a lower corrosion rate of the composite coated copper compared to its bare form during the early phase of propagation. Experimental conditions are summarised in *Table 2*.

By electrophoresis, GrO was uniformly deposited on a permanent magnet, e.g., NdFeB and the coating was subsequently reduced to partially remove functional groups containing oxygen [128]. The EPD GrO coating showed substantially better adhesion to the substrate compared to the spin-coated ones. The surface of the bare NdFeB was rough and porous but site-dependent topography of the EPD-GrO modified samples depended on the amount loaded. The relationship between the increasing thickness and decreasing adhesion of the coating with an extension of deposition time was determined. Raman, infrared, and X-ray photoelectron spectroscopy (XPS) results reflected the strong adhesion of EPD films and that was connected to the Koble-type decarboxylation mechanism [129, 130] of the surface yielding GrO flakes. An unexpected outcome was that several deterioration reactions were observed in GrO. The signal of epoxy groups decreased

Table 2: Metallic substrate, type and growth parameters to obtain Gr film by EPD and chronoamperometry

Substrate	Preparation types and their parameters	Corrosion test parameters	Work-electrode surface (cm^2)	Types of potentiodynamic tests	Ref.
Cu	GrO, EPD in sol. C = 1.0 mg cm^{-3}, E=1 V / 10 mm^{-1}, 10 min	air ox. at 200 ºC for 4 h, in 30 wt.% H_2O_2 for 2 min, then 0.1 M NaCl solution	Unknown	after 1 h at OCP, scan rate: 1 mV s^{-1}	[131]
Cu	red. GrO with polyiso-cyanate cured with HAA (hydroxyl acrylic acid), EPD for 30 s, at E = 10 V 10 mm^{-1}, 0.1 M $NaBH_4$ red. for 5 min	3.5 wt.% NaCl, at 25 ºC	1	after 2 h at OCP, scan rate: 1 mV s^{-1}	[132]
NdFeB	GrO red., EPD in sol. of 1 mg cm^{-3} GrO, NdFeB anode & Pt cathodic dep., E=10 V / 10 mm^{-1},	3.5 wt.% NaCl solution at room temperature	Unknown	EIS	[133]
Cu	GrO isocyanate cured with hydroxy acrylic, then silylation, EPD on Cu at 10-30 V 10 mm^{-1}	3.5 wt.% NaCl, at 25 ºC	1	EIS	[136]
Cu	chronoamperometry of GrO at −1.5 V for 10 min in sol. C = 2 g dm^{-3}, in 0.1 M KCl, at −1.5 V for 10 min, then GrO red. $NaBH_4$ (0.1M) for 5 min	OCP 3.5 wt.% NaCl sol. after 1 h	1	EIS	[138]
Mild steel	EPD in Ni sol. at pH = 3, Iρ = 1 A dm^{-2}, at t = 40°C, Gr c=100 mg dm^{-3}	3.5 wt.% NaCl, at 27 ºC	1	scan rate: 0.01 V s^{-1}, EIS	[169]

after deposition, which might be explained by the high anodic electrode potential applied to the working electrode and the large potential drop at the interface. The decrease in current density during potentiodynamic scanning and the positive shift in the free corrosion potential of the system reflected efficient initial protection but lower cohesion and adhesion of the thicker coatings, leading to a poorer protection potential.

The GrO-acrylic polymer composite fully covered the copper substrates, but the sheets were separated far from one another in an island like manner consequently a large percentage of the surface remained unburied [131]. As for the reagents, solution and cell arrangement, EPD conditions e.g. voltage (10 V) and deposition time (30 s) proved to be optimal to obtain crack-free films of an average thickness of 45 nm. An electrochemical investigation indicated insignificant protection performance of the composite coating under immersion propagation. A steady corrosion current extrapolated to the OCP region showed slight changes over the anodic and cathodic regions. A current density drop of 38.3–3.5 μA cm^{-2} was observed in comparison to the bare copper. A polarisation resistance of the composite covered specimen was assessed by EIS, assigning an increased charge-transfer resistance of ~25 Ω cm^{-2} (bare copper: ~8 Ω cm^{-2}).

Stainless steel specimens with an exposed geometrical surface of 100 cm^2 were almost uniformly deposited with GrO in H_2SO_4 solution by coupling the substrate cathodically [132]. For transferring purposes, chemical and electrochemical etching was developed to delaminate the reduced GrO film, giving coherent freestanding membranes or deposit them onto other substrates. By optimising electrophoretic parameters, a low voltage of 3 V was found to consolidate reduced GrO layers preferentially aligned in an in-plane direction through a cohesive electrophoretic squeezing force in near volume range of the electrode (cathode). The free-standing Gr membrane was reduced, annealed at 1000 ºC then a graphite-like architecture evolved with a *d*-spacing of 3.42 Å and C/O ratio of 16.7. Electrical conductivity was of high as 5.5×10^5 S m^{-1}.

Graphene Coated Metals in Electrochemical Cells and Batteries

Because corrosion is a serious problem in energy storage devices like batteries and fuel-cells [133], the application of GrO as a barrier coating to inhibit the corrosion of aluminium electrodes in lithium ion batteries is considered to be an innovative solution. Spin-coating was employed to coat aluminium with GrO and decrease the corrosion rate when the electrode was subjected to the electrolyte of $LiPF_6$ (1.0 M) dissolved in ethylene carbonate and dimethylcarbonate (50:50 vol.%) [134]. SEM observations with energy dispersive X-ray spectroscopy analysis and atomic force microscopy (AFM) scanning suggested increasing surface roughness of aluminium with lower GrO quantity, but its greater amount helped reduce the roughness remarkably. The average roughness of the bare substrate was around 350 nm, which changed to 199-154 nm for the GrO loaded one. The thickness of the film showed great epitaxial variety even though the coating was relatively thick. Cyclic voltammetry showed a decreasing electrochemical current response of the GrO coated electrodes with increasing surface loading. This indicated hindered and impeded charge-transfer through the electrode interface without any direct implication of capacitive and adsorption charge loss in the current transients. Accordingly, chrono-amperometry curves exhibited moderately changing characteristics (as a consequence of altered electrode kinetics) in the early phase of the transients and

decreasing base currents over the complete timescale because of the smaller electroactive surface. EIS spectra suggested a somewhat higher resistance against pitting, the lower susceptibility to localised corrosion. Thus, GrO restricted aluminium oxidation, behaving as a charge-transfer barrier. Otherwise, the lower capacity and potential of the cells should have been measured by the set-ups with the GrO loaded electrodes during charge–discharge testing. Instead, surprisingly the opposite was reported. Nevertheless, enhanced cycle-life stability (lower rate of capacity loss) of the modified electrode compared to the cell configuration with bare aluminium is of course self-explanatory. Self-discharge was lower as a decreasing rate of open circuit voltage decline was observed to the modified aluminium samples. GrO films did not show any corrosion and the underlying native oxide layer remained intact under test conditions.

Microbiologically induced corrosion (MIC) severely limits the structural integrity and lifetime of metallic structures in technological processes and applications because of frequently evolving mechanisms, i.e., crevice and pitting local corrosion phenomena. A microbial fuel cell (MFC) is a galvanic cell producing an electric current that causes bioelectro-chemical oxidation of organic substances on anodes and abiotic reduction on cathodes [135]. MFCs have been used as a galvanic tool to simulate extracellular electron transfer mechanisms of microbes and the bio-electrochemical oxidation of organic substances. In addition, metals are not used as anodes in MFCs due to their fast galvanic corrosion. Owing to this, Gr films are employed as barrier coatings and the corrosion rate of the working nickel electrode was evaluated by galvanic coupling in the MFC set-up [136]. Regarding the experiment, it was determined that the geometrical ratio of the working and counter electrodes was the guarantee to maximise, and concentrate current densities on the working electrode.

Nevertheless, the cell design did not allow the assessment of adequate kinetic parameters (general corrosion rate) because of the large uncompensated ohmic drop and unfavourable cell geometry. These are all relevant in DC techniques, although inadequate voltammetric data could provide a rough estimation, even though 5 mV s^{-1} was higher than recommended and might have resulted in the considerable rate of adsorption and pseudo-capacitive current during the measurement. In relation to the impedance measurement and its evaluation, these data are even more sensitive to inappropriate cell design. The protection efficacy of the Gr film was assessed under realistic operating conditions, the bare and coated nickel electrodes represented a 3D microporous structure. The overall outcome confirmed a retardation of corrosion processes by the Gr film for extended periods. CV scanning showed decreased current transients of coated nickel, which was ca. ten thousand times lower than measured for the bare nickel electrode based MFC after a propagation for 2800 h. Nickel dissolution rates of the Gr coated anodes were at least ten times lower than the baseline (uncoated) electrode. EIS characterisation confirmed impeded MIC on the Gr/nickel for ca. 40 folds in comparison with uncoated electrodes. The effective masking of nickel from the mixture of microorganisms and their metabolic products was concluded.

Composite Graphene Coatings

Physically Mixed and in situ Polymerised Mixtures

Chronoamperometry was successfully employed to prepare Gr coated copper, starting from an aqueous colloid solution of GrO [137]. As a result of the EPD process, a seemingly compact and void of area without coating; and polymer film with Gr inclusion was obtained. Nevertheless, the distribution of Gr flakes was highly uneven and inhomogeneous (random), whereas the sheets showed various degrees of folding and overlapping in the polymer matrix. In addition, the fast reduction of GrO in the polymer proves the high permeability of the matrix, although it reached a thickness of several micrometres. On the other hand, the coatings with reduced GrO provided moderate protection for copper with an initial inhibition rate of 94% drawn from the potentiodynamic polarisation measurement data (at nil impressed potential). The corrosion rate reduced to 0.2 mm yr^{-1} from the rate for pure copper of ca. 3.65 mm yr^{-1}. This assessment was only made at the beginning of the immersion test (after an hour), whilst waiting for stabilisation of the freshly installed cell set-up. In comparison with the EIS investigation, the composite coating provided electrical insulation and ionic diffusion hindrance to the copper surface. So, the protection was related to the increased polarisation resistance of Gr loaded coatings of ca. 26 Ω cm^2 compared to bare copper of 9 Ω cm^2.

Intrinsically conducting polymers (ICPs) like electroactive polyaniline (PAni) have been widely used materials for some time providing corrosion protection regardless of the long-standing disagreement over the anodic protection mechanism and the generally less effective barrier nature. PAni is a preferable electron-conducting polymer with favourable properties over other alternatives. Under optimal conditions, the protection mechanism leads to the formation of a passive (dense) metal oxide layer [138-140].

To increase protection performance, many substances such as well dispersed clay [141] with an aspect ratio of ca. 200 was aimed at lengthening mass transport pathways through the composite films for all redox active species. These polymer-clay mixtures exhibited notable protection improvements over neat polymers. Besides the several attempts to combine of carbon nanotubes (CNTs) with organic [142-156], inorganic, and metal [157-160] matrixes for corrosion protection and resistance, respectively, there are examples from the literature about testing Gr-polymer composites for various purposes [160-162]. The main focus of these works was the exploitation of high relative aspect ratio of Gr (ca. 500) [163] in comparison to exfoliated clay minerals. Hence, Gr is a key filler in advanced gas barrier materials, motivating studies to

Table 3: Metallic substrate, type and growth parameters to obtain Gr films by spin coating and solution casting. Types and settings of corrosion tests and electrodes with the reference number of the article

Substrate	Preparation type and parameters	Corrosion test parameters	Work-electrode surface (cm^2)	Types of electrochemical tests	Ref.
porous silica	electrospin Gr-Nylon 6-6 in formic acid agitated for 12 h then add. of GrO, ES at 12 kV, flow rate: 0.2 mL h^{-1} for hours, Electrode: polymer solution 90 wt.% of formic acid with 0.36-2 wt.% GrO and Ny	Potentiostatic oxidation in KOH (0.5 M) for 3.5 h, reduction in H_2SO_4 at pH = 2 for 8 h, EIS in Na_2SO_4 in (1-10^{-1}-10^{-2}-10^{-3} M) for hours	unknown	potentiostatic treatment, potentiodynamic polarisation, scan rate: 100 mV min^{-1}, EIS	[112]
AlO_x	GrO sonication in ethanol then spin-coating	$LiPF_6$ in ethylene carbonate and dimethyl-carbonate (50:50 vol.%); at 1.0 M	100	cyclic voltammetry, chronoamperometry, potentiodynamic polarisation and EIS	[114]
Cu	Spin-coating of Gr with acetone (20 cm^3 cm^{-2}) then rapid annealing 800-1000 ºC for 3 min	Seawater 3.0–3.5% NaCl	0.25	potentiodynamic polarisation, scan rate: 2 mV s^{-1}, EIS	[136]
steel	PAni-Gr comp. (NMP complex and casting)	3.5 wt.% NaCl solution	unknown	potentiodynamic polarisation	[153]
cold-rolled steel	GrO red. with N_2H_2, pressing powders then curing (thickness: ~120 µm)	3.5 wt.% NaCl, at 25ºC	1	potentiodynamic scanning at 10 mV min^{-1}, after 30 min EIS	[161]
low alloy steel	2 wt.% Gr/MWCNT/PEI & 20 wt.% Gr/PEI comp.-s, dispersion in PAA cured at 150 ºC for 5 min, then 250 ºC for 5 min for imidisation	3.5 wt.% NaCl solution	9.62	potentiodynamic polarisation (scan rate: 1.67 mV s^{-1})	[7]

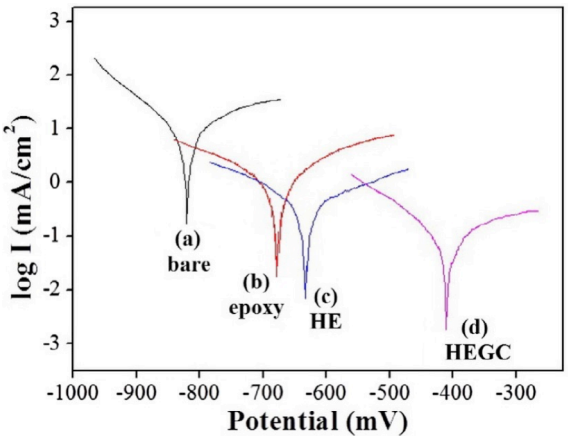

Figure 11: Tafel plots of the (a) bare, (b) epoxy-coated, (c) HE coated, and (d) HEGC-coated CRS electrodes [178] (by courtesy of the publisher, Elsevier)

achieve very low oxygen permeability using low filler contents (compared to neat polystyrene and the best polymer-clay mixture known at that time) [164] and underscore the possible obliteration of traditional clay-polymer composites [165-169]. Thus, a carefully designed and well-prepared PAni-Gr mixture exhibited outstanding impermeability characteristics against the diffusion of molecular oxygen and water vapour *versus* neat PAni and PAni-montmorillonite using a filler content of 0.5 wt.% and the excellent protection performance of steel substrates. Potential ennoblement of steel electrodes with coatings of increasing Gr content was considerable and an approximately fifteen times lower steady corrosion current was reported. The main reason for the success is mostly related to the high dispersity of Gr in the composite of microscopically isolated and macroscopically non-percolating distribution [170]. Experimental conditions are summarised in *Table 3*.

Lower electrical and ionic conductivities always provide better corrosion protection. Therefore, metals coated with Gr filled composites of electrically less or non-conducting (practically insulating) matrices like epoxy (in the case of high dispersity) can behave as a super-hydrophobic interface [171-176]. These composites are characterised by a water contact angle of at least 150º making them repellent, resistant to water absorption [177] and their exceptionally good anti-wetting properties results in good corrosion prevention potentials.

The nano-casting prepared epoxy-Gr composite featured high hydrophobicity and provided excellent protection for cold-rolled steel (CRS) panels [178]. *Fig.11* shows Tafel plots of bare, epoxy, hydrophobic epoxy (HE) and hydrophobic epoxy-Gr composite (HEGC) coated CRS panels. The open circuit potential of the immersion tested steel panels coated with epoxy-Gr showed appreciable ennoblement of ca. 0.3 V and ca. ten times lower corrosion currents compared to neat epoxy coated steel. The much higher polarisation resistance was partly attributed to the more hindered mass transport through the Gr loaded coating (with less than half the oxygen permeability) and access to its interface on the fluid side as a result of the finely patterned structure of the outer surface. The reproducibility of the data is questionable because parameters were not representative to properly describe the kinetic processes of the system, proceeding at the metal-solution interface. As in other cases, electrochemical techniques gave instantaneous rate assessments (in the first 30 min of the tests). Thus, the reported data are not suitable for forecasting long-term corrosion rates.

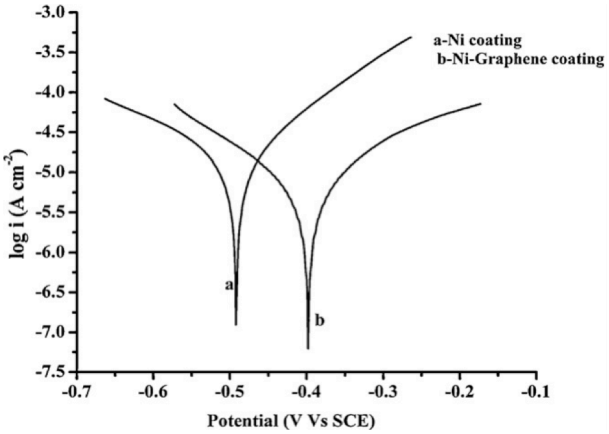

Figure 12: Tafel curves of Ni and Ni–Gr materials [186] (by courtesy of the publisher, Elsevier)

A more exotic approach is to develop metal-Gr composites for corrosion protection, although this strategy may have more disadvantages than advantages like with the metal-CNTs [179-182] because of the CNT activity towards catalytic oxygen reduction reactions [183-185]. Electrodeposited thin films of nickel matrix with Gr inclusion indicated a slight improvement in general protection performance; ennobled OCPs by ~0.1 V and steady corrosion currents reduced by over 50% were observed in comparison with pure nickel coated mild steel [186]. As a result of greatly affected nucleation and growth rate, measurement results are much more related to the highly altered crystalline structure of the nickel host matrix (lower electrical conductivity was unfortunately not characterised) as a consequence of the inclusion of Gr sheets, but differences in the texture and hardness of pure nickel and the Gr-nickel coatings were reported. Similarly to many other works, protection efficacy was not evaluated and reported over long-term immersion testing. On the one hand, the Tafel analysis of Ni and Ni–Gr performed in 3.5 wt.% NaCl solution (in *Fig.12*) was carried out using high voltage rate scanning without ohmic drop compensation, leading to distorted current legs over both potential regions (from the open-circuit or free corrosion potential of the electrode). A less representative transient is due to the low proportion of Faradaic charge-transfer current primarily assigned to the credible corrosion rate assessment. Probably due to these reasons, there is not much difference between the given corrosion currents of Ni and Ni-Gr samples. The Gr incorporation, cathodic and anodic Tafel regions exhibited almost ideal symmetry. This should mean the same scale of activation (expressed as a transfer function) in the cathodic (reduction and deposition) and anodic (oxidation and dissolution and/or deposition) processes. This feature is a kind of ineffectively blocked electrode behaviour, a quite reversible characteristic with less viable hindrance either in the anodic or cathodic processes. This suggestion seems to be confirmed by the reported similar corrosion currents.

On the other hand, the adequacy of EIS data may also be doubtful as basic requirements of system stability (in the time domain), linearity (immediate

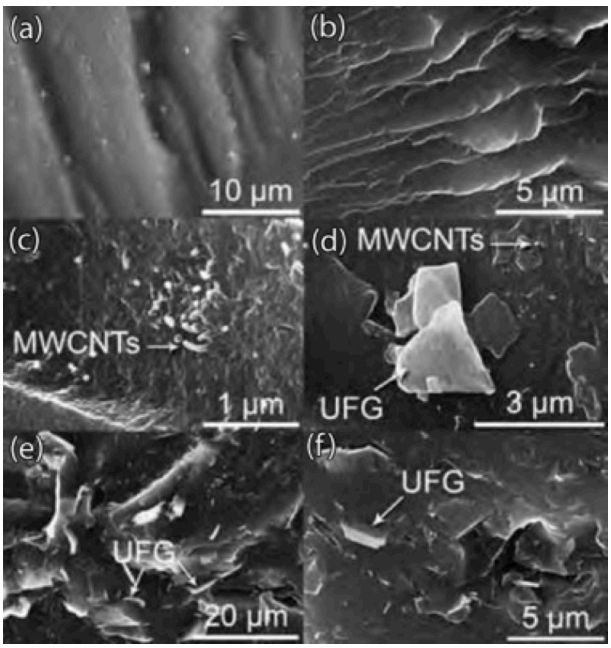

Figure 13: Cryo-fractured SEM images of (a) and (b), PEI, (c) and (d) 2 wt.% NFG/MWCNT/PEI, (e) and (f) 20 wt.% UNFG/PEI [187] (published with permission from the American Ceramic Society Bulletin)

response), and causality (the unquestionable relationship between perturbation and type-degree of response) might not be met. The time frame of 5 min to wait for a stationary or a steady-state condition then making measurements is in itself questionable. The large variation in the solution resistance (between the pure and composite Ni coating) is surely inadequate. In addition, the highly varied interfacial and coating resistance (swop between them) along with a hundred times difference in the coating capacitance are also unbelievable and can lead only to false interpretation. The depressed semicircle is a result of the complexity of the Ni/Gr electrode interface. The electrode was a porous electron and ion conductor and such systems need to be carefully handled (modelled with at least two transmission lines) when evaluation of impedance spectra in relation to structure and mechanistic behaviour of a complicated interface comes into the picture. Therefore, presented data and the corresponding evaluation are not appropriate and even misleading.

An innovative approach is the composite of multi-walled CNTs (MWCNTs) and exfoliated Gr embedded in polyether-imide (PEI) serving as a coherent and pore-free matrix [187]. This endeavour was made in an attempt to achieve a uniform dispersion of the nano-size additives in the host matrix (without functionalisation of the filler phase) and good adhesion of tailored PEI to the substrate, facilitating the maximum attainable corrosion protection performance. The protection mechanism was delineated according to the following: the composite protects steel alloys by a complex, active–passive way, serving as a physical barrier to water permeation against the evolution of ion channels to the metal surface and passivating metal surface by electron depletion at the interface based on the Schottky barrier effect [188-190].

Exfoliated but non-functionalised Gr was derived from ultrasonication in a solution of N-methyl-pyrrolidone (NMP). PEI as a host matrix was selected for its flexibility under a high glass transition temperature (155 ºC), thermal stability, firm resistance against radiation and appropriate interaction with carbon fillers *via* π–π stacking [191-193]. *In situ* synthesis and the imidisation protocol yielded coatings with appropriate adhesion properties to the steel surface of a thickness of 15–20 μm, whereas agglomeration and phase segregation of the fillers were low with the MWCNTs.

The SEM investigation revealed a fairly smooth surface finish without cracks or visible pinholes in the coatings. No phase segregation of the Gr and MWCNT fillers was observed in the mixtures around the interface as its clearly seen in *Fig.13* of the cryo-fractured samples of non-functionalised Gr (NFG), carbon nanotubes and PEI in 2 wt.% (c and d) and NFG/PEI of 20 wt.% (e, f) in comparison with pure PEI (a and b). OCPs were positively shifted by ~0.6 V, meaning a remarkable ennoblement. This was inferred, although substrates with high resistance coatings showing notable positive potentials must be at least partially attributed to the potential drop through the coatings [194] as a result of masking the real corrosion potential of the metal-coating interface to various extents. A potentiodynamic test indicated current densities of several orders of magnitudes lower (~10^{-9} A cm^{-2}) for composite coated specimens compared to bare low-alloy and galvanised steel samples with current densities of ~10^{-5} A cm^{-2}. Immersion tested samples were characterised quantitatively with regards to the perspective of corrosion rate or protection of steel substrates by weight-loss measurement (according to the ASTM-G1 protocol) after 3,144 hours. The substrate coated with 20 wt% Gr-PEI performed best with ca. thousand times lower corrosion rates (ca. 8.5×10^{-4} mm $year^{-1}$) than bare low-alloy steel samples (ca. 1.2×10^{-1} mm $year^{-1}$). However, the PEI film containing Gr and MWCNT (ca. 9.2×10^{-3} mm $year^{-1}$) manifested a moderate average corrosion rate of ca. 5.5×10^{-4} mm $year^{-1}$ compared to the neat PEI film.

Concluding Remarks

Overall, it is evident that atomic pure graphene films lack uniformity and partly this leads to insufficient instantaneous protection performance. Therefore, some sort of physical and/or chemical post-treatment is needed to facilitate long-term protection performance

From direct deposition techniques, the broadly and thoroughly investigated CVD technique is undoubtedly a viable alternative when large-scale continuous surface finishing is highly demanded. However, it is far from the best choice when corrosion protection efficiency and durability are the priorities, due to the complexity of growing cohesive films on the surface of metal substrates with preferable orientation of the grains, and weak adherence of Gr films sensitive to mechanical and surface charging effects.

When performance is an essential preference then spin-coating, kinetic spray, electro-spinning, and electrophoretic deposition should be employed depending on the complexity of the surface, conductivity of the substrate and additional technological aspects in relation to further processes. Among them, spin-coating and kinetic spray techniques develop good quality and homogeneous coatings of greatly varied thicknesses. Thin and ultra-thin films feature high a dispersity, and an even distribution and sometimes even improved quality of the nanoparticles. When thicker coatings are obtained on electrically conducting substrates with strong adhesion to complex surface geometries without the matter of a certain degree of alteration of the nanoparticles, then electrophoretic deposition must be used.

With respect to the utilisation of pure ultra-thin Gr films and thicker coatings as Gr-filled composites, there are ways to achieve further progress in relation to the ultimate aim of improved corrosion protection. For example, thin Gr films can still be used as a primary metal surface finishing. Alternatively, strongly adhering matrices with Gr filler might obviously mean a far more robust solution with protection efficacy targeting high performance demands for real situations. Parameters like the combination and concentration of the fillers, and compatibility with the host matrices besides matching complementary technological requirements need to be carefully optimised to gain appropriate barrier and/or inhibition functions.

Acknowledgement

The publication of this review was supported by Associate Professor OLIVÉR BÁNHIDI, University of Miskolc. His contribution is greatly appreciated.

REFERENCES

[1] NOVOSELOV K.S., GEIM A.K., MOROZOV S.V., JIANG D., ZHANG Y., DUBONOS S.V., GRIGORIEVA I.V., FIRSOV A.A.: Electric Field Effect in Atomically Thin Carbon Films, Science, *2004*, 306(5696), 666–669

[2] NOVOSELOV K.S., GEIM A.K., MOROZOV S.V., JIANG D., KATSNELSON M.I., GRIGORIEVA I.V., DUBONOS S.V., FIRSOV A.A.: Two-dimensional gas of massless Dirac fermions in graphene, Nature, *2005*, 438(7065), 197–200

[3] BALANDIN A.A.: Thermal properties of graphene and nanostructured carbon materials. Nat. Mater., *2011*, 10(8), 569–581

[4] RAFIEE J., MI X., GULLAPALLI H., THOMAS A.V., YAVARI F., SHI Y., AJAYAN P.M., KORATKAR N.A.: Wetting transparency of graphene, Nat. Mater., *2012*, 11(3), 217–222

[5] RAFIEE J., RAFIEE M.A., YU Z.-Z., KORATKAR N.: Superhydrophobic to superhydrophilic wetting control in graphene films, Adv. Mater., *2010*, 22(19), 2151– 2154

[6] SUTTER P., MINNITI M., ALBRECHT P., FARÍAS D., MIRANDA R., SUTTER E.: A high-reflectivity, ambient-stable graphene mirror for neutral atomic and molecular beams, Appl. Phys. Lett., *2011*, 99(21), Art. No. 211907

[7] BUNCH J.S., VERBRIDGE S.S., ALDEN J.S., VAN DER ZANDE A.M, PARPIA J.M., CRAIGHEAD H.G., MCEUEN P.L.: Impermeable atomic membranes from graphene sheets, *2008*, Nano Lett., 8(8), 2458–2462

[8] NAIR R.R., WU H.A., JAYARAM P.N., GRIGORIEVA I.V., GEIM A.K.: Unimpeded permeation of water through helium-leak-tight graphene-based membranes, Science, *2012*, 335(6067), 442–444

[9] LEENAERTS O., PARTOENS B., PEETERS F.M.: Graphene: a perfect nanoballoon, Appl. Phys. Lett., *2008*, 93(19), Art. No. 193107

[10] BERRY V.: Impermeability of graphene and its applications, Carbon, *2013*, 62(1), 1–10

[11] CHEN S., BROWN L., LEVENDORF M., CAI W., JU S.-Y., EDGEWORTH J., LI X., MAGNUSON C.W., VELAMAKANNI A., PINER R.D., KANG J., PARK J., RUOFF R.S.: Oxidation resistance of graphene-coated Cu and Cu/Ni alloy, ACS Nano, *2011*, 5(2), 1321–1327

[12] LIU L., RYU S.M., TOMASIK M.R., STOLYAROVA E., JUNG N., HYBERTSEN M.S., STEIGERWALD M.L., BRUS L.E., FLYNN G.W.: Graphene oxidation: thickness-dependent etching and strong chemical doping, Nano Lett., *2008*, 8(7) 1965–1970

[13] SURWADE S.P., LI Z.T., LIU H.T.: Thermal oxidation and unwrinkling of chemical vapor deposition-grown graphene, J. Phys. Chem. C, *2012*, 116(38) 20600–20606

[14] PRASAI, D. TUBERQUIA J.C., HARL R.R., JENNINGS G.K., ROGERS B.R., BOLOTIN K.I.: Graphene: corrosion-inhibiting coating, ACS Nano, *2012*, 6(2), 1102–1108

[15] DE HEER W.A., BERGER C., WU X., FIRST P.N., CONRAD E.H., LI X., LI T., SPRINKLE M., HASS J., SADOWSKI M.L., POTEMSKI M., MARTINEZ G.: Epitaxial graphene, Solid State Comm., *2007*, 143(1-2) 92–100

[16] SHIVARAMAN S., CHANDRASHEKHAR M.V.S., BOECKL J., SPENCER M.G.: Thickness estimation of epitaxial graphene on SiC using attenuation of substrate Raman intensity, J. Electron. Mater., *2009*, 38(6), 725–730

[17] RATINAC K.R., YANG W., GOODING J.J., THORDARSON P., BRAET F.: Graphene and related materials in electrochemical sensing, Electroanalysis, 2011, 23(8)3, 803–826

[18] BROWNSON D.A.C., MUNRO L.J., KAMPOURIS D.K., BANKS C.E.: Electrochemistry of graphene: not such a beneficial electrode material? RSC Adv., *2011*, 1(6), 978–988

[19] RAMAN R.K.S., TIWARI A.: Graphene: The thinnest known coating for corrosion protection, J. Org. Materials, *2014*, 66(4), 637–642

[20] TONG Y., BOHM S., SONG M.: Graphene based materials and their composites as coatings, Austin J. Nanomed. Nanotechnol., *2013*, 1(1), 1–16

[21] REINA A., JIA X., HO J., NEZICH D., SON H., BULOVIC V., DRESSELHAUS M.S., KONG J.: Large area, few-layer graphene films on arbitrary substrates by chemical vapor deposition, Nano Lett., *2009*, 9(1) 30–35

[22] KIM K.S., ZHAO Y., JANG H., LEE S.Y., KIM J.M., KIM K.S., AHN J.-H., KIM P., CHOI J.-Y., HONG B.H.: Large-scale pattern growth of graphene films for stretchable transparent electrodes, Nature, *2009*, 457(7230), 706–710

[23] CORAUX J., N'DIAYE A.T., BUSSE C., MICHELY T.: Structural coherency of graphene on Ir(111), Nano Lett., 2008, 8(2), 565–570

[24] SUTTER P.W., FLEGE J.-I., SUTTER E.A.: Epitaxial graphene on ruthenium, Nat. Mater., *2008*, 7(5), 406–410

[25] LI X., CAI W., AN., KIM S., NAH J., YANG D., PINER R., VELAMAKANNI A., JUNG I., TUTUC E., BANERJEE S.K., COLOMBO L., RUOFF R.S.: Large-area synthesis of high-quality and uniform graphene films on copper foils, Science, *2009*, 324(5932) 1312–1314

[26] LEE Y., BAE S., JANG H., JANG S., ZHU S.E., SIM S.H., SONG Y.I., HONG B.H., AHN J.H.: Wafer-scale synthesis and transfer of graphene films, Nano Lett., *2010*, 10(2), 490–493

[27] LI X.S., ZHU Y.W., CAI W.W., BORYSIAK M., HAN B., CHEN D., PINER R.D., COLOMBO L., RUOFF R.S.: Transfer of large-area graphene films for high-performance transparent conductive electrodes, Nano Lett., *2009*, 9(12), 4359–4363

[28] PARK H.J., MEYER J., ROTH S., SKÁKALOVA V.: Growth and properties of few-layer graphene prepared by chemical vapor deposition, Carbon, *2010*, 48(4), 1088–1094

[29] BAE S., KIM H., LEE Y., XU X., PARK J.-S., ZHENG Y., BALAKRISHNAN J., LEI T., KIM H.R., SONG Y.I., KIM Y.-J., KIM K.S., ÖZYILMAZ B., AHN J.-H., HONG B.H., IIJIMA S.: Roll-to-roll production of 30-inch graphene films for transparent electrodes, Nat. Nanotech., *2010*, 5(8), 574–578

[30] LI X., MAGNUSON C.W., VENUGOPAL A., AN J., SUK J.W., HAN B., BORYSIAK M., CAI W., VELAMAKANNI A., ZHU Y., FU L., VOGEL E.M., VOELKL E., COLOMBO L., RUOFF R.S.: Graphene films with large domain size by a two-step chemical vapor deposition process, Nano Lett., *2010*, 10(1), 4328– 4334

[31] LI X., MAGNUSON C.W., VENUGOPAL A., TROMP R.M., HANNON J.B., VOGEL E.M., COLOMBO L., RUOFF R.S.: Large-area graphene single crystals grown by low-pressure chemical vapor deposition of methane on copper, J. Am. Chem. Soc., *2011*, 133(9), 2816–2819

[32] VLASSIOUK I., SMIRNOV S., SURWADE S.P., REGMI M., SRIVASTAVA N., FEENSTRA R., ERES GY., PARISH C., LAVRIK N., DATSKOS P., DAI S., FULVIO P.: Graphene nucleation density on copper: fundamental role of background pressure, J. Phys. Chem. C, *2013*, 117(37), 18919–18926

[33] BERGER C., SONG Z.M., LI X.B., WU X.S., BROWN N., NAUD C., MAYO D., LI T.B., HASS J., MARCHENKOV A.N, CONRAD E.H., FIRST P.N., DE HEER W.A.: Electronic confinement and coherence in patterned epitaxial graphene, Science, *2006*, 312(5777), 1191–1196

[34] BERGER C., SONG Z.M., LI T.B., LI X.B., OGBAZGHI A.Y., FENG R., DAI Z.T., MARCHENKOV A.N., CONRAD E.H., FIRST P.N., DE HEER W.A.: Ultrathin epitaxial graphite: 2D electron gas properties and a route toward graphene-based nanoelectronics, J. Phys. Chem. B, *2004*, 108(52), 19912–19916

[35] VLASSIOUK I., FULVIO P., MEYER H., LAVRIK N., DAI S., DATSKOS P., SMIRNOV S.: Large-scale atmospheric pressure chemical vapor deposition of graphene, Carbon, *2013*, 54(4), 58–67

[36] VAN GILS S., LE PEN C., HUBIN A., TERRYN H., STIJNSB E.: Electropolishing of copper in H_3PO_4 *ex situ* and *in situ* optical characterization, J. Electrochem. Soc., *2007*, 154(3), C175–C180

[37] SHIVAREDDY S., BAE S., BRANKOVIC S.: Cu surface morphology evolution during electropolishing, Electrochem. Solid State Lett., *2008*, 11(1), D13–D17

[38] WOOD J.D., SCHMUCKER S.W., LYONS A.S., POP E., LYDING J.W.: Effects of polycrystalline Cu substrate on graphene growth by chemical vapor deposition, Nano Lett., *2011*, 11(1), 4547–4554

[39] VLASSIOUK I., REGMI M., FULVIO P., DAI S., DATSKOS P., ERES G., SMIRNOV S.: Role of hydrogen in chemical vapor deposition growth of large single-crystal graphene, ACS Nano, *2011*, 5 (7), 6069–6076

[40] FLORES C.B., LÓPEZ D.M.: Multilayer graphene synthesized by CVD using liquid hexane as the carbon precursor, World J. Cond. Matter Phys., *2011*, 1(4), 157–160

[41] KIRKLAND N.T., SCHILLER T., MEDHEKAR N., BIRBILIS N.: Exploring graphene as a corrosion protection barrier, Corr. Sci., *2012*, 56(1), 1–4

[42] KOUSALYA A.S., KUMAR A., PAUL R., ZEMLYANOV D., FISHER T.S.: Graphene: An effective oxidation barrier coating for liquid and two-phase cooling systems, Corr. Sci., *2013*, 69(1), 5–10

[43] KALITA G., AYHAN M.E., SHARMA S., SHINDE S.M., GHIMIRE D., WAKITA K., UMENO M., TANEMURA M.: Low temperature deposited graphene by surface wave plasma CVD as effective oxidation resistive barrier, Corr. Sci., *2014*, 78(1), 183–187

[44] FRIEDRICH H., JACOBY G., MEISTER C.G.: Quantum reflection by Casimir–van der Waals potential tails, Phys. Rev. A, *2002*, 65(3), 032902–032915

[45] SUTTER E., ALBRECHT P., CAMINO F.E., SUTTER P.: Monolayer graphene as an ultimate chemical passivation layer for arbitrarily shaped metal surfaces, Carbon, *2010*, 48(15), 4414–4420

[46] SINGH RAMAN R.K., BANERJEE P.C., LOBO D.E., GULLAPALLI H., SUMANDASA M., KUMAR A., CHOUDHARY L., TKACZ R., AJAYAN P.M., MAJUMDER M.: Protecting copper from electrochemical degradation by graphene coating, Carbon, *2012*, 50(11), 4040–4045

[47] HSIEH Y.-P., HOFMANN M., CHANG K.-W., JHU J.G., LI Y.-Y., YAO CHEN K., YANG C.C., CHANG W.-S., CHEN L.-C.: Complete corrosion inhibition through graphene defect passivation, ACS Nano, *2014*, 8(1), 443–448

[48] HUH J.-H., KIM S.H., CHU J.H., KIM S.Y., KIM J.H., KWON S.-Y.: Enhancement of seawater corrosion resistance in copper using an acetone-derived graphene coating, Nanoscale, *2014*, 6(8), 4379–4386

[49] NAYAK P.K., HSU C.-J., WANG S.-C., J.C., SUNG HUANG J.-L.: Graphene coated Ni films: A protective coating, Thin Solid Films, *2013*, 529(1), 312–316

[50] XIA J., CHEN F., LI J., TAO N.: Measurement of the quantum capacitance of graphene, Nat. Nanotechnol., 2009, 4(8), 505–509

[51] WANG S., ZHANG L., XIA Z., ROY A., CHANG D.W., BAEK J.-B., DAI L.: BCN graphene as an efficient metal-free electrocatalyst for the oxygen reduction reaction, Angew. Chem. Int. Ed., *2012*, 51(17), 4209–4212

[52] ERNEST Y.: Dioxygen electrocatalysis: mechanism in relation to catalyst structure, J. Mol. Catal., *1986*, 38(1-2), 5–25

[53] SREEVATSA S., BANERJEE A., HAIM G.: Graphene as a permeable ionic barrier, ECS Trans., *2009*, 19(5), 259–264

[54] ROBINSON Z.R., TYAGI P., MURRAY T.M., VENTRICE C.A., CHEN S., MUNSON A., MAGNUSON C.W., RUOFF R.S.: Substrate grain size and orientation of Cu and Cu–Ni foils used for the growth of graphene films, J. Vac. Sci. Technol. A, Vac. Surf. Films, *2011*, 30(1), Art. No. 011401

[55] LI X., CAI W., COLOMBO L., RUOFF R.S.: Evolution of graphene growth on Ni and Cu by carbon isotope labeling, Nano Lett., *2009*, 9(12), 4268–4272

[56] SRIVASTAVA A., GALANDE C., CI L., SONG L., RAI C., JARIWALA D., KELLY K.F., AJAYAN P.M.: Multilayer graphene synthesized by CVD using liquid hexane as the carbon precursor, Chem. Mater., *2010*, 22(11), 3457–3461

[57] MIAO C., ZHENG C., LIANG O., XIE Y.-H.: Physics and applications of graphene - experiments, Ed. MIKHAILOV S., InTech Europe, Rijeka, Croatia, *2011*

[58] ZHOU X.: Graphene oxidation barrier coating, Ph.D. Thesis, University of Colorado, Boulder, CO USA, *2011*

[59] SCHRIVER M., REGAN W., GANNETT W.J., ZANIEWSKI A.M., CROMMIE M.F., ZETTL A.: Graphene as a long-term metal oxidation barrier: worse than nothing, ACS Nano, *2013*, 7(7), 5763–5768

[60] HADDAD F.S., THAKRAR R.R., HART A.J., SKINNER J.A., NARGOL A.V.F., NOLAN J.F., GILL H.S., MURRAY D.W., BLOM A.W., CASE C.P.: Metal-on-metal bearings, J. Bone Joint Surg. Br., *2011*, 93(B), 572–579

[61] KOROVESSIS P., PETSINIS G., REPANTI M., REPANTIS T.: Metallosis: After contemporary metal-on-metal total hip arthroplasty five to nine-year follow-up, J. Bone Joint Surg. Am., *2006*, 88(6), 1183–1191

[62] KAW M., SINGH S., GAGNEJA H., AZAD P.: Role of self-expandable metal stents in the palliation of malignant duodenal obstruction, Surg. Endosc., *2003*, 17(4), 646–650

[63] BARON T.H.: Expandable metal stents for the treatment of cancerous obstruction of the gastrointestinal tract, New Engl. J. Med., *2001*, 344(22), 1681–1687

[64] CORTIZO M., DEMELE M., CORTIZO A.: Metallic dental material biocompatibility in osteoblastlike cells, Biol. Trace Elem. Res., *2004*, 100(2), 151–168

[65] CRAIG R.G., POWERS J.M. (Eds.): Restorative dental materials, 11th Ed., Mosby Inc., St Louis, MO, USA, *2010*

[66] TONDATO F., NG D.W., SRIVATHSAN K., ALTEMOSE G.T., HALYARD M.Y., SCOTT L.R.: Radiotherapy-induced pacemaker and implantable cardioverter defibrillator malfunction, Expert Rev. Med. Dev., *2009*, 6(3), 243–249

[67] ISHII K., KODANI E., MIYAMOTO S., OTSUKA T., HOSONE M., OGATA K., SATO W., MATSUMOTO S., TADERA T. IBUKI KUSAMA Y., ATARASHI H.: Pacemaker Contact Dermatitis: The effective use of a polytetrafluoroethylene sheet, Pacing Clin. Electrophysiol., *2006*, 29(11), 1299–1302

[68] SCHMIDT C., IGNATIUS A.A., CLAES L.E.: Proliferation and differentiation parameters of human osteoblasts on titanium and steel surfaces, J. Biomed. Mater. Res., *2001*, 54(2), 209–215

[69] KURTZ S.M., MURATOGLU O.K., EVANS M., EDIDIN A.A.: Advances in the processing, sterilization, and crosslinking of ultra-high molecular weight polyethylene for total joint arthroplasty, Biomaterials, *1999*, 20(18) 1659–1688

[70] DAVIS J.R.: Handbook of materials for medical devices, First Ed., ASM International, Materials Park, OH, USA, *2003*

[71] ATWOOD R.C., LEE P.D., CURTIS R.V.: Modeling the surface contamination of dental titanium investment castings, Dent. Mater., *2005*, 21(2), 178–186

[72] CAICEDO M.S., PENNEKAMP P.H., MCALLISTER K., JACOBS J.J., HALLAB N.J.: Soluble ions more than particulate cobalt-alloy implant debris induce monocyte costimulatory molecule expression and release of proin flammatory cytokines critical to metal-induced lymphocyte reactivity, J. Biomed. Mater. Res., *2010*, A93A(4), 1312–1321

[73] ROMESBURG J.W., WASSERMAN P.L., SCHOPPE C.H.: Metallosis and Metal-Induced Synovitis Following Total Knee Arthroplasty, Rev. Radiograp. CT Findings, *2010*, 4(9), 7–17

[74] JACOBS J.J., HALLAB N.J.: Loosening and osteolysis associated with metal-on-metal bearings: A local effect of metal hypersensitivity?, J. Bone Joint Surg. Am., *2006*, 88(6), 1171–1172

[75] YANG L., SHELDON B.W., WEBSTER T.J.: Orthopedic nano diamond coatings: Control of surface properties and their impact on osteoblast adhesion and proliferation, J. Biomed. Mater. Res., *2009*, A91A(2), 548–556

[76] PECHEVA E., PRAMATAROVA L., FINGAROVA D., HIKOV T., DINEVA I., KARAGYOZOVA Z., STAVREV S.: Advanced materials for metal implant coatings, J. Optoelectron. Adv. Mater., *2009*, 11(9), 1323–1326

[77] PODILA R., MOORE T., ALEXIS F., RAO A.M.: Graphene coatings for enhanced hemo-compatibility of nitinol stents, Rev. Soc. Chem. Adv., *2013*, 3(1), 1660–1665

[78] PODILA R., MOORE T., ALEXIS F.R.: Graphene coatings for biomedical implants, J. Vis. Exp., *2013*, 73(1), Art. No. e50276

[79] ZHANG W., LEE S., MCNEAR K.L., CHUNG T.F., LEE S., LEE K., CRIST S.A., RATLIFF T.L., ZHONG Z. YANG C.: Use of graphene as a protection film in biological environments, Sci. Rep. *2014*, 4(4), 4097

[80] NEUHAUSER E.F., LOEHR R.C., MILLIGAN D.L., MALECKI M.R.: Toxicity of metals to the earthworm *Eisenia fetida*, Biol. Fert. Soils, *1985*, 1(3), 149–152

[81] KOENIG S.P., BODDETI N.G., DUNN M.L., BUNCH J.S.: Ultrastrong adhesion of graphene membranes, Nat. Nano., 2011, 6(9), 543–546

[82] CAPRIOLI F., DECKER F., MARRANI A.G., BECCARI M., CASTRO V.D.: Copper protection by self-assembled monolayers of aromatic thiols in alkaline solutions, Phys. Chem. Chem. Phys., *2010*, 12(32), 9230–9238

[83] LUSK A.T., JENNINGS G.K.: Characterization of self-assembled monolayers formed from sodium s-alkyl thiosulfates on copper, Langmuir, *2001*, 17(25), 7830–7836

[84] BRINKER C.J., HURD A.J., SHUNK P.R., FRYE G.C., ASHLEY C.S.: Review of sol-gel thin film formation, J. Non-Cryst. Solids, *1992*, 147-148(1), 424–436

[85] SCRIVEN L.E.: in Better Ceramics through Chemistry III, Eds., BRINKER C.J., CLARK D.E., ULRICH D.R., The Materials Research Society, Pittsburgh, PA USA, *1988*, p.717

[86] LANDAU L.D., LEVICH B.G.: Dragging of a liquid by a moving plate, Acta Physiochim. U.R.S.S., *1942*, 17, 42–54

[87] DISLICH H.: Sol-gel: science, processes and products, J. Non-Cryst. Solids, *1997*, 80(1-3), 115–121

[88] ARFSTEN N.J., ERBLE A., OTTO J., REICH A.: Investigations on the angle-dependent dip coating technique, ADDC, for the for the Production of Optical Filters, J. Sol-Gel Sci. Techol., *1997*, 8(1-3), 1099–1104

[89] SCHMIDT H., in Chemistry, Spectroscopy and Application of sol-gel glasses, Ed., REISFELD R. Springer-Verlag, Berlin, Germany, *1992*, pp.119–152

[90] MEYERHOFER D.: Characteristics of resist films produced by spinning, J. Appl. Phys., *1978*, 49(7), 3993–3997

[91] LAI J.H.: An investigation of spin coating of electron resists, Polym. Eng. Sci., *1979*, 19(15), 1117–1121

[92] CHEN B.T.: Investigation of the solvent-evaporation effect on spin coating of thin films, Polym. Eng. Sci., *1983*, 23(7), 399–403

[93] VAN BOMMEL J.: Optical coatings for computer monitors and TV screens, Glass Res., *1997*, 10, 7

[94] O'BRIEN S.B.G., SCHWARTZ L.W.: Theory and modeling of thin film flows, Encyclopedia of Surface and Colloid Science, Ed. HUBBARD A., Marcel Dekker, New York, *2002*, pp. 5283–5297

[95] EVANS P.L., SCHWARTZ L.W., ROY R.V.: Three-dimensional solutions for coating flow on a rotating horizontal cylinder: Theory and experiment, Phys. Fluids, *2005*, 17(7), Art. No. 072102

[96] FLOCH H.G., BELLEVILLE G., PRIOTTON J.J.: Sol-Gel Optical Coatings For Lasers., Am. Ceram. Soc. Bull., *1995*, 74(10), 60–63

[97] FLOCH H.G., BELLEVILLE P.F.: Scratch-Resistant Single-Layer Antireflective Coating By A Low Temperature Sol-Gel Route, Proc. Spie, *1992*, 1758, 135–149

[98] MITSOULIS E., ATHANASOPOULOS G.: Numerical Simulation Of Blade-Over-Roll Coating Forming Flows, Comp. Met. Mater., *2010*, 10(4), 214–224

[99] NODA K., YAMAGAMI YAMAMOTO M., M., SATO H., ITAYA H., OKAJIMA A., YAMADA M.: Thin Film Formation By Direct Reverse Roll-Coating On Plastic Web, Jpn. J. Appl. Phys., *2003*, 42(1), 5722–5725

[100] ALONSO S., REÂGLAT O., BERTRAND F., CHOPLIN L., TANGUY P.A.: Process viscosity in reverse roll coating, Trans. I. Chem. E, *2001*, 79(Part A), 128–136

[101] EMSLIE A.G., BONNER F.T., PECK C.G.: Flow of a viscous liquid on a rotating disk, J. Appl. Phys., *1958*, 29(5), 858–862

[102] ACRIVOS A., SHAH M.J., PETERSEN E.E.: On the flow of a non-Newtonian liquid on a rotating disk, J. Appl. Phys., *1960*, 31(6), 963–968

[103] KIM D.-Y., SINHA-RAY S., PARK J.-J., LEE J.-G., CHA Y.-H., BAE S.-H., AHN J.-H., JUNG Y.C., KIM S.M., YARIN A.L., YOON S.S.: Self-healing reduced graphene oxide films by supersonic kinetic spraying, Adv. Funct. Mater. *2014*, 24(31), 4986–4995

[104] WANG S.J., GENG Y., ZHENG Q., KIM J.-K.: Fabrication of highly conducting and transparent graphene films, Carbon, *2010*, 48(6), 1815–1823

[105] YOON S., KIM H.J., LEE C.: Fabrication of an automotive heat exchanger using a kinetic spraying process, Surf. Coat. Technol., *2007*, 201(1) 9524–9532

[106] DZHURINSKIY D., MAEVA E., LESHCHINSKY EV., MAEV, R.GR.: Corrosion Protection of Light Alloys Using Low Pressure Cold Spray, J. Therm. Spray Technol., *2012*, 21(2) 304–313

[107] HUSSAIN T., MCCARTNEY D.G., SHIPWAY P.H., MARROCCO T.: Corrosion behavior of cold sprayed titanium coatings and free standing deposits, J. Therm. Spray Technol., *2011*, 20(1-2), 260–274

[108] YARIN A.L., KOOMBHONGSE S., RENEKER D.H.: Taylor cone and jetting from liquid droplets in the electrospinning of nanofibers, J. Appl. Phys., *2001*, 90(9), 4836–4846

[109] SHIN Y.M., HOHMAN M.M., BRENNER M.P., RUTLEDGE G.C.: Experimental characterization of electrospinning: the electrically forced jet and instabilities, Polymer, *2001*, 42(25), 9955– 9967

[110] MENCHACA C., MANOUN B., MARTÍNEZ-BARRERA G., CASTANO V.M., LÓPEZ-VALDIVIA H.: In situ high-temperature Raman study of crystalline nylon 6,12 fibers gamma-irradiated in an argon atmosphere, J. Phys. Chem. Solids, *2006*, 67 (9), 2111– 2118

[111] CAMPOS C.M., PÉREZ C.G., CASTAÑEDA I., GARCÍA-SÁNCHEZ M.A., GUARDIÁN R., URUCHURTU J.: Nylon/graphene oxideelectrospun composite coating, Internat. J. Polym. Sci., *2013*, 1, 1-9

[112] KAYA C.: Al_2O_3-Y-TZP/Al_2O_3 functionally graded composites of tubular shape from nano-sols using double-step electrophoretic deposition, J. Eur. Ceram. Soc., *2003*, 23(10), 1655–1660

[113] PUT S., VLEUGELS J., VAN DER BIEST O.: Functionally graded WC–co materials produced by electrophoretic deposition, Scr. Mater., *2001*, 45(10), 1139–1145

[114] SARKAR P., DATTA S., NICHOLSON P.S.: Functionally graded ceramic/ceramic and metal/ceramic composites by electrophoretic deposition, Compos. B-Eng., *1997*, 28(1), 49–56

[115] LEE S.B., CHOI O., LEE W., YI J.W., KIM B.S., BYUN J.H., YOON M.K., FONG H., THOSTENSON E.T., CHOU T.W.: Processing and characterization of multi-scale hybrid composites reinforced with nanoscale carbon reinforcements and carbon fibers, Compos. Part A, *2001*, 42(4), 337–344

[116] ZHITOMIRSKY I.: Hydroxyapatite coatings and fibers, Mater. Lett., *2000*, 42, 262

[117] YOU C., JIANG D.L., JAN S.H.: SiC/TiC laminated structure shaped by electrophoretic deposition, Ceram. Int., *2004*, 30(5), 813–815

[118] VAN DE PERRE L., VAN DER BIEST O.: Composite SiC-graphite interlayers for crack deflection in ceramic laminates, Silic. Ind., *1998*, 63, 39–43

[119] KAYA C., KAYA F., SU B., THOMAS B., BOCCACCINI A.R.: Structural and functional thick ceramic coatings by electrophoretic deposition, Surf. Coat. Technol., *2005*, 191(1), 303–310

[120] YANAGIDA A., NAKAJIMA Y., KAMESHIMA N., YOSHIDA T., WATANABE K., OKADA K.: Preparation of a crack-free rough titania coating on a stainless steel mesh by electrophoretic deposition, Mater. Res. Bull., *2005*, 40(1), 1335–1344

[121] PEIRO A.M., BRILLA E., PERAL J., DOMENECH X., AYLLON J.A.: Electrochemically assisted deposition of titanium dioxide on aluminium cathodes, J.Mater.Chem., *2002*, 12(1), 2769–2773

[122] BOCCACCINI A.R., ROETHER J.A., THOMAS B.J.C., SHAFFER M.S.P., CHAVEZ E., STOLL E., MINAY E.J.: 'The electrophoretic deposition of inorganic nanoscaled materials, J. Ceram. Soc. Jpn., *2006*, 114(1325), 1–14

[123] BESRA L., LIU M.: A review on fundamentals and applications of electrophoretic deposition number , EPD , Prog. Mater. Sci., *2007*, 52, 1

[124] VU Q.-T., PAVLIK M., HEBESTREIT N., PFLEGER J., RAMMELT U., PLIETH W.: Electrophoretic deposition of nanocomposites formed from polythiophene and metal oxides, Electrochim. Acta, *2005*, 51(6), 1117–1124

[125] PECH-RODRÍGUEZ W.J., GONZÁLEZ-QUIJANO D., VARGAS-GUTIÉRREZ G., RODRÍGUEZ-VARELA F.J.: Deposition of Vulcan XC-72 coatings on stainless steel bipolar plates by reverse pulsed dc voltage electrophoretic deposition number, EPD, for fuel cell applications, ECS Trans., *2014*, 58(12), 33–39

[126] LIH E.T.Y., ZAID R.T.M., LING T.L., CHONG K.F.: Facile corrosion protection coating from graphene, Int. J. Chem. Engin. Appl., *2012*, 3(6), 453–455

[127] SINGH B.P., NAYAK S., NANDA K.K., JENA B.K., BHATTACHARJEE S., BESRA L.: The production of a corrosion resistant graphene reinforced composite coating on copper by electrophoretic deposition, Carbon, *2013*, 61(1), 47–56

[128] HE W., ZHU L., CHEN H., NAN H., LI W., LIU H., WANG Y.: Electrophoretic deposition of graphene oxide as a corrosion inhibitor for sintered NdFeB, Appl. Surf. Sci., *2013*, 279(1), 416–423

[129] KOLBE H.: Decomposition of valeric acid by an electric current, Annal. Chem. Pharm., *1848*, 64(1), 339–341 (in German)

[130] KOLBE H.: Studies of the electrolysis of organic compounds, Annal. Chem. Pharm., *1849*, 69(1), 257–294 (in German)

[131] SINGH B.P., JENA B.K., BHATTACHARJEE S., BESRA L.: Development of the oxidation and corrosion resistanr hydrophobic graphene oxide-polymer composite coating on copper, Surf. Coat. Technol., *2013*, 232(1), 475–481

[132] WANG M., DUONG L.D., OH J.-S., MAI N.T., KIM S., HONG S., WANG T.H., LEE Y.K., NAM J.-D.: Large-Area, conductive and flexible reduced graphene oxide number, RGO, membrane fabricated by electrophoretic deposition number, EPD, ACS Appl. Mater. Interfaces, *2014*, 6(3), 1747–1753

[133] MEYERS J.P., DARLING R.M.: Model of carbon corrosion in PEM fuel cells, J. Electrochem. Soc., *2006*, 153(8), A1432–A1442

[134] PRABAKAR S.J.R., HWANG Y.-H., BAE E.G., LEE D.K., PYO M.: Graphene oxide as a corrosion inhibitor for the aluminium current collector in lithium ion batteries, Carbon, *2013*, 52(1), 128–136

[135] LOGAN B.E., HAMELERS B., ROZENDAL R., SCHRÖDER U., KELLER J., FREGUIA S., AELTERMAN P., VERSTRAETE W., RABAEY K.: Microbial fuel cells: methodology and technology, Environ. Sci. Technol., *2006*, 40(17), 5181–5192

[136] KRISHNAMURTHY A., GADHAMSHETTY V., MUKHERJEE R., CHEN Z., REN W., CHENG H-M., KORATKAR N.: Passivation of microbial corrosion using a graphene coating, Carbon, *2013*, 56(1), 45–49

[137] SAHU S.C., SAMANTARA A.K., SETH M., PARWAIZ S., SINGH B.P., RATH P.C., JENA B.K.: A facile electrochemical approach for the development of highly corrosion protective coatings using graphene nanosheets, Electrochem. Commun., *2013*, 32(1), 22–26

[138] WESSLING B.: Passivation of metals by coating with polyaniline: Corrosion potential shift and morphological changes, Adv. Mater., *1994*, 6(3), 226–228

[139] DEBERRY D.W.: Modification of the electrochemical and corrosion behavior of stainless steels with an electroactive coating, J. Electrochem. Soc., *1985*, 132(5), 1022–1026

[140] WEI Y., WANG J., JIA X., YEH J.M., SPELLANE P.: Polyaniline as corrosion protection coatings on cold rolled steel, Polymer, *1995*, 36(23), 4535–4537

[141] YEH J.M., LIOU S.J., LAI C.Y., WU P.C., TSAI T.Y.: Enhancement of the corrosion protection effect in polyaniline *via* the formation of polyaniline-clay nanocomposite materials, Chem. Mater., *2001*, 13(3), 1131–1136

[142] IONITA M., PRUNA A.: Polypyrrole/carbon nanotube composites: Molecular modeling and experimental investigation as an anti-corrosive coating, Prog. Org. Coat., *2011*, 72(4), 647–652

[143] MARTINA V., DE RICCARDIS M.F., CARBONE D., ROTOLO P., BOZZINI B., MELE C.: Electrodeposition of polyaniline–carbon nanotubes composite films and investigation on their role in corrosion protection of austenitic stainless steel by SNIFTIR analysis: J. Nanopart. Res., *2011*, 13(11), 6035–6047

[144] SALAM M.A., AL-JUAID S.S., QUSTI A.H., HERMAS A.A.: Electrochemical deposition of a carbon nanotube-poly o-phenylenediamine, composite on a stainless steel surface, Synth. Met., *2011*, 161(1-2), 153–157

[145] HU S.T., KONG X.H., YANG H., SUN R.H.: Anticorrosive films prepared by incorporating permanganate modified carbon nanotubes into the waterborne polyurethane polymer, Adv. Mater. Res., *2011*, 189–193, 1157–1162

[146] DE RICCARDIS M.F., MARTINA V., CARBONE D., ROTOLO P.: Functional characterisations of hybrid nanocomposite films based on polyaniline and carbon nanotubes, Adv. Sci. Technol., *2013*, 79(1), 81–86

[147] GERGELY A., PÁSZTI Z., MIHÁLY J., DROTÁR E., TÖRÖK T.: Galvanic corrosion prevention of the zinc-rich hybrid coatings facilitated by the percolating structure of the carbon nanotubes Part II: Protection properties and mechanism of the hybrid coatings, Prog. Org. Coat., *2014*, 77(2), 412–424

[148] GERGELY A., PÁSZTI Z., HAKKEL O., MIHÁLY J., KÁLMÁN E.: Corrosion protection of cold-rolled steel with alkyd paint coatings composited with various microstructure arranged polypyrrole-modified nano-size alumina and carbon nanotubes, Mater. Sci. Eng. B, *2012*, 177(18), 1571–1682

[149] GERGELY A., PÁSZTI Z., HAKKEL O., BERTÓTI I., MIHÁLY J., TÖRÖK T.: Investigation of modified carbon nanotubes/aluminium-oxide monohydrate containing zinc-rich hybrid paint coatings, Korr. Figy., *2013*, 53(1), 3–24 (in Hungarian)

[150] GERGELY A., TÖRÖK T.: Optimally balanced active-passive corrosion protection by zinc-rich paint coatings featuring proper hybrid formulation with polypyrrole modified carbon nanotubes, Mater. Sci. For., *2013*, 752(1), 275–283

[151] GERGELY A., PÁSZTI Z., BERTÓTI I., TÖRÖK T., MIHÁLY J., KÁLMÁN E.: Novel zinc-rich epoxy paint coatings with hydrated alumina and carbon nanotubes supported polypyrrole for corrosion protection of low carbon steel Part II: Corrosion prevention behaviour of the hybrid paint coatings, Mater. Corr., *2013*, 64(12), 1091–1103

[152] GERGELY A., TÖRÖK T., PÁSZTI Z., BERTÓTI I., MIHÁLY J., KÁLMÁN E.: Zinc-rich paint coatings containing either ionic surfactant-modified or functionalized multi-walled carbon nanotube-supported polypyrrole utilized to protect cold-rolled steel against corrosion, Nova Science Publishers, Inc., Part II: Application of Carbon nanotubes, *2012*, Chapter 10th, pp. 211–258.

[153] JEON H., PARK J., SHON M.: Corrosion protection by epoxy coating containing multi-walled carbon nanotubes, J. Ind. Engin. Chem., *2013*, 19(3), 849–853

[154] SHOW Y., NAKASHIMA T., FUKAMI Y.: Anticorrosion coating of carbon nanotube/polytetra-fluoroethylene composite film on the stainless steel bipolar plate for proton exchange membrane fuel cells, J. Nanomater., *2013*, Article ID 378752

[155] DESHPANDE P.P., VATHARE S.S., VAGGE S.T., TOMŠÍK E., STEJSKAL J.: Conducting polyaniline/multi-wall carbon nanotubes composite paints on low carbon steel for corrosion protection: Electro-chemical investigations, Chem. Pap., *2013*, 67(8), 1072–1078

[156] SREEVATSA S.: Carbon nanotube electronic structures as anti-corrosion coatings, PhD Thesis, State University of New Jersey, Newark, USA, 2009

[157] PRAVEEN B.M., VENKATESHA T.V., ARTHOBA NAIK Y., PRASHANTHA K.: Corrosion studies of carbon nanotubes–Zn composite coating, Surf. Coat. Technol., *2007*, 201(12), 5836–5842

[158] CHEN X.H., CHEN C.S., XIAO H.N., CHENG F.Q., ZHANG G., YI G.J.: Corrosion behavior of carbon nanotubes–Ni composite coating, Surf. Coat. Technol., *2005*, 191(2-3), 351–356

[159] MONTEMOR M.F., FERREIRA M.G.S.: Analytical characterisation and corrosion behaviour of bis-aminosilane coatings modified with carbon nanotubes activated with rare-earth salts applied on AZ31 Magnesium alloy, Surf. Coat. Technol., *2008*, 202(19), 4766–4774

[160] RAFIEE M.A., RAFIEE J., WANG Z., SONG H., YU Z.Z., KORATKAR N.: Enhanced mechanical properties of nanocomposites of low graphene content, ACS Nano, *2009*, 3(12), 3884–3890

[161] ZHANG W.L., LIU Y.D., CHOI H.J.: Fabrication of semiconducting graphene oxide/polyaniline composite particles and their electrorheological response under an applied electric field, Carbon, *2012*, 50(1), 290–296

[162] ZHANG W.L., PARK B.J., CHOI H.J.: Colloidal graphene oxide/polyaniline nanocomposite and its electrorheology, Chem. Commun., *2010*, 46(30), 5596–5598

[163] STANKOVICH S., PINER R.D., NGUYEN S.T., RUOFF R.S.: Synthesis and exfoliation of isocyanate-treated graphene oxide nanoplatelets, Carbon, *2006*, 44(15), 3342–3347

[164] COMPTON O.C., KIM S., PIERRE C., TORKELSON J.M., NGUYEN S.T.: Crumpled graphene nanosheets as highly effective barrier property enhancers, Adv. Mater., *2010*, 22(42), 4759–4763

[165] KIM H.W., MIURA Y., MACOSKO C.W.: Graphene/polyurethane composites for improved gas barrier and electrical conductivity, Chem. Mater., *2010*, 22(11), 3441–3450

[166] KIM H.W., MACOSKO C.W.: Dispersing organoclay in polystyrene melts: roles of stress and diffusion, Macromolecules, *2008*, 41(9), 3317–3327

[167] KALAITZIDOU K., FUKUSHIMA H., DRZAL L.T.: Multifunctional polypropylene composites produced by the incorporation of exfoliated graphite nanoplatelets, Carbon, *2007*, 45(7), 1446–1452

[168] KIM H.W., ABDALA A.A., MACOSKO C.W.: Graphene/polymer composites, Macromolecules, *2010*, 43(16), 6515–6530

[169] POTTS J.R., DREYER D.R., BIELAWSKI C.W., RUOFF R.S.: Graphene-based polymer composites, Polymer, *2011*, 52(1), 5–25

[170] CHANG C.-H., HUANG T.-C., PENG C.-W., YEH T.-C., LU H.-I., HUNG W.-I., WENG C.-J., YANG T.-I., YEH J.-M.: Novel anticorrosion coatings prepared from polyaniline/graphene composites, Carbon, *2012*, 50(14), 5044–5051

[171] LIU T., YIN Y., CHEN S., CHANG X., CHENG S.: Super-hydrophobic surfaces improve corrosion resistance of copper in seawater, Electrochim. Acta, *2007*, 52(11), 3709–3882

[172] ZHANG F., ZHAO L., CHEN H., XU S., EVANS D.G., DUAN X.: Corrosion resistance of superhydrophobic layered double hydroxide films on aluminium, Angew. Chem. Int. Ed., *2008*, 47(13), 2466–2469

[173] ZHANG F., CHEN S., DONG L., LEI Y., LIU T., Y.YIN: Preparation of superhydrophobic films on titanium as effective corrosion barriers, Appl. Surf. Sci., *2011*, 257(7), 2587–2591

[174] RAO A.V., LATTHE S., MAHADIK S., KAPPENSTEIN C.: Mechanically stable and corrosion resistant superhydrophobic sol–gel coatings on copper substrate, Appl. Surf. Sci., *2011*, 257(13), 5772–5776

[175] WENG C.J., CHANG C.H., PENG C.W., CHEN S.W., YEH J.M., HSU C.L., WEI Y.: Advanced anticorrosive coatings prepared from the mimicked Xanthosomasagittifolium leaf-like electroactive epoxy with synergistic effects of superhydrophobicity and redox catalytic capability, Chem. Mater., *2011*, 23(8), 2075–2083

[176] YANG T.I., PENG C.W., LIN Y.L., WENG C.J., EDGINGTON G., MYLONAKIS A., HUANG T.-C., HSU C.-H., YEH J.-M., WEI Y.: Synergistic effect of electroactivity and hydrophobicity on the anticorrosion property of room-temperature-cured epoxy coatings with multi-scale structures mimicking the surface of Xanthosomasagittifolium leaf, J. Mater. Chem., *2012*, 22(31), 15845–15852

[177] HIL R., MA M.: Superhydrophobic surfaces, Curr. Opin. Colloid Interface Sci., *2006*, 11(4), 193–202

[178] CHANG K.-C., HSU M.-H., LU H.-I., LAI M.-C., P LIU.-J., HSU C.-H., JI W.-F., CHUANG T.-L., WEI Y., YEH J.-M., LIU W.-R.: Room-temperature cured hydrophobic epoxy/graphene composites as a corrosion inhibitor for cold-rolled steel, Carbon, *2014*, 66(1), 144–153

[179] TURHAN M.C., LI Q., JHA H., SINGER R.F., VIRTANEN S.: Corrosion behaviour of multiwall carbon nanotube/magnesium composites in 3.5% NaCl, Electrochim. Acta, *2011*, 56(20), 7141–7148

[180] LI Q., TURHAN M.C., ROTTMAIR C.A., SINGER R.F., VIRTANEN S.: Influence of MWCNT dispersion on the corrosion behaviour of their Mg composites, Mater. Corr., *2012*, 63(5), 384–387

[181] FUKUDA H., SZPUNAR J.A., KONDOH K., CHROMIK R.: The influence of carbon nanotubes on the corrosion behaviour of AZ31B magnesium alloy, Corr. Sci., *2010*, 52(12), 3917–3923

[182] AUNG N.N., ZHOU W., GOH C.S., MUI S., NAI L., WEI J.: Effect of carbon nanotubes on the corrosion of Mg–CNT composites, Corr. Sci., *2010*, 52(5), 1551–1553

[183] ZHANG M., YAN Y., GONG K., MAO L., GUO Z., CHEN Y.: Electrostatic layer by layer assembled carbon nanotube mutilayer film and its catalytic activity for the oxygen reduction reaction, Langmuir, *2004*, 20(20), 8781–8785

[184] JÜRMANN G., TAMMEVESKI K.: Electroreduction of oxygen on multi-walled carbon nanotube modified highly oriented pyrolytic graphite electrodes in an alkaline solution, J. Electroanal. Chem., *2006*, 597(2), 119–126

[185] WANG S., IYYAMPERUMAL E., ROY A., XUE Y., YU D., DAI L.: Vertically aligned BCN nanotubes as efficient metal-free electrocatalysts for the oxygen reduction reaction: A synergetic effect by co-doping with boron and nitrogen, Angew. Chem., *2011*, 123(49), 11960–11964

[186] KUMAR C.M.P., VENKATESHA T.V., SHABADI R.: Preparation and corrosion behavior of Ni and Ni–graphene composite coatings, Mater. Res. Bull., *2013*, 48(4), 1477–1483

[187] DENNIS R.V., VIYANNALAGE L.T., GAIKWAD A.V., ROUT T.K., BANERJEE S.: Graphene nanocomposite coatings for protecting low-alloy steels from corrosion, Am. Ceram. Soc. Bull., *2013*, 92(5), 18–24

[188] ROUT T.K., GAIKWAD A.V., DINGEMANS T.A.: A method of preparing a polyetherimide coating on a metallic substrate, World Intellectual Property Organization, Pat. No. WO2011035920, A1, *2011*

[189] ROUT G.K., GAIKWAD A.V., LEE V., BANERJEE S.: Hybrid nanocomposite coatings for corrosion protection of low carbon steel: A substrate-integrated and scalable active–passive approach, J. Mater. Res., *2011*, 26(6), 837–844

[190] ROUT T.K., JHA G., SINGH A.K., BANDYOPADHYAY N., MOHANTY O.N.: Development of conducting polyaniline coating: A novel approach to superior corrosion resistance, Surf. Coat. Technol., *2003*, 67(1), 16–24

[191] KUMAR S., SUN L.L., CACERES S., LI B., WOOD W., PERUGINI A., MAGUIRE R.G., ZHONG W.H.: Dynamic synergy of graphitic nanoplatelets and multi-walled carbon nanotubes in polyetherimide nanocomposites, Nanotechnology, *2010*, 21(10), 105702–105710

[192] WILSON D., STENZENBERGER H.D., HERGENROTHER P.M.: Polyimides, Chapman and Hall, London, U.K., *1990*

[193] KUMAR S., LI B., CACERES S., MAGUIRE R.G., ZHONG W.-H.: Dramatic property enhancement in polyetherimide using low-cost commercially functionalized multi-walled carbon nanotubes *via* a facile solution processing method, Nanotech., *2009*, 20(46), 465708–465716

[194] VON BAECKMANN W., SCHWENK W., PRINZ W. (Eds.): Handbook of corrosion protection, Theory and practice of electrochemical protection processes, Third Edition, Golf Publishing Company, Houston TX, USA, *1997*

HUNGARIAN JOURNAL
OF INDUSTRY AND CHEMISTRY
VESZPRÉM
Vol. 41(2) pp. 109–114 (2013)

INVESTIGATIONS OF BIO-GASOIL PRODUCTION

PÉTER SOLYMOSI, ✉ ZOLTÁN VARGA, AND JENŐ HANCSÓK

MOL Department of Hydrocarbon- and Coal Processing, University of Pannonia, Egyetem u. 10., Veszprém, 8200, HUNGARY
✉Email: solymosip@almos.uni-pannon.hu

Liquid engine fuels are the main source of power for transportation in the passenger sector. It is the projection of the European Union (EU) to reach 10% utilisation of renewable fuels by 2020. To achieve this goal the EU created the 2003/30/EC and furthermore the 2009/28/EC Directives. For example, the feedstocks of these renewable engine fuels can be non-edible oil plant hybrids, such as rapeseed oils with high euric acid content obtained from special hybrids of rape (e.g. *Brassica napus*) waste lards (used cooking oil and slaughterhouse lards). If the preconditions of utilisation are given with respect to the sustainability and technical compatibility of motor engines and vehicle construction, these bio components can be blended with motor fuels in large quantities. Considering the properties of currently used first generation biofuels, the maximum amount of bio-component in engine fuels is approximately 7 (v/v)% fatty acid-methylester in diesel fuels. A reliable production technology of second generation biofuels, which can be blended into diesel fuels is the heterogenic catalytic hydrogenation of triglycerides and waste lards. Furthermore, isomerisation can improve the quality of a bio-paraffin mixture. In this context, we studied the isomerisation of bio-paraffin mixtures, which were obtained from the hydrodeoxygenation of vegetable oil. The characteristics of these products were favourable, such as their cetane number being higher than 75, for example. The actual EN590:2013 standard does not limit the blending ratio of the paraffinic bio-component in diesel fuels. Consequently, these products obtained by the catalytic hydrogenation of vegetable oils can be blended into gasoil by up to 10 % or even more to meet the above EU requirements with respect to the utilisation of renewable fuels.

Keywords: bio gasoil, hydrodeoxygenation, catalytic conversion, biofuels, blending diesel fuels

Introduction

Interest in alternative fuels is on the rise due to the unequal presence of the fossil energy carriers, the periodic rise in the price of fossil fuels, the need for decreasing dependence on crude oil, and the regulations of the European Union. They can play a significant role in achieving the EU plan to reach a 10% energy ratio of total fuel consumption using alternative fuels by 2020. Thus, the application of the biofuels can be increased to a large degree in the long- and medium-terms. For example, in some countries the domestic demand on biofuels could increase to 20% by 2030, along with the decrease in the demand for engine fuels that could be up to 70%. The world's energy production from biomass could reach 5% by 2050 [4, 5]. Accordingly, to ensure the availability of this feedstock the production costs could decrease. To achieve these goals, the EU created several directives (1998/70/EC, 2001/77/EC, 2003/17/EC, 2003/30/EC, 2003/87/EC, 2009/28/CE, and 2009/30/CE). Natural triglycerides like vegetable oils (edible or non-edible/waste) can be feedstock for biofuels as alternative energy sources [6, 7], such as special breeding non-edible oil plants [8, 9], animal fats or waste cooking oil [10, 11]. During the conversion of natural triglyceride molecules to bio-gasoil the following reactions take place [1, 2, 3]:

- full saturation of double bonds (hydrogenation),
- heteroatom removal
  - oxygen removal
    - hydrodeoxygenation (HDO reaction, and reduction)
    - decarboxylation,
    - decarbonylation
  - removing of other heteroatoms (sulphur, nitrogen, phosphorous, and metals),
- isomerisation of *n*-paraffins that are formed during the removal of oxygen
- different side reactions
  - hydrocracking of the fatty acid chain of triglyceride molecules,
  - water-gas shift reaction
  - methanisation,
  - cyclisation, aromatisation, etc.

During the HDO reduction reaction normal paraffins are formed with carbon numbers that are equal to the fatty acids in triglycerides. In the case of decarboxylation and decarbonylation reactions (HDC) normal alkanes are produced, where the carbon number is one less than that of fatty acids of the original vegetable (*Fig.1*).

Bio-gasoil is a mixture of gasoil with the boiling range of *iso*- and *normal*-paraffins. It can be obtained by the hydrogenation of vegetable oils and natural triglycerides

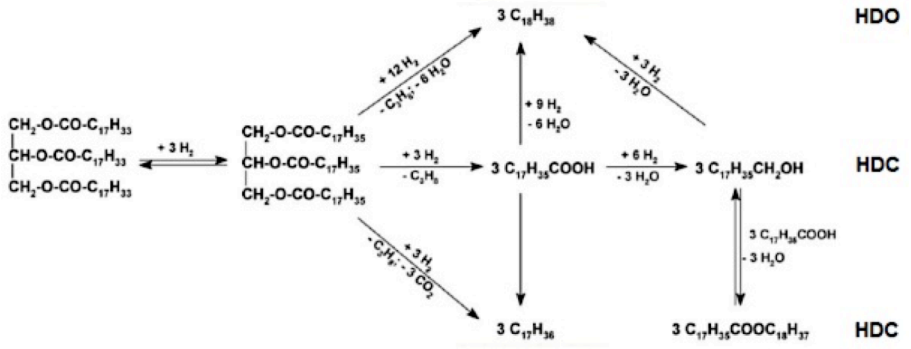

Figure 1: Pathways for the removal of oxygen from vegetable oils

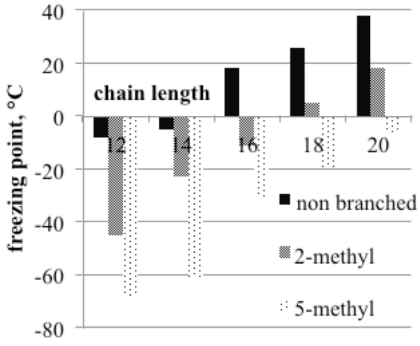

Figure 2: The freezing point of *iso*-paraffins as a function of the branch position

from other sources. These constitute the second generation biofuel components of diesel engines. They have good quality characteristics, such as high cetane number, good flow properties, unlimited mixability with engine fuels, and the a production line compatible with existing refinery structures [18, 19]. The actual EN 590:2013 standard does not limit the blending ratio of second generation bio-components, while the blending of biodiesel is limited to 7 v/v%. All the above mentioned aspects of alternative fuels can rationalise the investigation of the hydrogenation of non-traditional feedstock sources. These are the vegetable oils that can be obtained from non-edible hybrid oil-plants, rapeseed oil from *Brassica napus* with high euric acid content to produce diesel fuel blending components with good flow properties in colder conditions (below +5 °C). The freezing point of *iso*-paraffins from bio-sources is lower than for equal chain length *normal*-paraffins (*Fig.1*) [12-15, 17]. Thus, products with high *iso*-paraffin contents have more favourable cold flow properties (CFPP) with cloud points at lower temperatures (*Fig.2*). The aim of our work was the production of diesel gasoil blending components *via* the isomerisation of paraffin mixtures obtained from the hydrodeoxygenation of rapeseed oil with high euric acid content.

Experimental

In this work, a diesel gasoil bio-blending component production technique was investigated that meets the requirements of the EN:590 Standard with the possibility of blending it with engine fuels in unlimited quantities. Thus, the hydrodeoxygenation of natural triglycerides and further the isomerisation of the obtained bio-paraffin mixture were investigated over the Pt-SAPO-11 catalyst [16] developed in-house. The effect of the operation parameters, such as temperature, pressure, and liquid hourly space velocity (LHSV) was studied on the yield, composition, and utilisation properties of the products.

Experimental Apparatus and Product Separation

The experimental tests were carried out in one of the measured sections of a high-pressure reactor system containing two tubular reactors with a isothermal catalyst volume of 100 cm^3. The reactor system contained all the equipment and devices applied in the reactor system of a hydrotreating plant. The apparatus is suitable for maintaining if not succeeding the industrial precision of main process parameters.

Analytical Methods

The main properties of the feedstock materials and products were determined by standard methods. The hydrocarbon composition of the bio-paraffin mixture was determined by high temperature gas chromatography (Shimadzu 2010 GC [column: Phonomenex Zebron MXT]).

Process Parameters

The ranges of the applied process parameters in the isomerisation test on the basis of our earlier experimental results [13, 14, 17, 20-23] were as follows: temperature 300–360 °C, total pressure 20–80 bar, liquid hourly space velocity (LHSV) 1.0 h^{-1}, and H_2/feed volume ratio of 400 Nm^3 m^{-3}.

Feedstock materials

The feedstock of the catalytic tests was a bio-paraffin mixture, which was obtained from the hydrodeoxygenation of rapeseed with euric acid produced in Hungary. It was properly filtered as a pre-treatment. The main properties of the feedstock material are shown in *Table 1*. The catalyst was Pt-SAPO-11 (0.5 % Pt), the main properties of this can be found in *Table 2*.

Table 1: Selected properties of the feedstock materials

Properties	rapeseed oil		Bio-paraffin mixture	
kinematic viscosity at 40 °C, $mm^2\ s^{-1}$	46.56		3.493	
density at 15 °C, $g\ cm^{-3}$	0.9804		0.7923	
cloud point, °C	16		32	
cetane number	42		104	
compositions, %	Fatty acid		Paraffin	
	C16:0	2.3	C_{14-}	0.2
	C16:1	0.1	C_{14}	0.1
	C18:0	1.2	C_{15}	0
	C18:1	28.8	C_{16}	2.3
	C18:2	12.4	C_{17}	29.5
	C18:3	8.3	C_{18}	28.8
	C20:0	0	C_{19}	6.1
	C20:1	4.8	C_{20}	5.6
	C22:0	0.1	C_{21}	14.8
	C22:1	41.8	C_{22}	12.5
	other	0.2	C_{22+}	0.1

Results and Analysis

The first step was to produce a bio-paraffin mixture with a boiling range of gasoil from rapeseed with a high euric acid content. The properties of the bio-paraffin are summarised in *Table 1*. The commercially available $NiMo/Al_2O_3$ catalyst was utilised for the production of the bio-paraffin mixture. During the catalytic test the employed operation parameters were as follows: 320–380 °C, 20–80 bar, LHSV = 1.0 h^{-1}, and H_2/CH ratio of 600 $Nm^3\ m^{-3}$ [8]. It was found that the favourable operation parameters are 340 °C, 40 bar, LHSV=1.0 h^{-1}, and H_2/CH ratio of 600 $Nm^3\ m^{-3}$. The tested catalyst is suitable for the production of bio-paraffin mixtures with high yields from natural triglycerides. Due to the moderate acidity of this catalyst, the formation of *iso*-paraffins was lower (5 wt%, *Fig.3*). Accordingly, the CFPP of the products was found to be high (27 °C). The product fraction produced in this way, in practice, cannot be blended into diesel fuels in low temperate zone countries. It is necessary then for the improvement of CFPP *via* the catalytic isomerisation of this mixture with high *normal*-paraffin content [10, 11]. A large amount of bio-paraffin mixture was produced in a thousand hour, long-term catalytic test. The target fraction of the isomerisation tests was the 180–360 °C boiling range, which is the boiling range of gasoil. The yield of the target products was higher than 94 % in all operation parameter combinations (*Fig.4*). The lighter fraction with a boiling range of up to 180 ºC contains mainly *iso*-paraffins, which can be outstanding gasoline blending components due to their high octane numbers (>85).

Table 2: Selected properties of the isomerisation catalyst used

Properties	Pt/SAPO-11
Pt content, w%	0.5
Pt dispersity, %	69
BET surface area, $m^2\ g^{-1}$	105
average pore size, nm	0.61
micropore volume, $cm^3\ g^{-1}$	0.06
macropore volume, $cm^3\ g^{-1}$	0.20
total pore volume, $cm^3\ g^{-1}$	0.26
acidity, mmol $NH_3\ g^{-1}$	0.13
acidity (rel.), mmol $NH_3\ m^{-2}$ cat.	0.0012

We found that by adjusting the operation parameters, such as increasing the temperature, and decreasing the LHSV, the yield of the target fraction was decreased due to the higher yield of the cracking reaction. The target fraction obtained between 70% and 80%

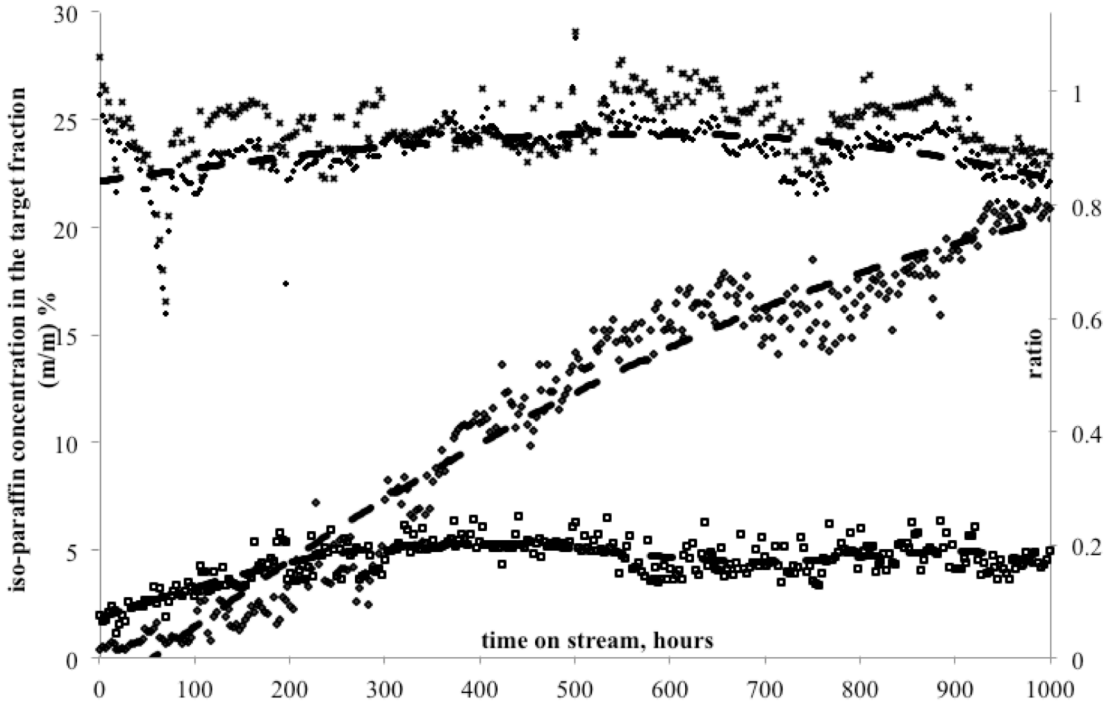

Figure 3: Hydrogenation of rapeseed oil with high euric acid content
(diamond: residual triglyceride, square: *iso*-paraffin content, cross C_{21}/C_{22} ratio)

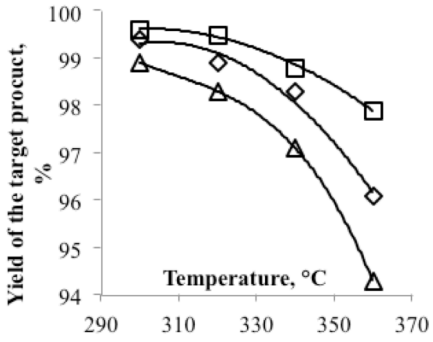

Figure 4: The yield of the target fraction as a function of operation parameters (pressure: 40 bar, liquid hourly space velocity square: 1.0 h^{-1}, diamond 2.0 h^{-1}, triangle 3.0 h^{-1})

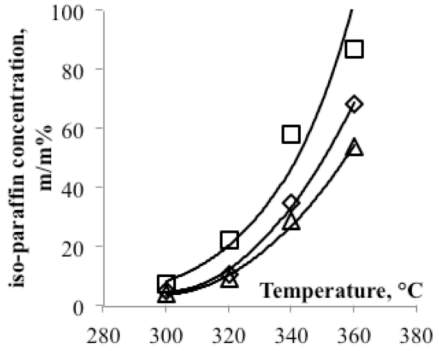

Figure 5: The *iso*-paraffin concentration of the target fraction as a function of operation parameters (pressure: 40 bar, liquid hourly space velocity: square 1.0 h^{-1}, diamond 2.0 h^{-1}, triangle 3.0 h^{-1})

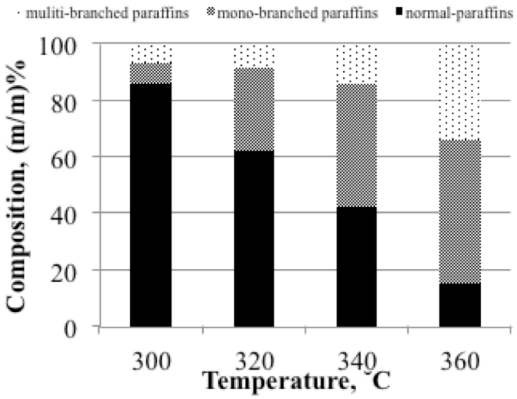

Figure 6: The composition of the products as a function of operation parameters (pressure: 40 bar, liquid hourly space velocity: 1.0 h^{-1})

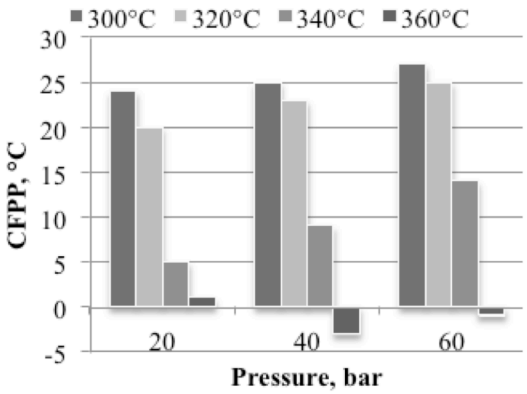

Figure 7: CFFP of the products as a function of operation parameters (liquid hourly space velocity: 1.0 h^{-1}, H_2/feed ratio: 400 Nm^3 m^{-3})

contained C_{17}–C_{22} hydrocarbons, as well as other (C_{13}–C_{16}) hydrocarbons from the boiling range of gasoil. The *iso*-paraffin content of the target fraction increased significantly with the operating temperature (*Fig.5*). The increase of the *iso*-paraffin concentration occurred at 360 °C then at higher temperatures it started to decrease, due to the thermodynamic hindrance of the exothermic reactions, and the higher rate of cracking reactions.

Up to ca. 320 °C, mainly mono-branched *iso*-paraffins were formed and were by in large mono-ethyl-paraffins (*Fig.6*). The freezing points of these products are much lower than *normal*-paraffins and the cetane number is high enough for a fuel additive. The greater formation of mono-methyl-paraffins over the SAPO-11 catalyst can be explained by the reduced formation of *iso*-paraffins due to steric hindrance. At 340 °C or higher, the formation of multi-branched isomers was significant *(Fig.6)*. These compounds have better cold flow properties (below -20 °C), but their cetane numbers are high enough (30–45) as shown in *Fig.2*. The favourable operation parameters in terms of bio-gasoil yield and *iso*-paraffin concentration were as follows: T = 360 °C; p = 40 bar; and H_2/feedstock ratio = 400 Nm^3 m^{-3}. The CFPP values of the products as a function of temperature and operation pressures are shown in *Fig.7*. These components have low enough CFPP values to blend into diesel gasoil in moderate amounts. On the basis of the experimental results, it was concluded that the production of bio-gasoil meets the standard's requirements with a CFPP value of max. +5 °C and 70% *iso*-paraffin content (*Fig.8*) in the case when the raw material contains 8% C_{17}–C_{22} *iso*-paraffins.

Conclusions

Based on our experimental results, it was concluded that the $NiMo/Al_2O_3$ catalyst is suitable for the long-term production of bio-paraffin mixtures from natural triglycerides *via* catalytic hydrodeoxygenation. Furthermore, the investigated Pt-SAPO-11 catalyst is suitable for improving the quality of a bio-paraffin mixture that was obtained from the hydrodeoxygenation of rapeseed oil with high euric acid content. During the isomerisation with optimised operation parameters, the yield of the target fraction was higher than 94%. At 340 °C or higher the *iso*-paraffin content is close to 70%. Consequently, the cold flow property of the cloud point is lower than +5 °C. Therefore, this approach can produce gasoil bio-blending components with good utilisation properties, such as high cetane number, and low temperature values for cold flow properties. Overall, the products described here are suitable for blending components of diesel fuels with concentrations of 10% or higher.

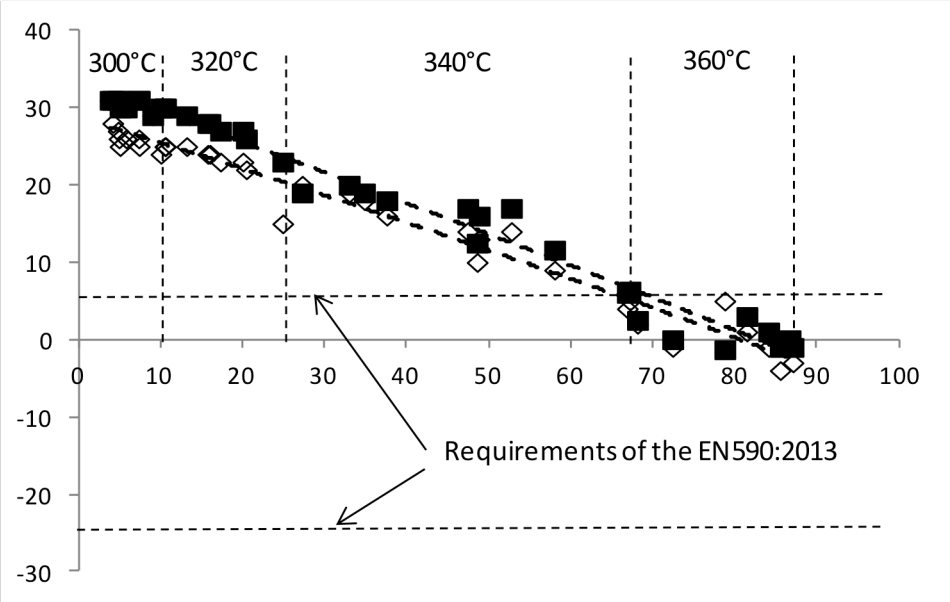

Figure 8: Cold flow properties as a function of *iso*-paraffin concentration
(solid squares: cold filtering clugging point, hollow diamonds: cloud point)

Acknowledgements

We acknowledge the financial support of the Hungarian State and European Union under TÁMOP-4.2.2.A-11/1/KONV-2012-0071 and TÁMOP-4.1.1.C-12/1/KONV-2012-0017.

REFERENCES

[1] HUBER G.W., O'CONNOR P., CORMA A.: Processing biomass in conventional oil refineries: Production of high quality diesel by hydrotreating vegetable oils in heavy vacuum oil mixtures, Appl. Catal. A:General, *2007*, 329,120-129

[2] DA ROCHA FILHO G.N., BRODZKI D., DJEGA-MARIADASSOU G.: Formation of alkanes, alkylcycloalkanes and alkylbenzenes during the catalytic hydrocracking of vegetable oils, Fuel, *1993*, 72(4), 543-549

[3] SIMACEK P., KUBICKA D., SEBOR G., POSPISIL M.: Fuel properties of hydroprocessed rapeseed oil, Fuel, *2010*, 89(3), 611-615

[4] SCHOLLNBERGER W.E.: Between 2020 and 2030 to be re-joined the course for the global energy mix, Erdöl Erdgas Kohle, *2013*, 129(12), 2-7 (in German)

[5] Shell Deutschland Oil Gmbh: Shell study sees great potential for biofuels, Erdöl Erdgas Kohle, *2012*, 128(11), 407-411 (in German)

[6] KRÁR M., KOVÁCS S., KALLÓ D., HANCSÓK J: Fuel purpose hydrotreating of sunflower oil on $CoMo/Al_2O_3$ catalyst, Bioresources Technology, *2010*, 101(23), 9287-9293

[7] KRÁR M., KASZA T., KOVÁCS S., KALLÓ D., HANCSÓK J.: Bio-gasoils with improved low temperature properties, Fuel Proc. Techn., *2011*, 92(5), 886-892

[8] SOLYMOSI P., BALADINCZ P., HANCSÓK J.: Production of motor fuels by the hydrogenation of rapeseed oil with high euric acid content, Proc. 19th EU Biomass Conference and Exhibition, Berlin, Germany, *2011*, 2077-2081

[9] SOLYMOSI P., KASZA T., HANCSÓK J.: Investigation of conventional and high oleic acid content rapeseed or sunflower oils, Hung. J. Ind. Chem., *2011*, 39(1), 85-90

[10] BALADINCZ P., TÓTH CS. HANCSÓK, J.: Expanding feedstock supplies of the second generation biofuels of diesel engines, Hung. J. Ind. Chem., *2010*, 38(1), 1-7

[11] SOLYMOSI P., ELLER Z., HANCSÓK J.: Motor fuel purpose hydrogenation of used cooking oils, Chem. Engng. Trans., *2013*, 35(2), 1351-1356

[12] HANCSÓK J., KASZA T., KOVÁCS S., SOLYMOSI P., HOLLÓ A.: Production of bioparaffins from natural triglycerides, Chem. Engng. Trans., *2011*, 25, 821-826

[13] KASZA T., HANCSÓK J.: Isomerisation of bio-paraffins over Pt-based SAPO-11 and AlMCM-41 catalysts, Műszaki Kémiai Napok, *2011*, 29, 220-225 (in Hungarian).

[14] KASZA T., HOLLÓ A., THERNESZ A., HANCSÓK J.: Production of bio-gasoil from bioparaffins over Pt/SAPO-11, Chem. Engng. Trans., *2010*, 21, 1225-1230

[15] HANCSÓK J., KASZA T., KOVÁCS S., SOLYMOSI P., HOLLÓ A.: Production of bio-gasoil from bioparaffins over Pt/SAPO-11, J. Cleaner Prod., *2012*, 34, 76-81

[16] GERGELY J., FORSTNER J., BALAI M., SZIRMAI L., PETRO J., KOVÁCS I., RESOFSZKI G., SMID L., AUER J., BALADINCZ J., SZALMÁSNÉ PÉCSVÁRI G., TÓTH L., KUBOVICSNÉ STOTZ K., KUN J., KÁNTOR L., CZÁGLER I., LŐVEI J., TÓTH E., LEFKÁNICS GY., TÁTRAI E., PÁLNÉ BORBÉLY G., ROSENBERGNÉ MIHÁLYI M., BEYER H., HANCSÓK J.: A selective hydroisomerisation catalyst preparation and application for hydrocarbons HU 225 912, *2001* (in Hungarian)

[17] KASZA T., KALLÓ D., HANCSÓK J.: Quality improvement of bio-paraffin mixtures, Fuel, *2014*, 120, 1-7

[18] HANCSÓK J., KRÁR M., MAGYAR SZ., BODA L., HOLLÓ A., KALLÓ D.: Investigation of the production of high cetane number biogasoil from pre-hydrogenated vegetable oils over Pt/HZSM-22/Al_2O_3, Micropor. Mesopor. Mat., *2007*, 101(1-2), 148-152

[19] SRIVASTAVA S.P., HANCSOK J.: Fuels and Fuel Additives, Wiley and Sons, Hoboken, NJ, USA, 2014, pp. 121-177

[20] KASZA T., BALADINCZ P., HANCSÓK J.: Production of bio-isoparaffins by the hydroisomerisation of bioparaffins. Hung. J. Ind. Chem., *2009*, 37(2), 95–99

[21] KASZA T., HANCSÓK J.: Production of depressed freezing point bio-gasoil from slaughterhouse waste lard. Hung. J. Ind. Chem., *2010*, 38(1), 41–45.

[22] KASZA T., HANCSÓK J.: Isomerisation of paraffin mixtures produced from sunflower oil. Hung. J. Ind. Chem., *2011*, 39(3), 363–368

[23] KASZA T.; TÓTH CS.; HANCSÓK J.: Application of improved bio-paraffins in diesel fuels, Hung. J. Ind. Chem., *2012*, 40(1), 25–31

HUNGARIAN JOURNAL
OF INDUSTRY AND CHEMISTRY
VESZPRÉM
Vol. 41(2) pp. 115–118 (2013)

THE ENERGY BALANCE OF SEPARATION OPPORTUNITIES IN MICROALGAE TECHNOLOGIES

ZOLTÁN HODAI, ✉ DÓRA RIPPEL-PETHŐ, GÉZA HORVÁTH, LÁSZLÓ HANÁK, AND RÓBERT BOCSI

Department of Chemical Engineering Science, University of Pannonia,
Veszprém, Egyetem u. 10., 8200, HUNGARY
✉Email: hodaiz@almos.uni-pannon.hu

Algae technology is at the focus of international research and development, since it is a green technology that reduces emissions of harmful chemicals and can be considered as a renewable energy source. Carbon dioxide from stack gases and the nitrogen content of wastewater can be considered as food sources for plants and algae. The utilisation of carbon dioxide by algae technologies depends on the technical environment and logistics of teamwork. This technology is a new opportunity in Hungary for decreasing emissions. We grew algae populations to utilise the carbon dioxide from a refinery's stack gas in the continental climate of Hungary. Critical parameters of the technology are the concentration of the algae suspension and extract, because of high investment and operating costs as well as the long operation time, which determines the feasibility of the algae technology. Our specific aim was to separate the algae mass faster and more efficiently from the starting solution. The optimisation of separation operations and technologies took into consideration environmental and economic aspects.

Keywords: microalgae technology, separation, filtration, renewable energy source

Introduction

The utilisation of microalgae carbon dioxide fixation is an important area of international research and development. The absorption of certain technological exhaust gases is possible on the basis of the photosynthesis of microalgae. The absorption of carbon dioxide can reach a magnitude of hundred ton per hectare. C_{16}-C_{22} esters are formed in certain algae cells that can be used for the production of biodiesels. This method is thus capable of producing fuels from renewable sources [1-4].

Algae production is a promising solution amongst the alternative fuel production processes, because it requires of low specific area for growth and high reproduction rate [5-8]. Algae are considered to be one of the most efficient organisms on Earth due to their outstanding reproduction rate, and generally high lipid content. For example, they can double their biomass in 24 hours [9-12]. Their lipid content on average is 20%, but it can be up to 60-80% for certain species [7, 9, 13, 14].

Research into oil production from algae is primarily based on microalgae. These are photosynthesising organisms with a cell size of no greater than 0.5 mm. They can be utilised for carbon dioxide and nitrogen oxide fixation, because they convert these compounds in a photosynthetic energy conversion [15]. The end product of these processes contains a significant amount of solar energy stored as chemical energy.

Furthermore, considerable amounts of biodiesel can be obtained [16-19]. The composition of a microalgae cell depends on cultivation parameters. We tested the available and applicable species under local climatic conditions. Afterwards microalgae that passed the local environmental tests can be considered useable for production.

Research is being carried out into carbon dioxide fixation from technological flows at our institute [15]. The absorption of carbon dioxide and reduction of the release of other pollutants in wastewater using microalgae are being studied. Algae technology utilises waste gases and some environmentally harmful components from wastewaters as nutrients, and thus purifies the growth media. These specific pollutants provide excessive amount of nutrients for the algae, which results in the algae's exponential growth. In addition to the above-mentioned method of energy extraction, a number of research efforts [4, 5, 8, 10-12, 18, 19 25] are currently dealing with the alternative use of biomass produced in this way, and biomass residue that remains after processing. In addition to the above-mentioned advantages, the operating costs can be a limiting factor.

The most critical steps in the production of algae-based biofuels are the harvesting of algae (harvesting, dewatering, and drying), and lipid extraction, because of the high level of investment and operating costs. The main challenge of the technology is to reduce costs, which by in large originate from the separation steps that need to be minimised.

Figure 1: Closed grower systems at the University of Pannonia

Figure 3: Open grower systems at a refinery

Results and Discussions

Our research focuses on carbon dioxide fixation from technological flows. We designed and built various grower systems at the Department of Chemical Engineering of the University of Pannonia (*Fig.1*), as well as at a refinery (*Figs.2* and *3*). By utilising these technological solutions we conducted research into the production of biomass and algae-based products as possible renewable fuels.

The propagation and environmental tolerance parameters were examined along with the possibilities of developing the technology. During the experiments, the whole technological chain was examined providing the possibility to optimise the entire chain of operational steps. The utilisation of algae cultures in experimental photobioreactors is examined, together with the optimisation of the operational conditions both for both artificial and natural light with different substrate solutions. The various parameters for algae processing are also determined.

The foci of our work were the processing and separation operations. Critical points of the technology are the processing steps, such as concentrating the algae suspension and extracting valuable components (lipids). The extraction technologies are of importance because of the high costs of investment and long operation periods. From the literature [5, 10, 12, 15, 17, 22, 23], biodiesel is not yet comparable to fuel produced from petroleum, however the cost of algae technology is dropping. Furthermore, algae technology could become viable if we consider the cost of wastewater purification and flue gas adsorption, and the price of products obtained from microalgae. We need to consider separating possibilities and beyond by analysing gains and losses simultaneously.

Figure 2: Closed grower systems at a refinery

Our specific aim was to devise densification and separation processes, which have low energy requirements and advantageous operation times. Furthermore, we defined useful components from algae and their optimised extraction, based on the optimisation of extraction techniques and other economical and environmental aspects.

Separation Opportunities

Harvesting can be carried out by microfiltration, ultra filtration, centrifugation, flocculation, sonochemical techniques, or some new techniques that are under development [21, 22]. In addition to chemical flocculation, clarification, and membrane separation procedures, special attention was paid to auto flocculation phenomena.

Forms of technology pay more and more attention to convert disposed waste into useful materials. The photosynthesising microorganisms, such as microalgae, utilise solar energy, rapidly reproduce, and do not require any soil to grow in. The biomass product contains solar energy stored in chemical bonds. To process the final product, the suspension, concentration, and extraction of the biomass are the most problematic parts of the methods of algae-based energy production. The main techniques for separation are mechanical operations (filtration, centrifugation, and settling), mechanical operations with admixture (flocculation and defecation), membrane operations (microfiltration and ultrafiltration), and other notable operations (sonochemical techniques, electroflocculation, and flotation). According to examples from the literature [9, 11, 15, 18], there are still only limited generally applicable and proven methods that can be used for biomass production with specific energetic goals.

Energetic Considerations

Increasingly diluted suspensions were examined during separation operations (*Fig.4*). Data from the literature [23-37] need to be brought to a common denominator for carrying out comparisons. For example, our results show that if we want to gradually treat more dilute suspensions using flotation, the energetic considerations can change by orders of magnitude.

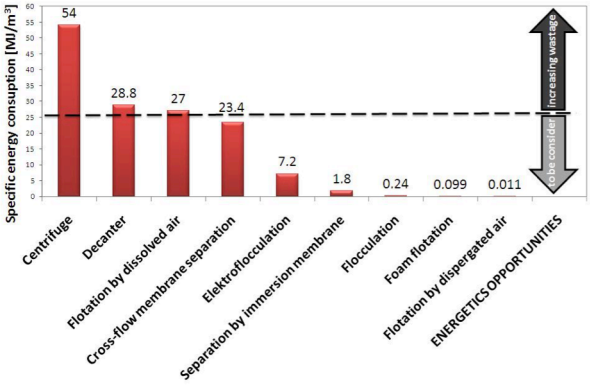

Figure 4: The energetic consideration of selected separation processes (the dashed line shows the energy content of algae suspensions on average of 25 MJ m^{-3})

According to *Fig.4*, cross-flow membrane separation, electroflocculation, centrifugation known as "spiral plate", immersion membrane separation, the flocculation, foam flotation and operation of the flotation by dispersed air are positioned favourably with respect to energetic rating (smaller demand of energy as the energy amount from the separated biomass).

The energy balances of chemical flocculation and electroflocculation do not include the costs of the procurement of chemicals and post-treatment, which would complicate the determination of its energy status. The amounts of chemicals used according to the quality of the suspension were between such wide intervals that they could not be considered using simple factors. By energetic rating, we should note the concentration of the kind of algae suspension in the chosen operation. The increase in volume and decrease in concentration of the suspension may require a review of the cost, materials and energy needs of the separation, and thus change its energetic status. For example, we can conduct a thought-experiment for flotation to see whether the treatment of a dilute suspension needs a device with a different energetic rating. Because of the fixed size of the flotation's device, we cannot decrease the amount of gas flow and the dilute suspension could start to foam, which may make it more difficult to handle than the stability and volume of the foam from a more concentrated suspension. Due to foaming, it will be more difficult for the algae layer to become thicker in the foam unless we use more chemicals and surface-active agents, which result in more parameters to consider. Apart from the above, an important question is how we consider the time domain of the technology (periodic, half-continuous, or continuous). The kind of growing system determines how to connect the separation operation. Half-continuous or continuous (or almost that) operation is beneficial for industrial biomass production to maximise the capacity of biomass. By running the reactor at the maximum rate of reproduction, we can maximise its capacity. According to the latter, the immersion membrane separation operation would be preferable.

Conclusions

According to our investigations, the usable operations for extraction and concentration in algae cultivation with regards to energetic causes vary greatly with respect to energy demands. For dilute suspensions, flotation and foam flotation are the most useful separation processes. We can use flocculation as well, but we have to consider the costs of and environmental damage caused by waste chemicals.

Acknowledgements

This research was supported by the European Union and the State of Hungary, and co-financed by the European Social Fund in the framework of TÁMOP 4.2.4. A/2-11-1-2012-0001 'National Excellence Programme'.

REFERENCES

[1] STRAKA F., DOUCHA J., LÍVANSKY K.: Utilisation of flue gas for cultivation of microalgae (Chlorella sp.) in an outdoor open thin-layer photobioreactor, J. Appl. Phycology, *2005*, 17(5), 403-412

[2] OLAIZOLA M.: Microalgal removal of CO_2 from flue gases: Changes in medium pH and flue gas composition do not appear to affect the photochemical yield of microalgal cultures, Biotechn. Bioproc. Engng., *2003*, 8(6), 360-367

[3] LAMENTI G., PROSPERI G., RITORTO L., SCOLLA G., CAPUANO F., PEDRONI P.M., VALDISERRI M.: Enitecnologie R&D project on microalgae biofixation of CO_2: outdoor comparative tests of biomass productivity using flue gas CO_2 from a NGCC power plant, Proc. 7th Int. Conf. Greenhouse Gas Control Technologies, 2005, 2(1), 1037-1042

[4] CARLSSON A.S., BILEN J.B., MÖLLER R., CLAYTON D.: Mircro- and macroalgae: utility for industrial applications, Ed.: BOWLES D., Outputs from the EPOBIO project. CPL Press, Berks, UK, *2008*

[5] BRIGGS M., VASUDEVAN P.T.: Biodiesel production-current state of the art and challenges, J. Ind. Microbiol. Biotechnol., *2008*, 35, 421-430

[6] HWANG E.J., SHIN H.S., CHAE S.R.: Single cell protein production of *Euglena gracilis* and carbon dioxide fixation in an innovative photobioreactor, Bioresource Technol., *2006*, 97(2), 322-329

[7] BECKER E.W., BADDILEY J.: Microalgae: Biotechnology and Microbiology, Cambridge Univ. Press, New York, USA, *1994*, p. 178

[8] POSEWITZ M.C., JINKERSON R.E., SUBRAMANIAN V.: Improving biofuel production in phototrophic microorganisms with systems biology tools, Biofuels, *2011*, 2(2), 125-144

[9] KOJIMA E., ZHANG K.: Growth and hydrocarbon production of microalgae *Botryococcus braunii* in bubble column photobioreactors, J. Biosci. Bioengng., *1999*, 87(6), 811-815
[10] BRIGGS M.: Wide-scale Biodiesel Production from Algae, Ph.D. Dissertation, University of New Hampshire, *2004*
[11] HWANG E.J., SHIN H.S., CHAE S.R.: Single cell protein production of *Euglena gracilis* and carbon dioxide fixation in an innovative photobioreactor Bioresource Technol., *2006*, 97(2), 322-331
[12] CHISTI Y.: Biodiesel from microalgae, Biotechnol. Adv., *2007*, 25(3) 294–306
[13] DISMUKES G.C.: Algal Photosynthesis, Princeton University Press, Princeton, NJ, USA *2008*
[14] SHI D., SONG D., FU J.: Construction of a shuttle vector for heterologous gene expression in *Escherichia coli* and microalgae anabaena, Chin. J. Biotechnol., *2008*, 24(3), 341-348
[15] BOCSI R., HORVÁTH G., HANÁK L.,: Microalgae production in service of fuel production, Hung. J. Ind. Chem., *2010*, 38(1), 9-13
[16] OLAIZOLA M., MASUTANI S.M., NAKAMURA T.: Recovery and sequestration of CO_2 from stationary combustion systems by photosynthesis of microalgae, U.S. Department of Energy, Office of Fossil Energy National Energy Technology Laboratory, Pittsburgh, PA, USA, *2006*
[17] BENEMANN J., SHEEHAN J., ROESSLER P., DUNAHAY T.: Biodiesel from algae, a look back at the U.S. DOE's aquatic species program, NREL Report NREL/TP-580-24190, *1998*
[18] BURLEW J.: Algae culture: from laboratory to pilot plant, Carnegie Institute, Washington DC, USA *1953*
[19] JUNG I.H., CHOE S.H.: Growth inhibition of freshwater algae by ester compounds released from rotten plants, J. Ind. Engng. Chem., *2002*, 8(4), 297-304
[20] SHELEF G.A., SUKENIK A., GREEN M.: Microalgae harvesting and processing: a literature review, Techn. Rep., Solar Energy Research Institute, *1984*
[21] POELMAN E., PAUW N.D., JEURISSEN B.: Potential of electrolytic flocculation for the recovery of micro-algae, Res. Conserv. Recyc., *1997*, 19(1), 1-10
[22] LEITE G.B., ABDELAZIZ A.E.M., HALLENBECK P.C.: Algal biofuels: challenges and opportunities, Bioresource Technol., *2013*, 145, 134-141
[23] RAWAT I., RANJITH KUMAR R., MUTANDA T., BUX F.: Biodiesel from microalgae: A critical evaluation from laboratory to large-scale production, Appl. Energy, *2013*, 103, 444-467
[24] DASSEY A.J., THEEGALA C.S.: Harvesting economics and strategies using centrifugation for cost-effective separation of microalgae cells for biodiesel applications, Bioresource Technol., *2013*, 128(2), 241-245
[25] UDOM I., ZARIBAF B.H., HALFHIDE T., GILLIE B., DALRYMPLE O., ZHANG Q., ERGAS S.J.: Harvesting microalgae grown on waste water, Bioresource Technol., *2013*, 150, 513-522
[26] UDUMAN N., BOURNIQUEL V., DANQUAH M.K., HOADLEY A.F.A.: A parametric study of electrocoagulation as a recovery process of marine microalgae for biodiesel production, Chem. Eng. J., *2011*, 174(1), 249-257
[27] BEACH E.S., ECKELMAN M.J., CUI Z., BRENTNER L., ZIMMERMAN J.B.: Preferential technological and life cycle environmental performance of chitosan flocculation for harvesting of the green algae *Neochloris oleoabundans*, Bioresour. Technol., *2012*, 121, 445–449
[28] BANERJEE C., GHOSH S., SEN G., MISHRA S., SHUKLA P., BANDOPADHYAY R.: Study of algal biomass harvesting using cationic guar gum from the natural plant source as flocculent, Carbohydrate Polymers, *2013*, 92(1), 675-681
[29] SCHLESINGER A., EISENSTADT D., BAR-GIL A., CARMELY H., EINBINDER S., GRESSEL J.: Inexpensive non-toxic flocculation of microalgae contradicts theories; overcoming a major hurdle of bulk algal production. Biotechnol. Adv., *2012*, 30(5), 1023–1030
[30] JUNGMIN K., BYUNG-GON R., KYOCHAN K., BO-KYONG K., JONG-IN H., JI-WON Y.: Continuous microalgae recovery using electrolysis: Effect of different electrode pairs and timing of polarity exchange, Bioresource Technol., *2012*, 123(2), 164-170
[31] MASCIA M., VACCA A., PALMAS S.: Electrochemical treatment as a pre-oxidative step for algae removal using Chlorella vulgaris as a model organism and BDD anodes, Chem. Enging. J., *2013*, 219(5), 512-519
[32] LEE A.K., LEWIS D.M., ASHMAN P.J.: Harvesting of marine microalgae by electroflocculation: The energetics, plant design, and economics, Appl. Energy, 2013, 108(3), 45-53
[33] AMER L., ADHIKARI B., PELLEGRINO J.: Techno-economic analysis of five microalgae-to-biofuels processes of varying complexity, Bioresource Technol., *2011*, 102(20), 9350–9359
[34] EDZWALD J.K.: Algae, bubbles, coagulants, and dissolved air flotation, Water Sci. Technol., *1993*, 27(10), 67–81
[35] NURDOGAN Y., OSWALD W.J.: Tube settling of high-rate pond algae, Water Sci. Technol., *1996*, 33(7), 229–241
[36] COLLET P., HÉLIAS A., LARDON L., RAS M., GOY R.A., STEYER J.P.: Life-cycle assessment of a microalgae culture coupled to biogas production, Bioresoure Technol., *2011*, 102(1), 207–214
[37] COWARDA T., LEEA J.G., CALDWELLB G.S.: Development of a foam flotation system for harvesting microalgae biomass, Algal Research *2013*, 2(2), 135-144

HUNGARIAN JOURNAL
OF INDUSTRY AND CHEMISTRY
VESZPRÉM
Vol. 41(2) pp. 119–122 (2013)

SOLID-LIQUID EXTRACTION OF CHLOROPHYLL FROM MICROALGAE FROM PHOTOAUTOTROPH OPEN-AIR CULTIVATION

ÉVA MOLNÁR, ✉ DÓRA RIPPEL-PETHŐ, AND RÓBERT BOCSI

Department of Chemical Engineering, Institute of Chemical and Process Engineering, University of Pannonia,
Egyetem u. 10., Veszprém, 8200, HUNGARY
✉Email: molnare@almos.uni-pannon.hu

Among industrial pollutants, strict quotas limit the emission of carbon dioxide in the European Union. The capturing and deposition of carbon dioxide requires significant expenditures. One of the newer solutions for the reduction of the carbon dioxide emissions is provided by algae technology. In this technology, the absorption of carbon dioxide is achieved by photosynthesis. Besides the reduction of pollutants, algae technology has another advantage by supplying valuable products, such as natural pigments, proteins, vitamins and oils from algae biomass. Since it has a high reproduction rate, algae cultivation can be a feasible substitute for plants traditionally used in the production of chlorophyll. The viability of the technology is dependent on whether or not the processing can be done economically. An investigation was carried out in order to compare and contrast two extraction methods (Soxhlet extraction and leaching) and four solvents (acetone, diethyl ether, ethanol and methanol) to determine the most effective method for the extraction of chlorophylls from dried microalgae (*Chlorella vulgaris sp.*). It was concluded that methanol is the most effective solvent for the extraction of both chlorophylls *a* and *b* using both Soxhlet extraction and leaching.

Keywords: microalgae, extraction solvent, extraction, chlorophyll, spectrophotometry

Introduction

Energy demand has been rapidly increasing throughout the world, which is mainly met by the combustion of fossil fuels that results in an increase in the concentration of greenhouse gases in the atmosphere. However as a possible remediation strategy, carbon dioxide levels can be reduced with the use of algae technology [1]. Algae technology is of significant interest in research and development since it is a 'green' technology that is capable of both decreasing the emission of pollutants and serving as a renewable energy source. The algae absorb carbon dioxide for photosynthesis while producing a number of valuable components [2]. Microalgae are a collection of various microscopic species capable of photosynthesis and are typically found in water with an exceptionally high reproduction rate. For propagation, they mainly need light, water and CO_2. Some species can even survive in waste water. Algae are good alternatives for plants that are traditionally used for the production of chlorophyll. Appropriate conditions are required for the successful cultivation of algae (solar energy, temperature, pH, and mixing) [3, 4]. However, the critical point of algae technology is neither cultivation nor processing. The biggest complication concerns the concentration of the microalgae suspension and the subsequent extraction of the valuable components due to the high investment costs and long operational times [5]. There is, however, an increasing demand for microalgae. The reason for this is that their oil content can be as much as 50% of their body mass, making them important in the production of biodiesel. The natural pigments, proteins and vitamins extracted from microalgae are primarily used by the pharmaceutical, cosmetic and food industries [3, 6].

Chlorophyll has been used for centuries as a traditional remedy for unpleasant body odours, for the neutralisation of the odours of stool and urine, and detoxification or sterilisation of wounds. Nowadays, its use is even more widespread. It is used as a food additive, food colouring, and nutritional supplement, especially because of its detoxifying and excellent basifying effects. It is also a strong antioxidant, which inhibits the harmful oxidative processes in the body and enhances the protection of cells and tissues [7, 8]. However, the processing of algae still needs to be improved with respect to determining the optimal methods, pieces of equipment, solvents, and parameters for the efficient and economic extraction of chlorophyll. Extraction is a process that can be carried out in a number of ways. There are also a number of solvents and preparation methods available. Also, variables such as pressure, temperature, the efficiency of contact and time all play an important role [9, 10]. Chlorophyll is sensitive to extreme light exposure, pH values and temperatures [7-9]. When choosing the solvent, one has to consider the sensitivity of the extracted component. A number of considerations are important, too: density, viscosity, heat of evaporation, price, effect on the environment and health. It is also essential that the

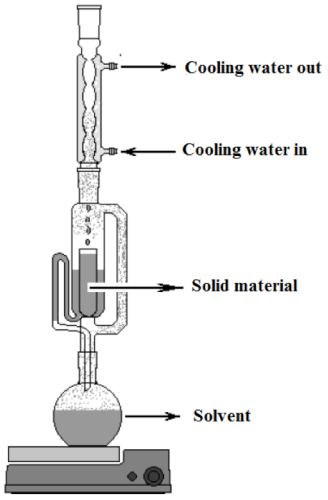

Figure 1: Soxhlet extractor [12]

solvent does not react with or cause damage to the extracted component and is not corrosive. Different methods can be used for different microalgae species [9-10].

Experimental

In advance of the extraction experiments the algae suspension (*Chlorella vulgaris sp.*) was concentrated, dried at 60 ºC until it reached a constant mass, then ground in a ball mill. Chlorophylls *a* and *b* products were obtained by the methods detailed in the following sections from this ground algae powder, which contains approximately 4 wt% water.

The Soxhlet Extraction Method

One of the most well known pieces of equipment for laboratory scale solid-liquid extraction is the Soxhlet extractor. In a Soxhlet extractor multiple fractional distillations are carried out, the extraction is always done with the pure condensate [10].

The first step of the extraction was to fill a cellulose casing with 1-3 g of algae powder. The filled casing was placed in the middle part of the piece of equipment (*Fig.1*). The lower round-bottom flask was filled with 400 cm^3 of solvent. The Soxhlet extraction was carried out with methanol, ethanol, and acetone. Pumice and a magnetic stirring rod were placed into the lower flask to ensure proper boiling. The cooling water was set to a continuous flow and then the heating was turned on. After the extracting solvents had reached their boiling points and started to evaporate, they condensed in the reflux condenser and dripped back down onto the algae powder at which point the extraction of the chlorophylls started. The liquid level continuously rose in the middle section until it reached the overflow pipe letting the chlorophyll extract pour back into the lower flask. A sample of 4–6 cm^3 was taken at the end of every cycle. The extraction continued as long as the absorption spectra measured by the spectrophotometer did not show a significant change.

The Method of Leaching

Leaching was carried out with so-called 'cold solvents' at room temperature. Samples of 0.1 g; 0.5 g; and 0.75 g of algae powder were measured into a test tube, then 5–5 cm^3 of solvent was added. The list of solvents was the same as for the Soxhlet extraction method with the inclusion of diethyl ether. The weight of the solvent was also measured and recorded in order to have reference data in the later phases of the experiment. The samples were mixed with Vortex and centrifuged for 2 minutes at 4000 rpm. A sample was taken from the top layer after centrifuge and its absorbance measured with a spectrophotometer [11, 12].

Calculations

The chlorophyll contents of the given samples were calculated with empirical formulae according to *Eqs.(1)-(8)*.

$$c_{\text{chlorophyll-a}}(90\%\ \text{methanol}) = 15.65 \cdot A_{666} - 7.34 \cdot A_{653} \quad (1)$$

$$c_{\text{chlorophyll-b}}(90\%\ \text{methanol}) = 27.05 \cdot A_{653} - 11.21 \cdot A_{665} \quad (2)$$

$$c_{\text{chlorophyll-a}}(96\%\ \text{ethanol}) = 13.95 \cdot A_{665} - 6.88 \cdot A_{649} \quad (3)$$

$$c_{\text{chlorophyll-b}}(96\%\ \text{ethanol}) = 24.96 \cdot A_{649} - 7.32 \cdot A_{665} \quad (4)$$

$$c_{\text{chlorophyll-a}}(100\%\ \text{acetone}) = 11.75 \cdot A_{662} - 2.35 \cdot A_{645} \quad (5)$$

$$c_{\text{chlorophyll-b}}(100\%\ \text{acetone}) = 18.61 \cdot A_{645} - 3.96 \cdot A_{662} \quad (6)$$

$$c_{\text{chlorophyll-a}}(95\%\ \text{diethyl ether}) = 10.05 \cdot A_{662} - 0.76 \cdot A_{644} \quad (7)$$

$$c_{\text{chlorophyll-b}}(95\%\ \text{diethyl ether}) = 16.37 \cdot A_{644} - 3.14 \cdot A_{662} \quad (8)$$

where A_λ is the absorbance at λ (in nm) wavelength, and $c_{\text{chlorophyll-a}}$ and $c_{\text{chlorophyll-b}}$ denote concentrations of chlorophyll *a* and chlorophyll *b* in μg cm^{-3} [12] as a function of solvents.

In Soxhlet extraction, the mass of the chlorophyll in the extract was calculated by the multiplication of the measured chlorophyll concentration values by the volume of the liquid in the round bottom flask. This also enabled the calculation of efficiency in mg of chlorophyll per g of dry algae units (relative to 100% dry algae powder).

In the leaching experiments, the chlorophyll concentration results calculated with the empirical formulae were multiplied by the volume of the solvent that resulted in the relative chlorophyll mass values in the given samples. Knowing the mass and water content of the algae, the efficiency of chlorophyll extraction relative to the mass of the dry algae can be calculated. These results were normalised to match the measurements and average values were calculated.

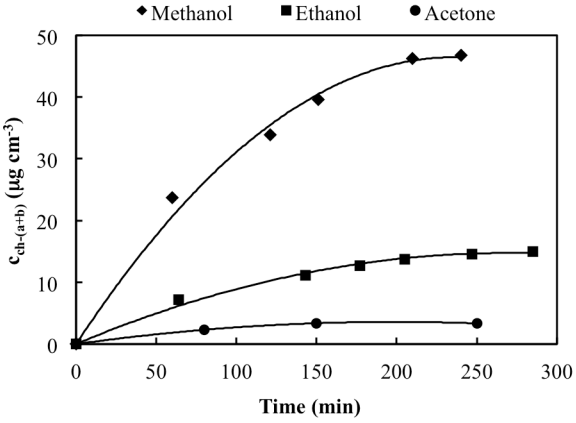

Figure 2: Changes in chlorophyll concentration during the Soxhlet measurements

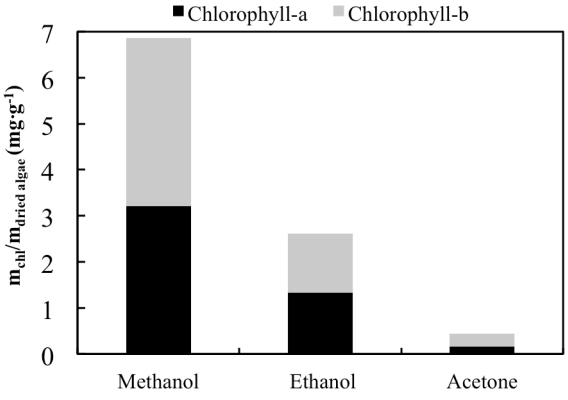

Figure 3: The efficiency of chlorophyll extraction of the various solvents during Soxhlet extraction

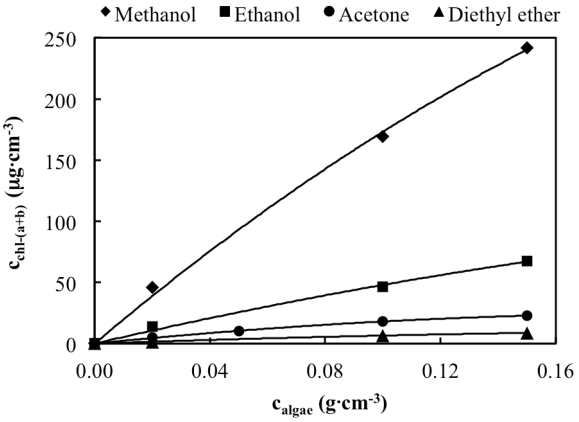

Figure 4: Change in chlorophyll concentration as a function of mass during leaching

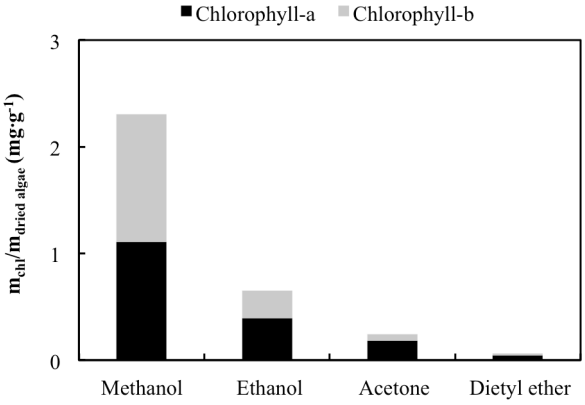

Figure 5: Efficiency of leaching using the various solvents

Results and Discussion

Soxhlet Extraction

The chlorophyll concentration measured changed according to a saturation curve as shown in *Fig.2*. It can be concluded that under the given circumstances the solvents reached their maximum efficiency and there was no need for longer extraction times. The ability of the solvents to extract chlorophyll relative to dried algae mass during the Soxhlet extraction is given in *Fig.3*.

The experiments were carried out using acetone, ethanol and methanol. It can be concluded that under the conditions of Soxhlet extraction, methanol is the most potent extracting solvent of chlorophyll *a* and *b* from the algae powder, followed by ethanol and acetone respectively. It can also be pointed out that acetone and methanol are more effective for the extraction of chlorophyll *b* while ethanol is more effective for the extraction of chlorophyll *a*. The latter experiment was not carried out with diethyl ether due to health and safety considerations.

Extraction by Leaching

Figs.4 and *5* illustrate the results of leaching. *Fig.4* depicts the concentration of chlorophyll for different masses of algae powder introduced into the system. The curves approach a saturation point in concentration, but do not reach the maximum. When we added progressively more and more algae powder to the same volume of solvent we observed increasing saturation behaviour. *Fig.5* presents the chlorophyll extracting ability of the various solvents when mixing 0.1 g of algae powder and 5 cm^3 of solvent. As expected, the best result was obtained by utilising at least 0.1 g of algae powder of. The efficiency ranking was similar to that of the Soxhlet extraction. Methanol proved to be the most efficient solvent, followed by ethanol, acetone and diethyl ether respectively.

The results are summarised in *Table 1,* which contains mg of chlorophyll per g of dry algae yields. This comparison enables the different solvents to be ranked and extraction methods, which is as follows according to their efficiency: methanol, ethanol, acetone, and diethyl ether. Additionally, significantly more chlorophyll can be extracted from ground algae with Soxhlet extraction than with leaching. In the

Table 1: Comparison of the chlorophyll (Chl.) extraction results

	Soxhlet extraction			Leaching		
	Chl. *a*	Chl. *b*	Chl. *a* & *b*	Chl. *a*	Chl. *b*	Chl. *a* & *b*
acetone	0.164	0.270	0.435	0.183	0.059	0.242
ethanol	1.329	1.290	2.619	0.395	0.259	0.654
methanol	3.206	3.657	6.862	1.109	1.199	2.307
diethyl ether	n/a	n/a	n/a	0.044	0.017	0.062

experiments conducted with acetone, it was observed that the extraction efficiency of chlorophyll *a* or chlorophyll *b* is greatly dependent on the conditions. Methanol, the solvent that proved to be the most efficient, could be removed later from the chlorophyll by low temperature evaporation.

Conclusions

From a systematic investigation of solid-phase extraction of chlorophyll *a* and chlorophyll *b* using Soxhlet extraction and leaching as a function of the employed solvent, it was found that the most efficient solvent is methanol. In both extraction techniques, the extracted amount of chlorophyll using methanol as a solvent is approximately an order of magnitude higher than in acetone and close to three to four times greater than the results of ethanol.

REFERENCES

[1] BOROWITZKA M.A.: Energy from Microalgae: A Short History, Develop. Appl. Phycology (Springer, The Netherlands), *2013*, 5, 1-15

[2] NAJAFI G., GHOBADIAN B., YUSAF T.F.: Algae as a sustainable energy source for biofuel production in Iran: A case study, Renewable and Sustainable Energy Reviews, *2011*, 15 (8), 3870–3876

[3] MATA T.M., MARTINS A.A., CAETANO N.S.: Microalgae for biodiesel production and other applications: A review, Renewable and Sustainable Energy Reviews, *2010*, 14(1), 217–232

[4] BOCSI R., HORVATH G., HANAK L., HODAI Z.: Extraction examinations of microalgae propagated for biodiesel additives, Hung. J. Ind. Chem., *2011*, 39(1), 45-49

[5] FAIZAL B.: Biotechnological applications of microalgae: biodiesel and value-added products, CRC Press, Bosa Roca, FL, United States, *2013*, pp. 80

[6] DEMIRBAS A., DEMIRBAS M.F.: The importance of algae oil as a source of biodiesel, Energy Conversion and Management, *2011*, 52(1), 163-170

[7] LANFER-MARQUEZ U.M., BARROS R.M.C., SINNECKER P.: Antioxidant activity of chlorophylls and their derivatives, Food Res. Int., *2005*, 38(8-9), 885–891

[8] HOSIKIAN A., LIM S., HALIM R., DANQUAH M.K.: Chlorophyll extraction from microalgae: A review of the process engineering aspects, Int. J. Chem. Engng., *2010*, Article ID 391632

[9] SIMPSON N.J.K., WELLS M.J.M.: Introduction to Solid-Phase Extraction, Marcel Dekker Inc, New York, NY, USA, *2000*, pp. 1-18

[10] MEIRELES M.A.A.: Extracting Bioactive Compounds for Food Products, Theory and Applications Contemporary Food Engineering Series, CRC Press, Dublin, Ireland *2009*, pp. 140-159

[11] LAN S., WU L., ZHANG D., HU C., LIU Y.: Ethanol outperforms multiple solvents in the extraction of chlorophyll-a from biological soil crusts, Soil Biology and Biochemistry, *2011*, 43(4), 857–861

[12] WELLBURN A.R., LICHTENTHALER H.: Formulae and program to determine total carotenoids and chlorophylls-a and b of leaf extracts in different solvents, Adv. Agricul. Biotechn., *1984*, 2(1), 9-12

HUNGARIAN JOURNAL
OF INDUSTRY AND CHEMISTRY
VESZPRÉM
Vol. 41(2) pp. 123–130 (2013)

CALCULATING THE ELECTROSTATIC POTENTIAL PROFILES OF DOUBLE LAYERS FROM SIMULATION ION DENSITY PROFILES

DEZSŐ BODA,[✉1] AND DIRK GILLESPIE[2]

[1]Department of Physical Chemistry, University of Pannonia, Egyetem u. 10., Veszprém, 8200, HUNGARY
[2]Department of Molecular Biophysics and Physiology, Rush University Medical Center, 1750 W. Harrison St., Chicago, USA
[✉]E-mail: boda@almos.vein.hu

Computer simulations of the planar double layer geometry provide the charge profile with statistical noise. To compute the mean electrostatic potential profile from the charge profile, one must solve Poisson's equation with appropriate boundary conditions (BC). In this work, we show that it is advantageous to use the Neumann or Dirichlet BCs at the boundaries of the simulation domain with an integrated version of Poisson's equation. This minimises errors from the simulation's noisy density profiles, in contrast to traditional convolution integrals that amplify the noise. The Neumann BC, where the electric field is prescribed, can be used in both the constant surface charge and constant electrode voltage ensembles. In the constant voltage ensemble, where the potential difference between the confining electrodes is prescribed, one can also use the Dirichlet BC, where the potentials at the boundaries are set. We show that the new methods provide converged results for the potential profile faster than the convolution integral does.

Keywords: electrical double layer, Poisson equation, boundary conditions, computer simulation

Introduction

The electrical double layer (DL) is formed by a charged surface and a phase (usually, a liquid) containing mobile charge carriers near the surface. Depending on the material carrying the mobile charges, DLs appear in electrolytes, molten salts, ionic liquids, plasmas, and even fast ion conductors (solid electrolytes). DLs in solutions of dissolved ions are particularly important in electrochemistry, biology, and colloid chemistry. DLs near electrodes differ from DLs near charged objects carrying a fixed surface charge (such as colloids, macromolecules, and porous bodies), because the surface charge on the electrode can be controlled by an external voltage.

Theoretical studies of DLs began with the Poisson-Boltzmann (PB) theory known as the Gouy-Chapman (GC) theory [1, 2] in electrochemistry, the Debye-Hückel (DH) theory [3] in solution chemistry, and the Derjaguin-Landau-Verwey-Overbeek (DLVO) theory [4, 5] in colloid chemistry. The PB theory is still very popular in applications because of its simplicity in spite of the fact that it neglects ionic correlations and effects due to the finite size of ions (e.g., excluded volume). More powerful statistical mechanical theories that are able to take these correlations into account have been developed [6–16]. Computer simulations are a versatile method of studying DLs in various geometries for various models of the constituents (ions, water, and electrode) [17–35]. This paper focuses on computing the electrical field and potential from a charge distribution obtained from computer simulations.

Computer simulations of systems containing charged particles must be performed in accordance with the laws of both electrostatics and statistical mechanics [36, 37]. This means that the electrical potential must be computed accurately for every configuration sampled in a Monte Carlo (MC) simulation. Alternatively, the electrical field must be computed accurately in every time step of a molecular dynamics (MD) simulation. Every configuration of the system (positions of ions) corresponds to a microscopic state. In this case, we consider the system at the microscopic level. A simulation that samples the possible microscopic states must be performed properly according to the probability distribution of a given statistical mechanical ensemble. One typical simulation method to handle various ensembles is MC. The density distribution of ionic species i, $\langle\rho_i(\mathbf{r})\rangle$, is obtained as an ensemble average from the simulation. From these, the average charge distribution can be obtained as

$$q(\mathbf{r}) = \langle Q(\mathbf{r})\rangle = \sum_i z_i e \langle\rho_i(\mathbf{r})\rangle , \qquad (1)$$

where $Q(\mathbf{r})$ is the charge distribution in a microscopic state, e is the electronic unit charge and z_i is the valence of ionic species i.

The average (mean) electrostatic potential can be obtained "on the fly" by computing the potential in the simulation cell for every configuration (denoted by $\Psi(\mathbf{r})$) and then taking the ensemble average, $\psi(\mathbf{r}) = \langle\Psi(\mathbf{r})\rangle$. In this work, we use upper-case symbols for the microscopic quantities ($\Psi(\mathbf{r})$ and $Q(\mathbf{r})$), while we use lower-case symbols for their macroscopic counterparts, namely,

their ensemble averages ($\psi(\mathbf{r})$ and $q(\mathbf{r})$). The electrical potential in a configuration of the MC simulation, $\Psi(\mathbf{r})$, can be computed analytically from Coulomb's law or numerically using a Poisson solver. In both cases, we apply electrostatic BCs at the microscopic level.

The reverse order, when we compute the ensemble average of the charge distribution *(Eq.(1))* and then solve Poisson's equation for the mean potential

$$\nabla^2\psi(\mathbf{r}) = -\frac{1}{\epsilon_0}q(\mathbf{r}) \tag{2}$$

is more usual (ϵ_0 is the permittivity of vacuum). This equation applies to either explicit or implicit solvent models. In the explicit solvent framework, $q(\mathbf{r})$ also contains the charge distribution of the water molecules (in addition to their ionic charges). In the implicit solvent framework, where water is represented by a dielectric background characterised by a dielectric constant, ϵ, $q(\mathbf{r})$ also contains polarisation charges induced in the dielectric (in the simplest case, $q(\mathbf{r})$ is the ionic charges divided by ϵ). Because we are solving a differential equation, we must use appropriate boundary conditions (BCs) when solving *Eq.(2)*. Because we want an ensemble averaged result, we apply the BCs at the macroscopic level.

This paper describes how to numerically integrate the Poisson equation with appropriate BCs to efficiently compute the mean electrostatic potential profile from the mean charge profile obtained from simulations. The statistical ensemble applied in the simulation determines which BC to use. In this paper, we consider the two basic ensembles, one where the electrode charges are fixed (constant charge ensemble) and one where the difference between the electrode potentials is fixed (constant voltage ensemble).

In the constant charge ensemble, the traditional method of computing the potential profile is via a convolution integral. Here, we show that this method is error-prone and numerically inefficient and instead, it is more advantageous to use a different integration scheme with Neumann BCs, where the normal electric fields at the boundaries of the system are fixed [38].

In the constant voltage ensemble developed by KIYOHARA and ASAKA [39], the electrode potentials are known in advance. Therefore, we can also use Dirichlet BCs, where the potentials at the boundaries of the system are prescribed.

In the following, we describe our model in detail. Then, we consider all three issues discussed above (BCs at the microscopic level, statistical mechanical ensembles, and BCs at the macroscopic level) and present various possibilities for the macroscopic BC depending on the statistical mechanical ensemble used. We present results of model calculations to show the self-consistency of these calculations.

Model and Boundary Condition at the Microscopic Level

At the microscopic level, we have a system that contains localised discrete and/or continuous distributions of charges $Q(\mathbf{r})$. In practice, there are two traditional schools to compute the electrostatic energy (in MC) or forces (in MD) for a configuration sampled by a computer simulation. In one school, the potential is computed on a grid from Poisson's equation *(Eq.(2))* using a partial differential equation (PDE) solver with appropriate boundary conditions. This method is generally used in MD simulations of explicit solvent systems.

In the other school, Coulomb's law is used to calculate the potential:

$$\Psi(\mathbf{r}) = \frac{1}{4\pi\epsilon_0\epsilon}\int Q(\mathbf{r}')G(\mathbf{r},\mathbf{r}')d\mathbf{r}', \tag{3}$$

where $G(\mathbf{r},\mathbf{r}')$ is the appropriate Green's function. This method is generally used for simulations with implicit solvents.

The planar DL geometry means that we have a rectangular simulation cell of length $L_2 - L_1$ and with a base $H \times H$ confined by two planar electrodes at the two ends ($x = L_1$ and $x = L_2$) carrying surface charges σ_1 and σ_2. Periodic boundary conditions (PBC) are used in the y, and z dimensions, which means that the Green's function is

$$G(\mathbf{r},\mathbf{r}') = \sum_{j=-\infty}^{\infty}\sum_{k=-\infty}^{\infty}\frac{1}{|\mathbf{r}-\mathbf{r}'+jH\mathbf{n}_y+kH\mathbf{n}_z|} \tag{4}$$

where the sum over j and k represents the interaction with the periodic image charges in the replicas of the central simulation cell in the y and z dimensions set by the unit vectors $\mathbf{n}_y$ and $\mathbf{n}_z$. The term $j = k = 0$ corresponds to the interaction with the charge in the central simulation cell computed explicitly. In this paper, the interaction with periodic replicas is taken into account using the charged sheet method by smearing these charges into a sheet carrying q/H^2 surface charges with a H^2 square hole in the middle. The interaction with the holed sheet can be integrated. For further details, see Ref. [18, 29].

The statistical mechanical ensemble determines which thermodynamic variables are fixed in the simulation. The attempts in the MC simulations are designed to ensure sampling according to the probability distribution of the given ensemble. Moreover, the simulation must be self-consistent in the sense that a prescribed thermodynamic variable must agree with its value computed as an output of the simulation. For example, in an NpT simulation (where the pressure is fixed), the pressure can also be computed from the virial sum as an ensemble average in both NVT and NpT simulations. This value must be equal to the one prescribed in the NpT ensemble. In practice, however, the accuracy of the pressure computed from the virial sum depends on the size of the system, and one obtains the same relationship between pressure

and density from NVT and NpT simulations only in the limit of very large simulation cells.

From the point of view of the DL problem, the question is whether we perform the simulation in the constant charge or constant voltage ensemble. In the constant charge ensemble the surface charges on the confining walls of the simulation cell are fixed. This is the traditional simulation setup used in DL simulations since TORRIE and VALLEAU [17, 18]. The output of the simulation is the density profiles of the various ionic species $\langle \rho_i(x) \rangle$ (the PBC applied in the y and z dimensions ensures that the profiles depend on x only), from which the x-dependent charge profile, $q(x)$, is obtained (see *Eq.(1)*). The corresponding form of Poisson's equation is

$$\frac{d^2\psi(x)}{dx^2} = -\frac{1}{\epsilon_0 \epsilon} q(x), \tag{5}$$

where ϵ is now included so $q(x)$ constrains only ionic and electrode charges.

Recently, KIYOHARA and ASAKA [39] introduced the constant voltage ensemble, where the potential difference between the two confining walls (the electrodes) is prescribed. A special MC step, where a small amount of charge, $\Delta\sigma$, is transferred from one electrode to the other, has been introduced. The charge exchange is accepted on the basis of the Boltzmann factor

$$\min\left[1, \exp\left(-\frac{\Delta U}{kT} + \frac{H^2 \Delta\psi^* \Delta\sigma}{kT}\right)\right] \tag{6}$$

where ΔU is the energy change associated with the charge movement and $\Delta\psi^* = \psi(L_2) - \psi(L_2)$ is the prescribed voltage. Here, the surface charges on the electrodes fluctuate, while the potential difference between the electrodes ($\Delta\psi^*$) is an independent, prescribed variable of the ensemble. The mean potential profile can be computed from *Eq.(5)*. The computed voltage, namely, the potential difference between the electrodes, $\Delta\psi = \psi(L_2) - \psi(L_2)$, must be equal to the prescribed voltage, $\Delta\psi^*$.

In the following, we describe various ways to apply BCs at the macroscopic level using a case study of a 1:1 electrolyte, where the ions are modeled as charged hard spheres with diameters $d_+ = d_- = 3$ Å and the dielectric constant of water is 78.46. The concentration is 1 M and the temperature is 298.2 K. We show results for the special case of $\sigma_1 = -\sigma_2 = \sigma = 0.1$ Cm^{-2} and $L_1 = -L_2 = L$, but the equations are presented for the general case. We used 200/200 ions in the MC simulations performed in the canonical (NVT) ensemble. The dimensions of the cell are $L = 50$ Å and $H = 57.2$ Å.

Boundary Conditions at the Macroscopic Level

Boundary Conditions Set in the Bath: The Convolution Integral

Let us distinguish between the charge of the ions obtained from the simulation, $q_{\rm ion}(x)$, and the surface charges, $\sum_k \sigma_k \delta(x - x_k)$, at $x_1 = L_1$ and $x_2 = L_2$ (in this work, we assume only two charged surfaces at L_1 and L_2, but there can be more as in the simulations of KIYOHARA *et al.* [40–50] for porous electrodes). The total charge is the sum of these:

$$q(x) = q_{\rm ion}(x) + \sum_k \sigma_k \delta(x - x_k). \tag{7}$$

The ionic charge profile is obtained as an ensemble average. The electrode charges are prescribed in the constant charge ensemble, while they are obtained as ensemble averages in the constant voltage ensemble.

At the macroscopic level, the issue of electrostatic self-consistency appears when we ask the question: what kind of BC should be applied when we solve Poisson's equation *(Eq.(5))*. The traditional answer to this question is that the BC is set in the bulk electrolyte, where the average electrical field and electrical potential are zero. The corresponding solution of Poisson's equation can then be obtained in the form of a convolution integral

$$\psi(x) = -\frac{1}{\epsilon_0 \epsilon} \int_x^\infty (x' - x) q_{\rm ion}(x') dx'. \tag{8}$$

This solution was probably inspired by theories that usually consider an isolated DL where the BCs are set in infinity. Because theories (unlike simulations) provide smooth charge profiles (with the property $\lim_{x\to\infty} q(x) = 0$) without any noise, this integral works well for theories. To the best of our knowledge, the majority of researchers (among others, the authors of this paper) have used this equation in the past [6–35]. In this work, we show that this equation, from a numerical point of view, is a poor choice to compute the potential in simulation studies. The reason is that the upper integration limit is not well defined and that $q(x)$ is subject to a large statistical noise.

In practice, the upper integration limit is set somewhere in the middle of the cell where a bulk electrolyte is. Here we will use exactly the middle of the cell ($x = 0$) as the upper integration limit. Because of $x - x'$ in the integrand, this integral is very sensitive to the noise in $q(x)$, because the noise is amplified as one moves further away from the electrode.

The results of a very short (200 MC cycles; 1000 attempts to move ions were made in an MC cycle) simulation are shown in *Fig.1*. The density and charge profiles are very noisy. When we compute the potential from *Eq.(8)*, the result is subject to a large error and is far from what we are supposed to get (*Fig.2*, top panel). The slope is not necessarily zero in the bath (which means that the electrical field is not zero). If the simulation was run for longer, we would get a completely different result. In general, long simulations are needed to produce a smooth charge profile and a well established potential profile. The problem is even more serious when we try to reproduce small effects, such as the value of the electrode potential at zero electrode charge (PZC) for asymmetric electrolytes. The value of the PZC potential is very small

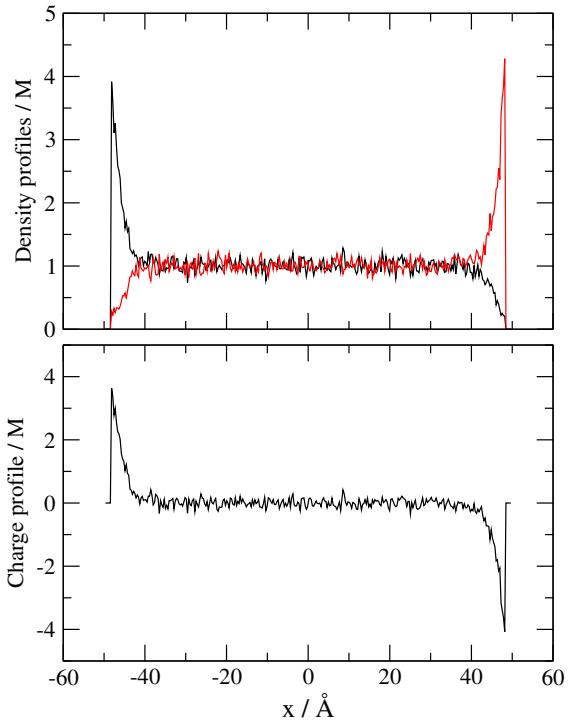

Figure 1: Density profiles (top panel) and a charge profile (bottom panel) obtained from a short (200 MC cycles) constant charge simulation using $\sigma_1 = -\sigma_2 = -0.1$ Cm^{-2}. The charge profile is obtained from $\sum_i z_i \rho_i(x)$, so its unit is M (mol dm^{-3})

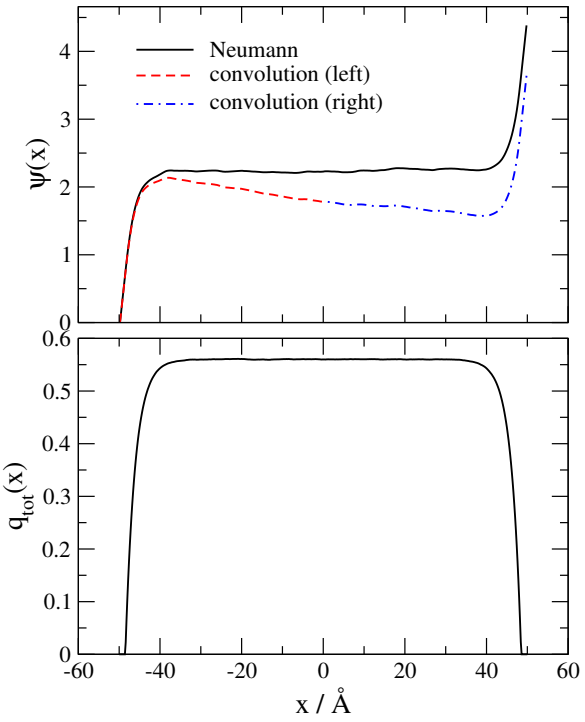

Figure 2: Potential profiles (top panel) as computed from the Neumann BC *(Eq.(11))* and the convolution integral *(Eq.(8))*. The upper limit of the convolution integral is $x = 0$ and it is computed for the left- and right-hand sides separately. The bottom panel shows the integral of the charge profile ($q_{\rm tot}(x)$, see *Eq.(7)*). It is closely related to the electric field through *Eq.(13)*. The profiles have been obtained from the curves of *Fig.1*. The electrostatic potential is shown in units of kT/e throughout this paper

and the effect of the noise is dramatic. Extremely long simulations are needed to obtain convergent results for the potential [51].

To illustrate this weak convergence, we have plotted the left electrode potential ($\psi(L_1) - \psi(0)$, top panel) and the voltage ($\psi(L_2) - \psi(L_1)$, bottom panel) as computed from *Eq.(8)* as functions of the performed MC cycles in *Fig.3* (red dashed curves). These potential values fluctuate strongly. The calculated values depend not only on the simulation time, but on the upper integration limit. If we shift that point a bit, we get a different result (data not shown).

Neumann Boundary Conditions and the Constant Charge Ensemble

Here we propose, instead, to use Neumann or Dirichlet BCs at the boundaries of the simulation cell (at L_1 and L_2, or, equivalently, at $-\infty$ and ∞). In the case of the Neumann BC, the normal electrical field is prescribed, while in the case of the Dirichlet BC, the electrical potential is prescribed at the confining walls. Our simulation setup ensures that the simulation cell is always charge neutral. Then, Gauss law states that the average electrical field is zero outside the cell for the regions $z < L_1$ and $z > L_2$. This information makes the Neumann BC applicable both in the constant charge and constant voltage ensembles.

In the constant charge ensemble, the potential difference between the electrodes is an output of the calculation. Therefore, we cannot use it as a BC, so we cannot apply the Dirichlet BC in this case. In the constant voltage ensemble, on the other hand, the potential difference is known in advance (see the next section). In the constant voltage ensemble, therefore, both Neumann and Dirichlet BCs can be used and they should give the same answer (apart from errors related to the size of the system, see later).

The Neumann BC for *Eq.(8)* is that the electrical field is zero outside the system:

$$E(x \to -\infty) = -\left.\frac{d\psi(x)}{dx}\right|_{x\to-\infty} = 0 \qquad (9)$$

and the same for $x \to \infty$. By integrating Poisson's equation once, we obtain

$$\frac{d\psi(x)}{dx} = -\frac{1}{\epsilon_0 \epsilon}\int_{-\infty}^{x} q(x')dx' + C_1 \qquad (10)$$

where C_1 is an integration constant. Taking *Eq.(10)* at

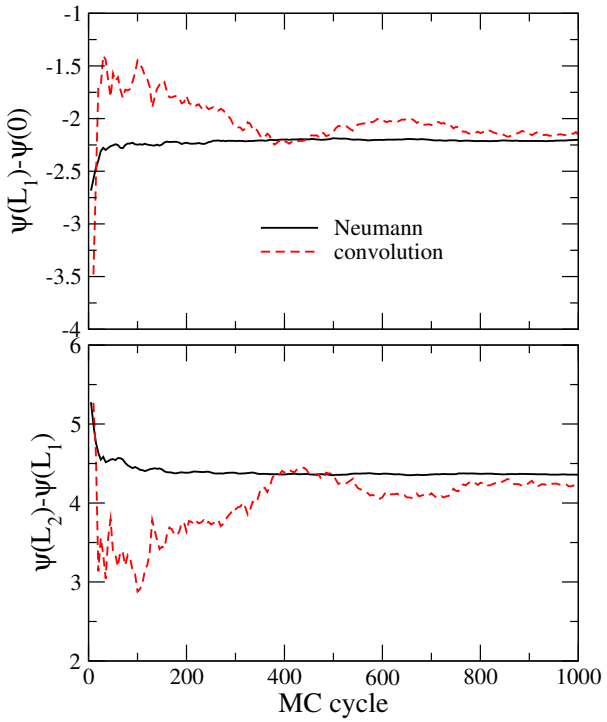

Figure 3: Convergence of the left electrode potential (top panel) and the voltage (bottom panel) as computed from the Neumann BC *(Eq.(11))* and the convolution integral *(Eq.(8))* in the constant charge ensemble.

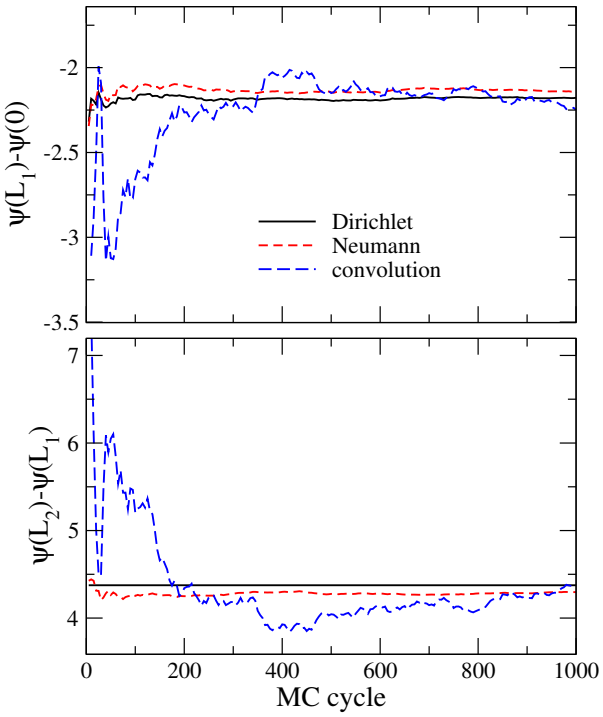

Figure 4: Convergence of the left electrode potential (top panel) and the voltage (bottom panel) as computed from the Neumann BC *(Eq.(11))*, the Dirichlet BC *(Eq.(17))*, and the convolution integral *(Eq.(8))* in the constant voltage ensemble

any location $x < L_1$ (where $q(x) = 0$) and using the BC *(Eq.(9))*, we get $C_1 = 0$ for the integration constant. If we use *Eq.(7)* for $q(x)$, we obtain

$$\frac{d\psi(x)}{dx} = -\frac{1}{\epsilon_0\epsilon}\int_{L_1}^{x} q_{\rm ion}(x')dx' - \frac{1}{\epsilon_0\epsilon}\sigma_1 \qquad (11)$$

for $L_1 < x < L_2$. The change in the lower integration limit was possible because ions exist only between the two electrodes ($q_{\rm ion} \neq 0$ only for $L_1 < x < L_2$). Introducing

$$q_{\rm tot}(x) = \int_{L_1}^{x} q_{\rm ion}(x')dx' \qquad (12)$$

for the integral of the ionic charge profile (the total charge density per area in the $[L_1, x]$ interval), the electrical field can be given as

$$E(x) = \frac{1}{\epsilon_0\epsilon}q_{\rm tot}(x) + \frac{1}{\epsilon_0\epsilon}\sigma_1 \qquad (13)$$

for $L_1 < x < L_2$. The $q_{\rm tot}(x)$ profile is shown in the bottom panel of *Fig.2*. For the special case of $\sigma_1 = -\sigma_2$, the total ionic charge is zero in the system, so $q_{\rm tot}(L_2) = 0$. The nearly constant but noisy profile in the middle of the cell represents the bulk region.

Integrating once more, we obtain

$$\psi(x) = -\frac{1}{\epsilon_0\epsilon}\int_{L_1}^{x} q_{\rm tot}(x')dx' - \frac{1}{\epsilon_0\epsilon}\sigma_1(x - L_1) + C_2, \qquad (14)$$

where C_2 is another integration constant. Its value is inconsequential because we can set the zero level of the potential arbitrarily. *Fig.2* shows the $\psi(x)$ profile where $C_2 = 0$. It is usual, however, to set the ground in the bulk, so $C_2 = -\overline{\psi(0)}$, where $\overline{\psi(0)}$ is the average of the potential profile over the bulk. KIYOHARA and ASAKA [39, 52] used an equation of a convolution form that can be shown to be equivalent to *Eq.(14)*, but they seemed to leave out the linear term containing σ_1.

Eq.(14) is different from the convolution integral *(Eq.(8))* because it does not suffer from the uncertainty in the upper integration limit and from errors originating from the noise of the $q_{\rm ion}(x)$ profile. The integration is performed for a well defined finite domain from the left electrode to x. *Fig.3* shows that this equation provides a much better convergence as a function of simulation time for the same simulation (same $q_{\rm ion}(x)$).

This procedure was used in our papers for inhomogeneous electrolyte systems to compute the mean electrostatic potential [53–56]. It was especially useful for electrolytes adsorbed in narrow slits [55, 56]. In this case, the DLs formed at the walls of the slit overlap so a bulk electrolyte does not form in the middle of the slit and the slit is not charge neutral. The Neumann BC is then the natural BC so the electric field is zero behind the walls. In another example, the Neumann BC is used to compute the potential for a DL model, where the electrode, the

inner layer, and the electrolyte have different dielectric constants [54]. In this case, the polarisation charge induced at the dielectric boundaries must also be included in *Eq.(14)*.

Dirichlet Boundary Conditions and the Constant Voltage Ensemble

An alternative method is the constant voltage ensemble of KIYOHARA and ASAKA [39]. Here, the electrode charges fluctuate and the potential between the electrodes is prescribed. Therefore, we can also apply Dirichlet BCs, where

$$\psi(L_1) = 0 \tag{15}$$

and

$$\psi(L_2) = \Delta\psi^*. \tag{16}$$

The general solution for the potential profile in the $L_1 < x < L_2$ range is

$$\psi(x) = -\frac{1}{\epsilon_0\epsilon}\int_{L_1}^{x} q_{\rm tot}(x')dx' + C_1(x-L_1) + C_2, \tag{17}$$

where we integrate from the right-hand side of the electrode at $x = L_1$, so the surface charge σ_1 is now excluded from the integration. The BC at $x = L_1$ *(Eq.(15))* provides the integration constant $C_2 = 0$, while the BC at $x = L_2$ *(Eq.(16))* provides the integration constant

$$C_1 = \frac{1}{L_2 - L_1}\left[\Delta\psi^* + \frac{1}{\epsilon_0\epsilon}\int_{L_1}^{L_2} q_{\rm tot}(x)dx\right]. \tag{18}$$

Of course, we can calculate the potential profile using the Neumann BCs too. In that case, we must use $\langle\sigma_1\rangle$ in *Eq.(14)* instead of σ_1 because the electrode charge is now fluctuating so its value is not known in advance. Therefore, its ensemble average should be used in *Eqs.(7-14)*.

In the constant voltage ensemble we need the value of the voltage that corresponds to $\sigma_1 = -0.1$ Cm^{-2} as used in the previous constant charge simulation. This value we estimated with a very long (50,000 MC cycles) constant charge simulation and was obtained as $\Delta\psi^* = 4.398\,kT/e$. This value was used in the constant voltage simulation as an input parameter.

Fig.4 is the analogous version of *Fig.3*. The black solid curves are the results obtained from the Dirichlet BCs *(Eqs.(17)* and *(18))*. The red short-dashed curves show the results of the Neumann BC using $\langle\sigma_1\rangle$ in *Eq.(14)*. The convolution integral results (blue long-dashed curves) are inaccurate and poorly converged for such a short simulation.

In the constant voltage ensemble the electrode charge is a fluctuating quantity. *Fig.5* shows its convergence. Its limiting value is not equal to that used in the constant charge simulation that provided the input voltage value $\Delta\psi^* = 4.398\,kT/e$. The deviation is due to finite size of the system. Using a larger simulation box (larger H), a smaller deviation is observed (data not shown). This deviation is also observed in *Fig.4*. The limiting value of the

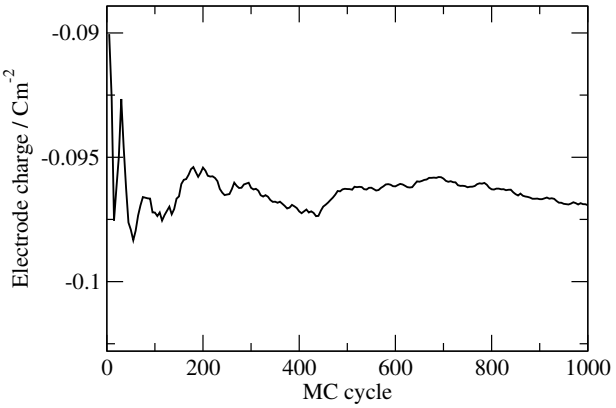

Figure 5: Convergence of the electrode charge in the constant voltage ensemble

potential difference $\Delta\psi = \psi(L_2) - \psi(L_1)$ obtained from the calculation using the Neumann BC (bottom panel) is different from the prescribed value (the value used in the Dirichlet BC, see also bottom panel).

This behaviour is analogous to that discussed earlier regarding the example of the pressure computed in the NVT and NpT ensembles. The constant charge ensemble corresponds to the NVT, while the constant voltage ensemble corresponds to the NpT ensemble. In the constant charge ensemble, the voltage is computed using the Neumann BC, just as the pressure is computed in the NVT ensemble from the virial sum. In the constant voltage ensemble, the voltage is prescribed, just as the pressure is prescribed in the NpT ensemble. The voltage can also be computed from the Neumann BC, just as the pressure can also be computed from the virial sum in the NpT ensemble.

Conclusion

We propose that the Neumann or Dirichlet BCs should be used in computing the mean electrostatic potential for the planar DL geometry studied by computer simulations. The commonly used convolution integral of *Eq.(8)* requires a vaguely defined upper integration limit and also suffers from numerical problems because it magnifies the effect of the noise in the charge profile that is always present in computer simulations. The problem of noise in the density profiles is unique to simulations and therefore more care must be taken in computing the electrostatic potential. On the other hand, theories [6–16], which produce smooth, noise-free density profiles, can use the convolution integral.

We have shown here that the numerical method we proposed is much more efficient than the convolution integral, because we use unambiguous parameters in the BC, specifically, the electrode charge in the case of the Neumann BC and the voltage in the case of the Dirichlet BC. Also, the simulation cell is necessarily finite, therefore, the boundaries of the system are always well de-

fined. Overall, our method leads to converged results with very short simulations.

Acknowledgement

The present publication was realised with the support of the projects TÁMOP-4.2.2/A-11/1/KONV-2012-0071 and TÁMOP-4.1.1/C-12/1/KONV-2012-0017.

REFERENCES

[1] GOUY G.: Sur la constitution de la charge electrique a la surface d'un electrolyte (English Title Please), J. Phys. (Paris), *1910*, 9, 457 (in French)

[2] CHAPMAN D.L.: A Contribution to the Theory of Electrocapillarity, Phil. Mag., *1913*, 25, 475

[3] DEBYE P., HÜCKEL E.: The theory of electrolytes. I. Lowering of freezing point and related phenomena, Physik. Z., *1923*, 24, 185–206

[4] DERJAGUIN B., LANDAU L.: Theory of the stability of strongly charged lyophobic sols and of the adhesion of strongly charged particles in the solution of electrolytes, Acta Physiochem USSR, *1941*, 14, 633–662

[5] VERWEY E.J.W., OVERBEEK J.T.G.: Theory of the Stability of Lyophobic Colloids Elsevier, Amsterdam, *1948*

[6] BLUM L.: Theory of electrified interfaces, J. Phys. Chem., *1977*, 81(2), 136–147

[7] HENDERSON D., BLUM L., SMITH W.R.: Application of the hypernetted chain approximation to the electric double-layer at a charged planar interface, Chem. Phys. Lett., *1979*, 63(2), 381–383

[8] BLUM L., HENDERSON D.: Mixtures of hard ions and dipoles against a charged wall: The Ornstein–Zernike equation, some exact results, and the mean spherical approximation, J. Chem. Phys., *1981*, 74(3), 1902–1910

[9] OUTHWAITE C.W., BHUIYAN L.B.: An improved modified Poisson-Boltzmann equation in electric-double-layer theory, J. Chem. Soc. Faraday. Trans. II., *1983*, 79, 707–718

[10] LOZADA-CASSOU M., HENDERSON D.: Application of the hypernetted chain approximation to the electrical double-layer - comparison with Monte Carlo results for 2-1 and 1-2 salts, J. Phys. Chem., *1983*, 87(15), 2821–2824

[11] MIER-Y TERAN L., SUH S.H., WHITE H.S., DAVIS H.T.: A nonlocal free-energy density-functional approximation for the electrical double-layer, J. Chem. Phys., *1990*, 92(8), 5087–5098

[12] KIERLIK E., ROSINBERG M.L.: Free-energy density functional for the inhomogeneous hard-sphere fluid - application to interfacial adsorption, Phys. Rev. A, *1990*, 42(6), 3382–3387

[13] ROSENFELD Y.: Free-energy model for inhomogeneous fluid mixtures - Yukawa-charged hard-spheres, general interactions, and plasmas, J. Chem. Phys., *1993*, 98(10), 8126–8148

[14] GILLESPIE D., NONNER W., EISENBERG R.S.: Density functional theory of charged, hard-sphere fluids, Phys. Rev. E, *2003*, 68(3), 031503

[15] DI CAPRIO D., STAFIEJ J., BADIALI J.P.: Field theoretical approach to inhomogeneous ionic systems: thermodynamic consistency with the contact theorem, Gibbs adsorption and surface tension, Mol. Phys., *2003*, 101(16), 2545–2558

[16] PIZIO O., PATRYKIEJEW A., SOKOLOWSKI S.: Phase behavior of ionic fluids in slitlike pores: A density functional approach for the restricted primitive model, J. Chem. Phys., *2004*, 121(23), 11957–11964

[17] TORRIE G.M., VALLEAU J.P.: Monte Carlo study of an electrical double-layer, Chem. Phys. Lett., *1979*, 65(2), 343–346

[18] TORRIE G.M., VALLEAU J.P.: Electrical double-layers 1. Monte Carlo study of a uniformly charged surface, J. Chem. Phys., *1980*, 73(11), 5807–5816

[19] TORRIE G.M., VALLEAU J.P., PATEY, G.N.: Electrical double-layers 2. Monte Carlo and HNC studies of image effects, J. Chem. Phys., *1982*, 76(9), 4615–4622

[20] VALLEAU J.P., TORRIE G.M.: The electrical double-layer 3. Modified Gouy-Chapman theory with unequal ion sizes, J. Chem. Phys., *1982*, 76(9), 4623–4630

[21] TORRIE G.M., VALLEAU J.P.: Electrical double-layers 4. Limitations of the Gouy-Chapman theory, J. Phys. Chem., *1982*, 86(16), 3251–3257

[22] VALLEAU J.P., TORRIE G.M.: Electrical double-layers 5. Asymmetric ion wall interactions, J. Chem. Phys., *1984*, 81(12), 6291–6295

[23] TORRIE G.M., VALLEAU J.P., OUTHWAITE C.W.: Electrical double-layers 6. Image effects for divalent ions, J. Chem. Phys., *1984*, 81(12), 6296–6300

[24] VAN MEGEN W., SNOOK I.: The grand canonical ensemble Monte Carlo method applied to the electrical double-layer, J. Chem. Phys., *1980*, 73(9), 4656–4662

[25] SNOOK I., VAN MEGEN W.: Finite ion size effects in the electrical double-layer - a Monte Carlo study, J. Chem. Phys., *1981*, 75(8), 4104–4106

[26] BRATKO D., JÖNSSON B., WENNERSTRÖM H.: Electrical double layer interactions with image charges, Chem. Phys. Lett., *1986*, 128, 449–454

[27] TANG Z.X., SCRIVEN L.E., DAVIS H.T.: A 3-component model of the electrical double-layer, J. Chem. Phys., *1992*, 97(1), 494–503

[28] PHILPOTT M.R., GLOSLI J.N.: Molecular dynamics simulation of interfacial electrochemical processes: Electric double layer screening, Solid-liquid Electrochemical Interfaces, *1997*, 656, 13–30

[29] BODA D., CHAN K.Y., HENDERSON D.: Monte Carlo simulation of an ion-dipole mixture as a model of an electrical double layer, J. Chem. Phys., *1998*, 109(17), 7362–7371

[30] SPOHR E.: Computer simulation of the structure of the electrochemical double layer, J. Electroanalytical Chem., *1998*, 450(2), 327–334

[31] BODA D., HENDERSON D., CHAN K.Y.: Monte Carlo study of the capacitance of the double layer in a model molten salt, J. Chem. Phys., *1999*, 110(11), 5346–5350

[32] CROZIER P.S., ROWLEY R.L., HENDERSON D.: Molecular-dynamics simulations of ion size effects on the fluid structure of aqueous electrolyte systems between charged model electrodes, J. Chem. Phys., *2001*, 114(17), 7513–7517

[33] GUYMON C.G., HUNSAKER M.L., HARB J.N., HENDERSON D., ROWLEY R.L.: Effects of solvent model flexibility on aqueous electrolyte behavior between electrodes, J. Chem. Phys., *2003*, 118(22), 10195–10202

[34] SPOHR E.: Some recent trends in computer simulations of aqueous double layers, Electrochimica Acta, *2003*, 49(1), 23–27

[35] HENDERSON D., BODA D.: Insights from theory and simulation on the electrical double layer, Phys. Chem. Chem. Phys., *2009*, 11(20), 3822–3830

[36] ALLEN M.P., TILDESLEY D.J.: Computer Simulation of Liquids Oxford, New York, *1987*

[37] FRENKEL D., SMIT B.: Understanding molecular simulations Academic Press, San Diego, *1996*

[38] JACKSON J.D.: Classical Electrodynamics Wiley, New York, 3rd edn., *1999*

[39] KIYOHARA K., ASAKA K.: Monte Carlo simulation of electrolytes in the constant voltage ensemble, J. Chem. Phys., *2007*, 126(21), 214704 (pages 14)

[40] KIYOHARA K., ASAKA K.: Monte Carlo simulation of electrolytes in the constant voltage ensemble, J. Chem. Phys., *2007*, 126(21), 214704

[41] KIYOHARA, K., ASAKA, K.: Monte Carlo simulation of porous electrodes in the constant voltage ensemble, J. Phys. Chem. C, *2007*, 111(43), 5903–15909

[42] KIYOHARA K., SUGINO T., TAKEUCHI I., MUKAI K., ASAKA K.: Expansion and contraction of polymer electrodes under an applied voltage, J. Appl. Phys., *2009*, 105(6), 063506

[43] KIYOHARA K., SUGINO T., TAKEUCHI I., MUKAI K., ASAKA K.: Expansion and contraction of polymer electrodes under an applied voltage, J. Appl. Phys., *2009*, 105(11), 119902

[44] KIYOHARA K., SUGINO T., ASAKA K.: Electrolytes in porous electrodes: Effects of the pore size and the dielectric constant of the medium, J. Chem. Phys., *2010*, 132(14), 144705

[45] KIYOHARA K., SUGINO T., ASAKA K.: Phase transition in porous electrodes, J. Chem. Phys., *2011*, 134(15), 154710

[46] KIYOHARA K., SUGINO T., ASAKA K.: Molecular mechanism of ionic electroactive polymer actuators, Smart Mat. & Struc., *2011*, 20(12), 124009

[47] KIYOHARA K., SHIOYAMA H., SUGINO T., ASAKA K.: Phase transition in porous electrodes. II. Effect of asymmetry on ion size, J. Chem. Phys., *2012*, 136(9), 094701

[48] KIYOHARA K., ASAKA K.: Voltage induced pressure in porous electrodes, Mol. Phys., *2013*, 111(2), 295–306

[49] KIYOHARA K., SHIOYAMA H., SUGINO T., ASAKA K., SONEDA Y., IMOTO K., KODAMA M.: Phase transition in porous electrodes. III. In the case of a two component electrolyte, J. Chem. Phys., *2013*, 138(23), 234704

[50] KIYOHARA K., SHIOYAMA H., SUGINO T., ASAKA K., SONEDA Y., IMOTO K., KODAMA M.: Phase transition in porous electrodes. III. In the case of a two component electrolyte (vol 138, 234704, 2013), J. Chem. Phys., *2013*, 139(6), 069902

[51] VALISKÓ M., HENDERSON D., BODA D.: Competition between the effects of asymmetries in ion diameters and charges in an electrical double layer studied by Monte Carlo simulations and theories, J. Phys. Chem. B, *2004*, 108(42), 16548–16555

[52] KIYOHARA K., ASAKA K.: Monte Carlo Simulation of Porous Electrodes in the Constant Voltage Ensemble, J. Phys. Chem. C, *2007*, 111(43), 15903–15909

[53] NAGY T., VALISKÓ M., HENDERSON D., BODA D.: The Behavior of 2:1 and 3:1 Electrolytes at Polarizable Interfaces, J. Chem. Eng. Data, *2011*, 56(4), 1316–1322

[54] NAGY T., HENDERSON D., BODA D.: Simulation of an electrical double layer model with a low dielectric layer between the electrode and the electrolyte, J. Phys. Chem. B, *2011*, 115(39), 11409–11419

[55] KOVÁCS R., VALISKÓ M., BODA D.: Monte Carlo simulation of the electrical properties of electrolytes adsorbed in charged slit-systems, Cond. Matt. Phys., *2012*, 15(2), 23803

[56] VALISKÓ M., HENDERSON D., BODA D.: Selective adsorption of ions in charged slit systems, Cond. Matt. Phys., *2013*, 16(4), 43601

HUNGARIAN JOURNAL
OF INDUSTRY AND CHEMISTRY
VESZPRÉM
Vol. 41(2) pp. 131–136 (2013)

DEGRADATION OF REINFORCED AND UNREINFORCED WASTE POLYAMIDES DURING MECHANICAL RECYCLING

JÁNOS SÓJA AND NORBERT MISKOLCZI✉

MOL Department of Hydrocarbon and Coal Processing, Institute of Chemical Engineering and Process Engineering, University of Pannonia, Egyetem u. 10, 8200, HUNGARY
✉Email: mnorbert@almos.uni-pannon.hu

The paper discusses the degradation of waste polyamides during mechanical recycling from the automotive sector. Two different polyamides were investigated: glass fibre reinforced and unreinforced. Raw materials were reprocessed twenty times and the changes in their properties were investigated as a function of reprocessing number. Considerable differences were found in relation to the specimen properties between reinforced and unreinforced waste materials. For example, the tensile strengths of reinforced and unreinforced polyamide 6.6 wastes were 84.2 and 165.2 MPa, respectively, which dropped to 38.0 and 97.0 MPa after the twentieth reprocessing cycle. Specimens from the reprocessing procedure have been investigated by Fourier transformed infrared spectroscopy in the spectral range of 400–4000 cm^{-1}. Due to mechanical stress between the rotating screw and plasticising cylinder, the reinforcements broke. The average length of the glass fibre was decreased as a function of the reusing cycle number from 1890 to 580 μm.

Keywords: polyamide, mechanical recycling, degradation, FTIR

Introduction

As a result of the continuously increasing trend in the demand for polymer worldwide, ever increasing amounts of waste polymers are generated. Polyamides (PA) are expensive engineering plastics, especially if they are reinforced. In particular, glass fibre composites are widespread among fibre-reinforced materials, as a results of their favourable mechanical and economical properties. The application of glass fibre results in improved tensile and flexural properties. Thermoplastic polyamides contain typically 10-30% glass fibres as reinforcements and are applied in many industries such as the automotive sector, civil engineering, packaging, and biomedical applications [1-9,11,16].

A grand challenge is the utilisation of plastic wastes. Polymer materials have a high resistance to different environmental and mechanical effects, which yields their favourable characteristics. Such advantageous properties can easily become disadvantage owing to waste polymers inability to decompose within a reasonable time frame. Unfortunately, a vast amount of polymer waste ends up to landfills, where non-degradable plastics together with other materials accumulate and pollute the environment [10,12-15]. The most studied recycling technologies are mechanical or chemical. Chemical recycling is a thermal process for cracking the long carbon chains of polymers into gases and liquid hydrocarbons in the absence of oxygen within in temperature range of 400-1000 °C. The other technology is mechanical recycling, when waste polymers are mixed with original granulates and newly shaped by injection moulding or extrusion. Mechanical recycling is a good option for reusing waste plastic, only when selectively collected polymers of high purity are available. Similarly to the chemical process, the polymer chains can degrade due to mechanical and thermal stresses during the pre-treating and shaping steps. Therefore, it is important to know the behaviour of polymer chains when exposed to thermal and mechanical stresses [9,11-16].

The goal of our work was to investigate the mechanical recycling of reinforced and unreinforced waste polyamides. Waste polymers have been reprocessed twenty times and the changes of mechanical amongst other properties were investigated. The effects of reinforcements on the loss of properties during the reshaping procedures were followed.

Experimental

Plastics

Glass fibre reinforced and unreinforced waste polyamides were used as raw materials. The main properties of the raw materials are shown in *Table 1*.

Table 1: The main properties of raw materials

	Reinforced	Unreinforced
MFI,* g $(10\ min)^{-1}$	15.1	11.8
Ash content, %	30.6	0.03
Tensile strength, MPa	165.2	84.2
Charpy strength, kJ m^{-2}	13.4	12.1

* 275 ºC, 5 kg

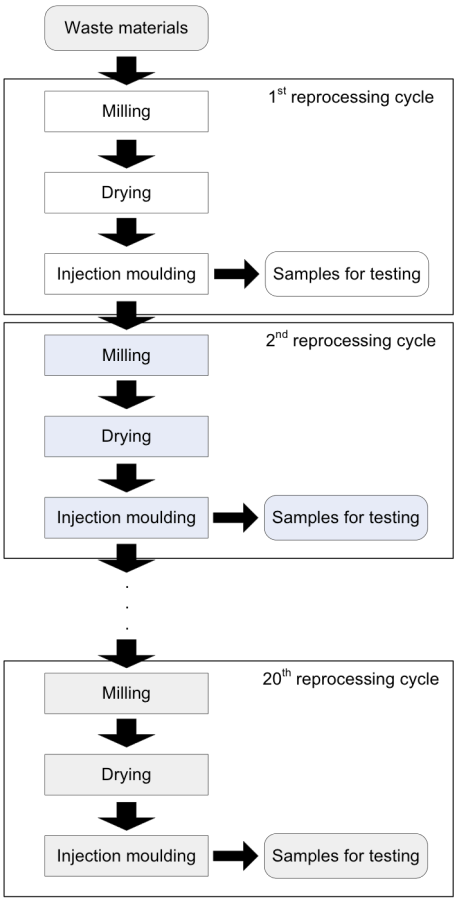

Figure 1: The main experimental steps

Sample Preparation

Due to PA samples being sensitive to humidity, raw materials before processing and samples before testing were dried. Drying was carried out in an air circulated drying box at 90 ºC for 2 h. The injection moulding of the specimens was carried out by a microprocessor-controlled injection moulding machine. The dimensions of dog-boned injection moulded specimens were 3 mm × 10 mm in cross-section and 50 mm in length. *Fig.1* illustrates the main experimental steps.

Methods

The tensile and three point flexural properties (mainly stress and extension) (MSZ EN ISO 527-1-4:1999, MSZ EN ISO 14125:1999) were determined using an INSTRON 3345 universal tensile testing machine. The temperature and relative humidity in the laboratory were 23 ºC and 60% respectively, during the mechanical tests. Tensile tests were carried out at a crosshead speed of 80 mm min^{-1}. During the investigation of flexural properties, the crosshead testing speed was 20 mm min^{-1}. Samples were also investigated by infrared spectroscopy with a TENSOR 27 type FTIR spectrometer (resolution: 3 cm^{-1}, illumination: SiC Globar light, detector: RT-DLaTGS type) within the 400-4000 cm^{-1} wave number range. A CEAST Resil

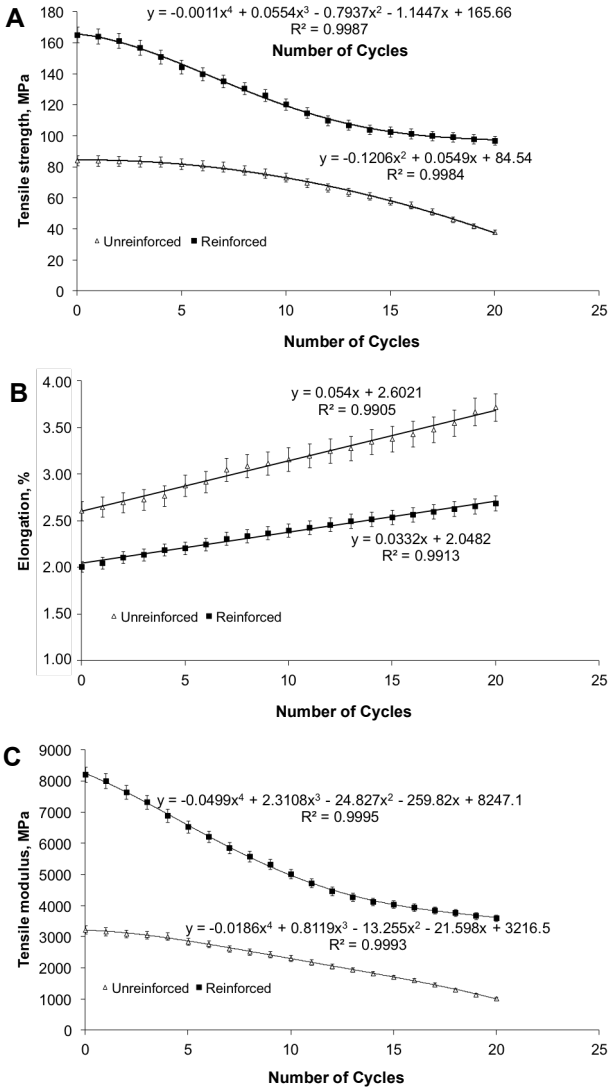

Figure 2: Tensile properties of reinforced and unreinforced polyamide 6.6 wastes: A) tensile strength, B) elongation and C) tensile modulus

Impactor was applied to measure the Charpy impact strength of the produced samples according to the MSZ EN ISO 179-2:2000 standard.

Results and Analysis

Tensile Properties

The tensile properties of reshaped specimens are summarised in *Figs.2A-2C*. The tensile strength of reinforced and unreinforced polyamide 6.6 wastes were 84.2 MPa and 165.2 MPa, respectively, which were reduced to 38.0 MPa and 97.0 MPa after the twentieth reprocessing cycle (*Fig.2A*). It is important to note that the decreasing trends were considerably different in the two cases: a fourth order trend line in the case of reinforced samples and a second order one in the case of unreinforced samples were found as shown in *Fig.2A*. A short section with a barely decreasing slope can be found both at the beginning (before the third cycle) and at the end (after the fifteenth cycle) of the trend line for

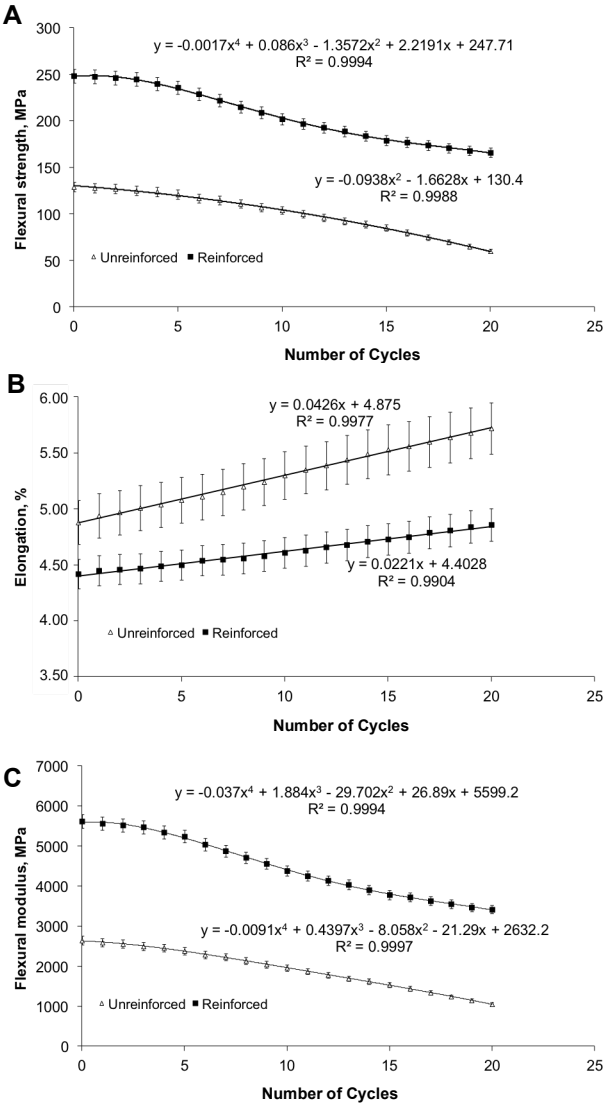

Figure 3: Flexural properties of reprocessed reinforced and unreinforced polyamide 6.6 wastes A) flexural strength, B) elongation and C) flexural modulus

the reinforced specimens. In the case of unreinforced specimens a similar phenomenon was found only up to the ninth cycle.

The elongations of specimens are shown in *Fig.2B*. Owing to the rigid property of polyamides the relative elongations are rather small (below 3.8%). As results demonstrate the change in elongations was rather linear, but the gradient was different when the reinforced (tan α = 0.033) and unreinforced (tan α = 0.054) raw materials were investigated; because a slower ratio in change was found in the presence of glass fibres in polyamide wastes.

As demonstrated by the tensile strength, tensile moduli show a decreasing trend as well. Furthermore, the trend line is highly similar to the measured data for tensile strength. The E-modulus of reinforced and unreinforced wastes was 8219 MPa and 3226 MPa, respectively. Those were decreased to 3606 MPa and 1022 MPa according to the mathematical equations in *Fig.2C*.

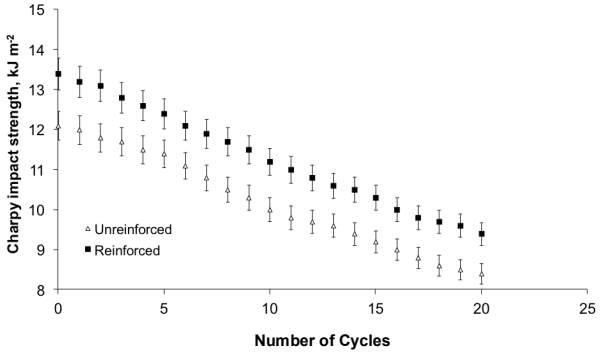

Figure 4: Charpy impact strength of reprocessed reinforced and unreinforced polyamide 6.6 wastes

Flexural Properties

The flexural properties of reshaped specimens are summarised in *Figs.3A-3C*. The change in both flexural strength and E-modulus followed a decreasing trend, while the trend in terms of elongation was rather increasing. The results were similar to the tensile properties discussed above. It is important to note that the shapes of trend lines were also similar to results demonstrated before. When reinforced polyamide 6.6 waste material was reprocessed the flexural strength, elongation and E-modulus changed from 248.5 MPa, 4.42% and 5622 MPa to 166.0 MPa, 4.86% and 3416 MPa, respectively. By taking into consideration the results of both tensile and flexural tests it can be concluded that the glass fibre reinforcement helps to keep the high values of strengths and E-moduli in the case of reinforced polymers at the start of property curves as a function of processing cycle number. Approximately after the third-to-fifth reprocessing cycles, the dropping ratio was increased step by step. Presumably this was the consequence of the glass fibres degrading into pieces. On the contrarily, a relatively constant dropping ratio was found in the unreinforced case.

Charpy Impact Strength

The Charpy impact strength test is one of the most widely specified mechanical tests of polymeric materials to provide information about impact properties. Results of Charpy tests were summarised in *Fig.4*. The change in Charpy impact strength followed a decreasing trend in both cases. Moreover, a similar trend in the changes could be found, because the gradients were 13.38 and 12.18 for reinforced samples and unreinforced specimens, respectively. The Charpy impact strengths were 12.1 kJ m^{-2} and 13.4 kJ m^{-2} without any reprocessing, and decreased to 8.4 kJ m^{-2} and 9.4 kJ m^{-2} respectively by the end of the procedure. Naturally the reinforced samples gave higher values of impact strength.

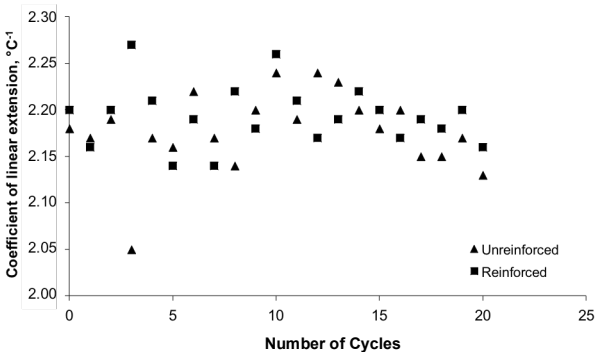

Figure 5: Coefficient of linear heat extension of reprocessed reinforced and unreinforced polyamide 6.6 wastes

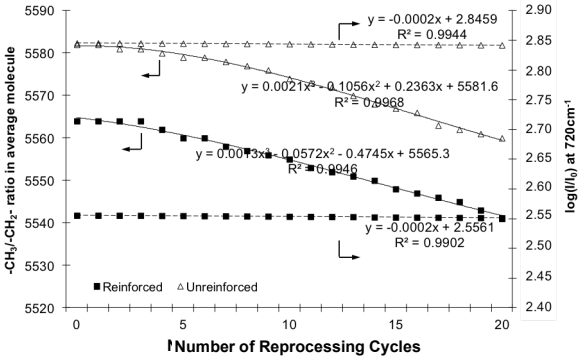

Figure 7: The change in the $–CH_3/–CH_2–$ ratio of an average molecule and the value of $\log(I/I_0)$ from FTIR spectra at 720 cm^{-1} as a function of the reprocessing cycles in the cases of reinforced and unreinforced polyamides

Linear Extension Coefficient

The coefficient of thermal expansion describes the change in dimensions of samples against changing temperature at a constant pressure. Regarding polymers the linear extension coefficient is used to classify the materials. As it is known, thermal expansion decreases with increasing bond energy and the thermal extension of the amorphous phase is higher than that of the crystalline phase, because rearrangements in the structure can be achieved at the glass transition temperature. A change in ratio of amorphous and crystalline phases occurs. The coefficients of linear extension are demonstrated in *Fig.5*. Results demonstrate well that the coefficient changes randomly in both cases between 2.05 and 2.27 with approximately the same average value of 2.18 $ºC^{-1}$ for the reinforced and unreinforced specimens within 0.01 $ºC^{-1}$. Presumably no rearrangements in the structures of the tested materials occurred during the reprocessing and the ratio of the amorphous to crystalline phases remained similar. In other words, the specimens a have relatively permanent stability of shape.

Fourier Transformed Infrared Spectroscopy

Samples from the reprocessing procedure were also investigated by Fourier transformed infrared spectroscopy

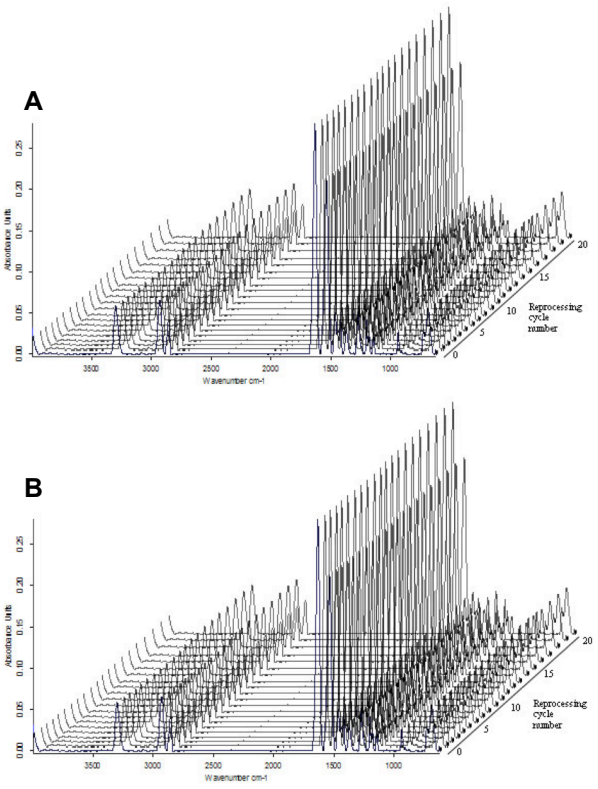

Figure 6: FTIR spectra of reinforced (A), and unreinforced polyamide (B)

(FTIR), which provides a measure of changes in molecular structures through molecular vibrational excitations. The FTIR spectra of reinforced and unreinforced waste polymers as a function of the reprocessing cycles are shown in *Figs.6A* and *6B*. By this method, modifications in the molecular structures of polymers could be observed as a result of changes in their chemical bonds. A typical spectrum of polyamide can be described as follows:

- stretching vibration of $-CH_2-$ and $-CH_3$ groups between 2800–3000 cm^{-1}
- symmetric and asymmetric deformation stretching of $-CH_3$ groups between 1430 and 1470 cm^{-1} and 1365 and 1395 cm^{-1}
- $\beta_{asymmetric}CH_2$ of $-CH_2-$ groups at 720 cm^{-1}
- bands at 3350, 1730 cm^{-1}, and 630 cm^{-1} as well referring to the N–H and C=O bonds from –NH– and –CO functional groups.

The methyl/methylene group ($–CH_3/–CH_2–$) ratio in an average molecule was calculated based on the FTIR peak intensities in the range of 2800–3000 cm^{-1}. Results are summarised in *Fig.7*. As shown, the ratio of methyl and methylene groups slowly decreased in both cases as a function of reprocessing cycles. This suggests that the numbers of methyl groups increased, while the methylene groups decreased in an average molecule. This is a consequence of polymer degradation, when the C-C bonds of main polymer chains are cleaved, which resulted in shorter chains containing less methylene groups.

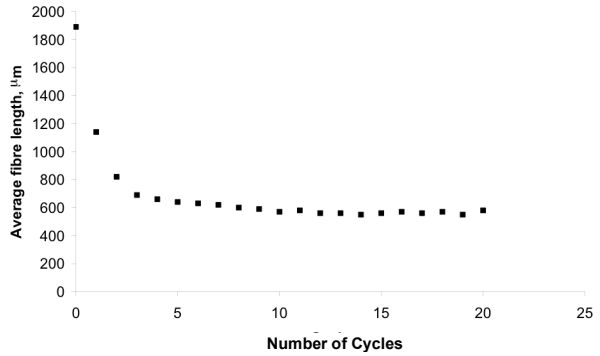

Figure 8: The average length of glass fibre reinforcements as a function of reprocessing cycles

Scanning Electron Microscope Graphs

As the polyamide matrix covered the fibres, it was difficult to determine their average length. Therefore to investigate the average length of the reinforcements and thus gain insights into their degree of degradation, the samples were burned and the remaining glass fibres were investigated by SEM techniques. The results are shown in *Fig.8*. As shown, the average length of the glass fibre reinforcements decreased as a function of the reusing cycle number. The length of glass fibres suddenly decreased from 1890 μm to 660 μm during the first four cycles of reprocessing. Then the average length exhibited a relatively constant value between 550 and 640 μm. The mean and standard deviation were 581 μm and 28 μm between the fifth and twentieth cycles, respectively. The cause for the degradation of the reinforcement fibres was the mechanical stress caused by the rotating screw and plasticising cylinder.

Conclusions

We investigated the reprocessing of waste glass fibre reinforced and unreinforced polyamide 6.6 materials. It was found that the mechanical properties of both wastes deteriorated as a function of reprocessing. For example, the tensile strengths of reinforced and unreinforced polyamide 6.6 wastes were 84.2 MPa and 165.2 MPa, respectively, which decreased to 38.0 MPa and 97.0 MPa after the twentieth reprocessing cycle. On the other hand, the trend lines of the changes were significantly different in the case of reinforced and unreinforced wastes. More gradually decreasing ratios could be measured regarding unreinforced plastics until the tenth cycle. Based on infrared spectra, it was concluded that the deterioration in mechanical properties presumably was the consequence of polymer degradation. The C-C bonds of the main polymer chains were broken and resulted in the formation of shorter polymer chains. The lengths of glass fibres suddenly decreased from 660 μm to 1890 μm during the first four cycles of reprocessing. Then, the average length exhibited a relatively constant value between 550 and 640 μm. The coefficients of linear heat extension changed randomly in both cases between 2.05 and 2.27 $^{o}C^{-1}$. The average value was 2.18 $^{o}C^{-1}$ for both reinforced and unreinforced samples within 0.01 $^{o}C^{-1}$.

REFERENCES

[1] TROEV K., TODOROVA N., MITOVA V., VASSILEVA ST., GITSOV I.: Phosphorus-containing oligoamides obtained by a novel one-pot degradation of polyamide-6, Polymer Degrad. Stabil., *2006*, 91(4), 778-788

[2] PEDROSO A.G., MEI L.H.I., AGNELLI J.A.M., ROSA D.S.: The influence of the drying process time on the final properties of recycled glass fiber reinforced polyamide 6, Polymer Testing, *2002*, 21(2), 229-232

[3] GRÖNING M., ERIKSSON H., HAKKARAINEN M., ALBERTSSON A.C.: Phenolic prepreg waste as a functional filler with an antioxidant effect in polypropylene and polyamide-6, Polymer Degrad. Stabil., *2006*, 91(8), 1815-1823

[4] GOITISOLO I., EGUIAZÁBAL J.I., NAZÁBAL J.: Effects of reprocessing on the structure and properties of polyamide 6 nano-composites, Polymer Degrad. Stabil., *2008*, 93(10), 1747-1752

[5] BERNASCONI A., DAVOLI P., ARMANN C.: Fatigue strength of a clutch pedal made of reprocessed short glass fibre reinforced polyamide, Int. J. Fatigue, *2010*, 32(1), 100-107

[6] LA MANTIA F.P., SCAFFARO R.: Melt stabilization of wet polyamide 6, Polymer Degrad. Stabil., *2002*, 75(3), 473-477

[7] BERNASCONI A., DAVOLI P., ROSSIN D., ARMANNI C.: Effect of reprocessing on the fatigue strength of a fibreglass reinforced polyamide, Composites Part A: Appl. Sci. Manufact., *2007*, 38(3), 710-718

[8] HASSAN M.M., BADWAY N.A., GAMAL A.M., ELNAGGAR M.Y., HEGAZY E.S.A.: Studies on mechanical, thermal and morphological properties of irradiated recycled polyamide and waste rubber powder blends, Nuclear Instruments and Methods in Physics Research Section B: Beam Interactions with Materials and Atoms, *2010*, 268(9), 1427-1434

[9] YU S., LIU M., MA M., QI M., LÜ Z., GAO C.: Impacts of membrane properties on reactive dye removal from dye/salt mixtures by asymmetric cellulose acetate and composite polyamide nanofiltration membranes, J. Membrane Sci., *2010*, 350(1-2), 83-91

[10] GHIDOSSI R., POUPOT C., THIBON C., PONS A., DARRIET P., RIQUIER L., DE REVEL G., PEUCHOT M.M.: The influence of packaging on wine conservation, Food Control, *2012*, 23(2), 302-311

[11] HASSAN M.M., BADWAY N.A., GAMAL A.M., ELNAGGAR M.Y., HEGAZY E.S.A.: Effect of carbon black on the properties of irradiated recycled polyamide/rubber waste composites, Nuclear Instruments and Methods in Physics Research Section B: Beam Interactions with Materials and Atoms, *2010*, 268 (16), 2527-2534

[12] HASSAN M.M., BADWAY N.A., GAMAL A.M., ELNAGGAR M.Y., HEGAZY E.S.A.: Studies on mechanical, thermal and morphological properties of irradiated recycled polyamide and waste rubber powder blends, Nuclear Instruments and Methods in Physics Research Section B: Beam Interactions with Materials and Atoms, *2010*, 268(9), 1427-1434

[13] HUANG S.H., HUNG W.S., LIAW D.J., LO C.H., CHAO W.C., HU C.C., LI C.L., LEE K.R., LAI J.Y.: Interfacially polymerized thin-film composite polyamide membranes: Effects of annealing processes on pervaporative dehydration of aqueous alcohol solutions, Separ. Purific. Techn., *2010*, 72(1), 40-47

[14] YU S., LIU M., MA M., QI M., LÜ Z., GAO C.: Impacts of membrane properties on reactive dye removal from dye/salt mixtures by asymmetric cellulose acetate and composite polyamide nanofiltration membranes, J. Membr. Sci., *2010*, 350(1-2), 83-91

[15] KILIARIS P., PAPASPYRIDES C.D., PFAENDNER R.: Influence of accelerated aging on clay-reinforced polyamide 6, Original Research Article Polymer Degradation and Stability, *2009*, 94(3), 389-396

[16] SHEN Z., BATEMAN S., WU D.Y., MCMAHON P., DELL'OLIO M., GOTAMA J.: The effects of carbon nanotubes on mechanical and thermal properties of woven glass fibre reinforced polyamide-6 nanocomposites, Composites Sci. Techn., *2009*, 69(2), 239-244